

Spectrally resolved two-photon microscopy for three-dimensional imaging and evaluation of semiconductor materials

メタデータ	言語: en
	出版者: Shizuoka University
	公開日: 2017-12-14
	キーワード (Ja):
	キーワード (En):
	作成者: Al-Tabich, Amin
	メールアドレス:
	所属:
URL	https://doi.org/10.14945/00024353

THESIS

Spectrally resolved two-photon microscopy for three-dimensional imaging and evaluation of semiconductor materials

スペクトル分解二光子顕微鏡を用いた半導体材料の三次
元観察と評価に関する研究

AMIN AL-TABICH

Graduate School of Science and Technology

Department of Nanovision Technology

Shizuoka University

2017

1. INTRODUCTION.....	6
1.1. Semiconductors.....	6
1.2. Motivation.....	7
1.3. Objective.....	8
1.4. Dissertation structure.....	9
2. TWO-PHOTON FLUORESCENCE MICROSCOPY.....	11
2.1. Historical background.....	11
2.2. Modern advances.....	12
2.3. Theoretical basis.....	15
2.4. Image formation and resolving abilities.....	24
2.5. Advantages of the two-photon method.....	31
3. SPECTRAL RESOLVING.....	37
3.1. Kasha's rule.....	37
3.2. Certainty assessment.....	39
4. SEMICONDUCTORS AND DEFECTS.....	43
4.1. Semiconductors under study.....	43
4.2. Defects and dopants.....	45
4.1. Native point defects in ZnO.....	51
5. SETUP AND SOFTWARE.....	56
5.1. Setup.....	56

5.2. Software.....	61
5.3. Frequent problems.....	63
5.4. Additional studies.....	65
6. IMAGING OF NONUNIFORMITIES.....	67
6.1. Mechanical defects in ZnO monocrystal.....	67
6.2. Point defects in ZnO nanorods.....	70
6.3. Effects of FIB etching on ZnO monocrystal.....	79
6.4. Gallium doped ZnSe monocrystal.....	84
7. MEASUREMENT UNCERTAINTY.....	103
8. SUMMARY.....	106
BIBLIOGRAPHY.....	109
ACKNOWLEDGMENTS.....	114
SUPPLEMENT.....	115

1. Introduction

Measurements with light as a carrier of information are a relatively young development. Nevertheless it allowed us to break some of the most persistent stalemates in the history of science. The field theory was started with the description of light. The quantum physics was started with the description of light. Astronomical discoveries were always in great majority based on light measurements. Light seems to limit physics both from the infinitesimal – lack of the rest mass or size; and maximal – speed of light as the limit of information transition; extremes, and yet it constantly proves to be one of the most useful tools for science. It is only natural to reach for its possibilities once again, in another attempt to deepen our knowledge.

1.1. Semiconductors

It is safe to say that semiconductor materials are present in daily lives of almost every human being since the silicon revolution in the middle of the previous century, mostly in the form of the electronic devices. However silicon in the field of electronics is not the only application of semiconductors that we encounter on a daily basis. While silicon usage is still the most common and growing in numbers ever since, we also observe a rapid growth, and more importantly, increasing market share of other semiconductor based devices. Light-emitting diodes use a wide range of other semiconductor materials, and are a common addition to the silicon based devices, in the form of indicators, screen backlights and various other applications. Another example would be the well-established solar cell industry, which also uses a very wide range of materials, including vast palette of semiconductor materials. Fields of spintronics and quantum computing are another examples of rapidly growing domains where researchers have to go beyond silicon, to find the most suitable solutions.

The most interesting semiconductors for their optical properties are the wide band gap semiconductors, which is a common name for materials with a band gap in 2 to 4 eV range. Thanks to this property, such materials are suitable for a highly demanded control over the electromagnetic field in the ultraviolet and visible (UV-vis) spectral range. Modern development of this class of materials started in the early 90's and can be attributed to two dramatic developments, namely the first blue-green laser diode [1] based on zinc selenide (ZnSe) and the invention of blue light emitting diodes (LED) made of gallium nitride (GaN)[2] as a luminescence material. Those two achievements alone greatly popularized the used semiconductors and centered the research community around them for many years.

Nowadays a full palette of wide band gap semiconductors is under constant research in hope to improve efficiency and parameters of the commonly used devices. Among those arousing the greatest interest we can name the two semiconductors mentioned above, as well as zinc oxide (ZnO) which found a wide range of applications in such fields as solar cells [3], LED [4] and spintronics [5], silicon carbide (SiC) which is found in electronic devices operating under extreme heat and voltage conditions, and aluminum nitride (AlN) exhibiting significant piezoelectric properties, making it especially popular in the field of mechano-acoustics [6].

1.2. Motivation

Regardless of the material and its applications, a quality of the crystalline structure is always a major concern. Small change of a single property of the semiconductor, like a slight change of the width of the band gap can render the whole batch of the product useless. Quality of the crystalline structure affects all the properties of the semiconductors, be it mechanical, physical or chemical. That is why the homogeneity of the material and the repeatability of the manufacturing process in a very small error range is of the utmost importance.

However different units manufactured under the same conditions, even in the same batch, can exhibit vastly different semiconducting properties [7]. Due to the seemingly random character of some of the production parameters, the sources of inhomogeneity are difficult to determine and eliminate. Modern manufacturing methods get constantly better at producing homogenous semiconductors, and a development of a reliable method which would allow to precisely identify and track all classes of crystalline defects would extensively contribute to the quality assurance of the modern devices.

Currently, there is no method of three-dimensional imaging and differentiation of the defects and doping in wide-band gap semiconductor crystals. The field is overwhelmingly underdeveloped due to the focus on planar structures for the past decades. However, the limitations of the planar structures are already noticeable and the trend is shifting towards the three-dimensional solutions [8-10]. This novel approach will drive the researchers to develop a suitable techniques capable of providing an insight into three-dimensional semiconductor solutions. With this dissertation, author hopes to contribute to the early stage of this new era.

1.3. Objective

The objective of this dissertation is to develop and evaluate a method of tracking and three-dimensional in-volume imaging of defects and impurities present in wide band gap semiconductors for the quality assurance of manufacturing and processing.

For this goal we chose the two-photon fluorescence microscopy, which allows three-dimensional imaging and exhibits deep penetration abilities. Additionally, by the spectral filtration of wavelengths attributed to specific radiative centers, it is possible to differentiate and image defects of interest.

To evaluate the extent of possibilities and limitations of this method, we present the results of our studies over several popular wide band gap semiconductors in various forms,

including ZnO monocrystals, ZnO nanorods, ZnSe monocrystals, cadmium sulfide (CdS) nanostructures and titanium dioxide (TiO₂) monocrystals.

1.4. Dissertation Structure

The dissertation is organized into a logical flow of defining needs, followed by a proposal of solution, the objective of the study, the theoretical background, introduction of developed tools, validation of the system, and confirmation of the objective fulfillment with the extensive test of various samples under differing goals.

Chapter 1 provided an introduction of the current challenges and possible development directions, as well as stating the objective of the study. Chapter 2 focuses on two-photon microscopy method introduction with subchapters on theoretical background, modern advances and extensive theoretical explanation. Additionally a comparison with alternative methods is presented. Chapter 3 is dedicated to a proposed advancement of the basic two-photon method with spectral filtering, and introduction of its capabilities. Chapter 4 introduces the materials under study, with an analysis of the properties and limitations concerning the semiconductors that are possible to study with the presented method. Furthermore, an analysis of studied native point-defects in ZnO are presented and analyzed focusing on systems resolving capabilities for mapping of these defects. After this chapter, the focus of the dissertation is centered on the performed studies and developments.

The developed system, and methods used for confirmation and additional studies is presented in chapter 5, which gives an overview of the used two-photon microscope, its software, and possible problems encountered during measurements. This chapter also introduces the technical data of all of the measuring devices which were performed for the goal of determination and confirmation of the properties of the studied materials.

Chapter 6 is the main chapter of this dissertation. It contains multiple subchapters presenting all of the performed studies and results, for each of the used materials and

objectives. Subchapter 6.1 is dedicated to imaging of mechanical defects in ZnO monocrystals. Subchapter 6.2 is focused on mapping of the native point-defects in ZnO nanorods. Subchapter 6.3 presents further insight into material profiling of ZnO monocrystals, by focusing on purposely introduced patterns achieved with focused ion beam etching method. Finally subchapter 6.4 demonstrates the three-dimensional doping volume imaging of the developed method, on an example of gallium doped zinc selenide monocrystal.

Chapter 7 provides a comprehensive overview of the achieved results and discussion on the usefulness and possible applications of the method, as well as the challenges of implementation of the method in the semiconductor industry.

2. Two-photon fluorescence microscopy

2.1. Historical background

The theoretical basis of multi-photon microscopy was developed by Maria Gopper Mayer in 1930, when she predicted in her doctoral dissertation that a single energy transition of an electron can be initiated by an absorption of energy of multiple particles [11], if the energy is transferred in a short enough time, namely if the temporal separation between the incidents is lower than 10 attoseconds. Her prediction required unachievable at the time energy densities to observe, and therefore it was impossible to undeniably prove it for over 30 years. Until the development of one of the greatest inventions in physics, lasers.

Shortly after that, in 1961, the multi-photon excitation has been proven experimentally in the work of two American physicists, Wolfgang Kaiser and Charles Garret [12]. However the path to practical applications was not so clear at that time. Since as mentioned above, multi-photon excitation requires a simultaneous absorption of energy of multiple particles, effectively such particle density is only acquirable in the very center of a tightly focused beam. Effectively the excitation could occur only in a sub-micrometer volume, which was a limiting factor for any imaging technique available at that time.

It took another 30 years to implement multi-photon excitation to a much newer imaging technique, laser scanning microscopy. Laser scanning microscopy was first presented in the form of confocal scanning microscope by David Egger and Paul Davidovits [13] in 1969. The first to develop a scanning microscope with the implementation of multi-photon excitation was Winfred Denk [14], and his work was published only as recently as in 1990. However the field developed quickly, since this new method shared many properties with the already well-established confocal scanning microscopy, and could draw from its solutions.

2.2. Modern advances

Introduction of the two-photon technique of imaging caught a substantial interest. Desire to improve the technique by the researching community is owed to the ability of a deep in-volume analysis of the scattering mediums, which is a unique and exceptional property. Other optical methods capable of penetrating deep into the sample include X-ray imaging [15], magnetic resonance imaging [16] and various tomography methods [17] including optical coherence tomography (OCT) [18]. All of these methods incorporate ballistic particles as the carrier of information about a distribution of some property of the studied sample, i.e. scattering, refractive index etc. Unlike two-photon and coherence imaging, those methods incorporate a non-direct, mathematical methods of reconstruction of a three-dimensional image of the sample [19], based on a series of two-dimensional images. Such approach forces an extended time of processing between data acquisition and assessment. Prolonged delay is unacceptable for mass numbers that are present in today's manufacturing. Listed methods found their use in medical applications, where the process time is measured in hours and days, not milliseconds.

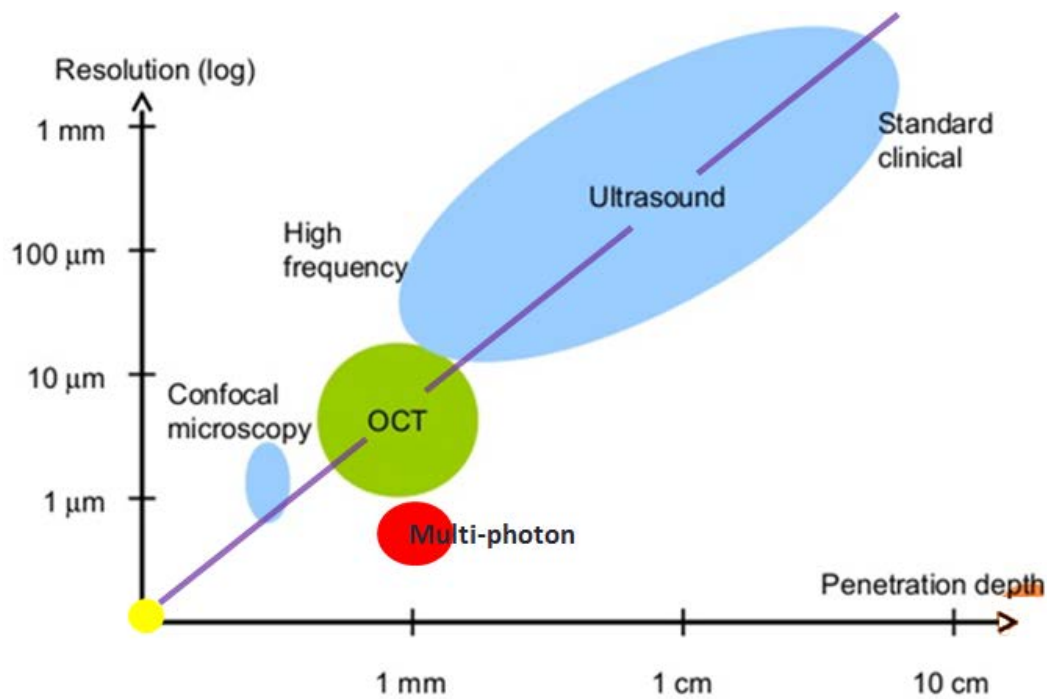


Fig. 2.1 Comparison of in-bulk imaging methods. Purple line indicates an expected resolution to depth of imaging ratio.

Due to the use of ballistic particles, methods like X-ray tomography can provide a depth of imaging well into the range of centimeters. This ability is a trade-off, and the cost is reduction of resolution. Achieving a resolution comparable with fluorescence methods limits the depth of imaging to the sub-micrometer range [20], and therefore renders this techniques not suitable for most of the needs.

Modern multi-photon systems allow imaging at depths over 1000 μm [21]. To achieve such impressive abilities, various methods have to be incorporated, including selection of the excitation wavelength and optimization of the energy density at the focal point. Generally longer wavelength allows for a deeper imaging of the sample, however in the case of autofluorescence the range of available wavelengths is limited by the studied sample, and if the specially designed dyes are utilized, which is usually the case for biological specimens, other factors come into play, like blood and water absorption spectra, which limits the excitation wavelength to around 1300 nm [22]. The energy density at the focal spot also

cannot be increased indefinitely, not only because of the availability of the high intensity sources, but also due to the increased excitation probability at out-of-focus planes of the sample. This leads to degradation of the image. The planes most prone to excitation with the out-of-focus beam are in the imminent vicinity of the focal spot, which results in deterioration of the resolution, as well as the surface plane of the sample, which might result in obscuring of the image with the surface-related artifacts. Both those effects require a careful optimization of the excitation beams intensity.

Another trade-off is present at the speed of acquisition of the two-photon images. Various methods were demonstrated which allow for real-time two-photon imaging of two-dimensional planes [23, 24], however all of these methods exhibit a drastic decrease of the contrast and imaging depth of the obtained images. This is due to the short time of irradiation and detection at the single focal point, which is a result of the required scanning speed, and overall lowered average energy density which is a result of the proposed excitation beam splitting techniques, introduced in order to obtain a parallelized imaging process by the irradiation of multiple foci [25, 26]. Such systems also require utilization of a matrix detector, like CCD, to determine the positions of each of the focal points. Matrix detectors are known for a lower sensitivity of the sensing system, than point detectors, like PMT, which contributes to further contrast deterioration.

Modern multi-photon imaging developments target mostly biological applications [27-31]. This is due to the complexity of such specimens and an ability of this technique to resolve various properties of the sample, even with a single scan. Multimodal imaging is currently a standard in organic tissue laboratory studies. This technique utilizes various fluorescent dyes to image different class of tissues. Fluorescent dyes of different spectral response are applied to the specimen and attach to the according tissues. During the imaging, each of the fluorescent dyes is separately excited and separately imaged, by the use of spectral filtering. To obtain the excitation of different fluorophores, different methods might be used. The fluorophores might be irradiated with different light sources, with wavelength corresponding to the absorption spectrum of each dye. Fluorophores might also be excited by the same source, but with different order of multi-photon process – most commonly two-photon and

three-photon processes. Probability of occurrence of higher order multi-photon excitation decreases over 10^5 times with each level, however the capabilities of forth [32] and fifth [33] order nonlinear excitation are actively investigated.

The developments in the multi-photon semiconductor imaging are scarce, in contrast with the studies on biological tissue. The studies concerning semiconductors and multi-photon processes tend to focus either on the spectral properties of the material [34-36], or on the use of semiconductors as the source of entangled photons for quantum information processing applications [37, 38]. Studies performed in our laboratory [39, 40] are among the narrow number of publications in this field.

2.3. Theoretical basis

The mechanism of the N-photon excitation requires an involvement of N-1 virtual excited states with energies lying somewhere in between valence and conductive bands, also known as the band gap. This requirement is presented on Jablonski diagram on Fig. 2.2

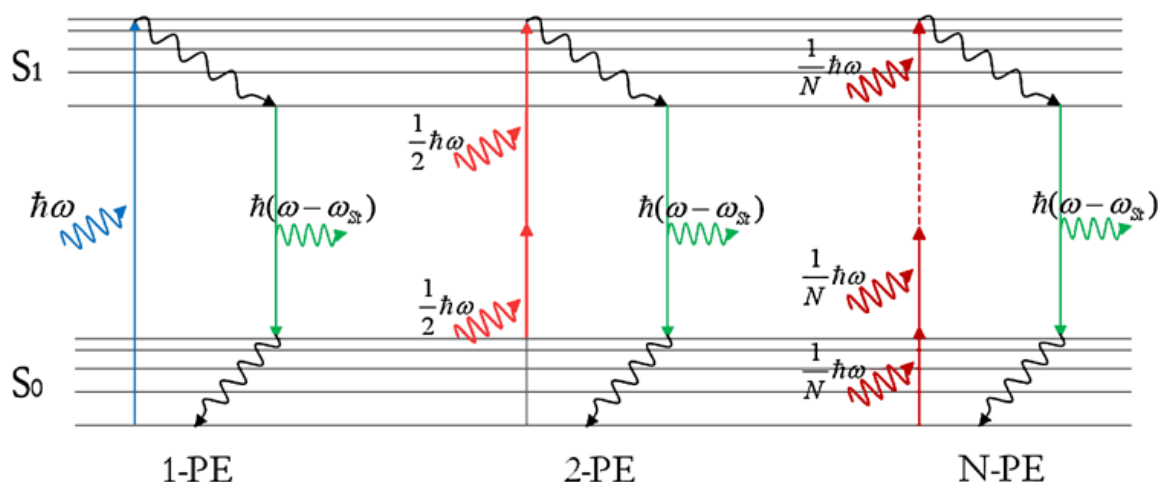


Fig. 2.2 Schematic depiction of one-photon (1-PE), two-photon (2-PE) and multiphoton (N-PE) excitation process. ω_{st} – Frequency resulting from the decrease of carrier energy due to the Stokes shift.

Since there are no existing bands in this energy range, an electron cannot remain in this virtual state for a prolonged time. Instead after the excitation finishes, electron immediately starts the process of energy emission. If no other events occur, such phenomenon is called dispersion. However if an additional energy transfer occurs, before the electron emits the energy and returns to its ground state, the molecule gets promoted to the final state, which is one of the states available in the conductive band. For this to occur, all photons required to achieve the sufficient energy, have to be absorbed in the timespan lower than 10 as. Such transition is regarded as a single quantum event. To calculate the probability of the occurrence of such event, an appropriate quantum system has to be considered. Such analysis is performed below.

Multi-photon excitation is a non-linear phenomenon characterized by the evolution of a quantum system consisting of three or more particles. As such, it is impossible to give an exact solution of its Schrodinger equation. However it is possible to give an approximate solution with satisfying precision with help of the perturbation theory, and its specialized successor, quantum field theory.

For the perturbation-free system, the Schrodinger equation in its most general form is:

$$H_0\psi_n = E_n\psi_n \quad (2.1)$$

Adding a small, first order perturbation to the system will result in a slightly modified Hamiltonian describing the system:

$$H' = H_0 + \epsilon H_1 \quad (2.2)$$

Where ϵ is a perturbation parameter with the value in the range of $0 < \epsilon < 1$. Hence, for the perturbed case, the Schrodinger equation can be written as:

$$(H_0 + \epsilon H_1)\psi_n = E_n\psi_n \quad (2.3)$$

If the perturbation parameter is not equal to 0, both eigenfunction and eigenvalue of energy has to be expanded:

$$\psi_n = \psi_n^{(0)} + \epsilon\psi_n^{(1)} + \epsilon^2\psi_n^{(2)} + \dots \quad (2.4)$$

$$E_n = E_n^{(0)} + \epsilon E_n^{(1)} + \epsilon^2 E_n^{(2)} + \dots \quad (2.5)$$

Where the superscripted numbering indicates the order of correction. To estimate the expectation value of the perturbing potential for the first-order correction, the appropriate

eigenfunction (eq. 2.4) and eigenvalue (eq. 2.5) have to be substituted in the perturbation corrected Schrodinger equation (eq. 2.3):

$$\epsilon H_1 \psi_n^{(0)} = \epsilon E_n^{(1)} \psi_n^{(0)} \quad (2.6)$$

Finding the solution for the eigenvalue of energy of the first-order correction leads to the following equation (in a bra-ket notation):

$$E_n^{(1)} = \langle \psi_n^{(0)} | H_1 | \psi_n^{(0)} \rangle \quad (2.7)$$

This term is a first-order energy shift related to the perturbation and it can be attributed to the probability of the single-photon absorption in a stationary state. By an appropriate selection of the excitation wavelength, the single-photon absorption cross-section can be minimized to a negligible value, and allows for maximizing the cross-section of two-photon absorption, describable by the second-order perturbation correction:

$$\begin{aligned} E_n^{(2)} &= \frac{\langle \psi_n^{(1)} | H_2 | \psi_n^{(1)} \rangle}{\epsilon} = \sum_{m \neq n} \frac{\langle \psi_n^{(0)} | H_1 | \psi_m^{(0)} \rangle \langle \psi_m^{(0)} | H_1 | \psi_n^{(0)} \rangle}{E_n^{(0)} - E_m^{(0)}} \\ &= \sum_{m \neq n} \frac{\left(\langle \psi_n^{(0)} | H_1 | \psi_m^{(0)} \rangle \right)^2}{E_n^{(0)} - E_m^{(0)}} \end{aligned} \quad (2.8)$$

While both terms given by eq. 2.7 and eq. 2.8 accurately represent the absorption cross-section in a stationary state of a particle under a static perturbation, we know that it is not representative for the real, time-dependent systems.

To solve the time-dependent Schrodinger equation, we will consider a Hamiltonian of time-independent system with time-dependent perturbation acting on it:

$$H' = H_0 + \epsilon H_1(t) \quad (2.9)$$

Therefore, the time-dependent Schrodinger equation for such system is:

$$i\hbar \frac{\partial}{\partial t} \psi(\vec{r}, t) = (H_0 + \epsilon H_1(t)) \psi(\vec{r}, t) \quad (2.10)$$

Following the steps of time-independent perturbation theory, the solution for the unperturbed time-independent Schrodinger equation in its classical form has to be modified by a perturbation parameter ϵ , to obtain a solution for the perturbed state:

$$\psi(\vec{r}, t) = \sum_n \sum_q \epsilon^q c_{nq}(t) |\psi_n^{(0)}(\vec{r})\rangle e^{-iE_n^{(0)}t/\hbar} \quad (2.11)$$

This solution can be then adopted into the time-dependent Schrodinger equation (eq. 2.10) [41]:

$$\begin{aligned} i\hbar \sum_q \left[\epsilon^q \frac{\partial}{\partial t} c_{mq}(t) - \epsilon^q c_{mq} \frac{i}{\hbar} E_m^{(0)} \right] e^{-\frac{iE_m^{(0)}t}{\hbar}} \\ = \sum_n \sum_q \left[E_n^{(0)} \langle \psi_m^{(0)} | \psi_n^{(0)} \rangle + \epsilon \langle \psi_m^{(0)} | H_1(t) | \psi_n^{(0)} \rangle \right] e^{-\frac{iE_m^{(0)}t}{\hbar}} \end{aligned} \quad (2.12)$$

where a coefficient c_{mq} is an amplitude of the corresponding eigenstate, which can be calculated by equating the terms for the perturbation order of interest. For the zeroth-order we obtain:

$$c_{m0}(t) = 0 \quad (2.13)$$

hence

$$c_{m0}(t) = c_{m0}(t = 0) = c_m^{(0)} \quad (2.14)$$

Accordingly for the first-order:

$$\frac{\partial c_{m1}(t)}{\partial t} = -\frac{i}{\hbar} \sum_n c_n^{(0)} \langle \psi^{(0)} | e^{\frac{iE_m^{(0)}t}{\hbar}} H_1 e^{-\frac{iE_m^{(0)}t}{\hbar}} | \psi_n^{(0)} \rangle \quad (2.15)$$

Integration over time gives the searched coefficient:

$$c_{m1}(t) = -\frac{i}{\hbar} \int_{-\infty}^t c_n^{(0)} \langle \psi_m^{(0)} | e^{\frac{iE_m^{(0)}t'}{\hbar}} H_1 e^{-\frac{iE_m^{(0)}t'}{\hbar}} \sum_n c_n^{(0)} | \psi_n^{(0)} \rangle dt' \quad (2.16)$$

Solution for the second-order perturbation integrated over time and with implemented solution for the first-order:

(2.17)

$$\begin{aligned} c_{m2}(t) \\ = -\frac{1}{\hbar^2} \int_{-\infty}^t \int_{-\infty}^{t'} \sum_n c_n^{(0)} \langle \psi_m^{(0)} | e^{\frac{iH_0 t'}{\hbar}} H_1 e^{-\frac{iH_0 t'}{\hbar}} | \psi_n^{(0)} \rangle \langle \psi_n^{(0)} | e^{\frac{iH_0 t''}{\hbar}} H_1 e^{-\frac{iH_0 t''}{\hbar}} \sum_n c_n^{(0)} | \psi_n^{(0)} \rangle dt'' dt' \end{aligned}$$

Presented solutions are the probability amplitudes of the perturbations in the system. Zeroth order represents a perturbation-free system, while higher orders represent respectively one-photon and two-photon transition probability amplitude. It is possible to calculate higher probability densities for other multi-photon interactions. However for the

purpose of this dissertation, presented precision is satisfying, since the absorption cross-section of the higher order interactions is minimized by the wavelength choice.

The transition probability for the single-photon case can be calculated as the absolute square of the corresponding probability density [41]:

$$P_m^{(1)} = c_m^*(t)c_m(t) = \frac{2\pi}{\hbar} |\vec{\mu}, \vec{\xi}| \rho(\omega = \omega_{mn}) t \quad (2.18)$$

Where ρ is the density of the excited states, and ξ is a randomly polarized electric field related with the light intensity by the following formula:

$$I = \left[\frac{nc}{2\pi\hbar\omega} \right] |\vec{\xi}|^2 \quad (2.19)$$

where the $\hat{\xi}$ is the unit vector.

To calculate the transition rate of a single-photon excitation, the probability has to be derived over time:

$$r_{n \rightarrow m} = \frac{\partial}{\partial t} P_m^{(1)} = \frac{2\pi}{\hbar} |\vec{\mu}, \vec{\xi}| \rho(\omega = \omega_{mn}) \quad (2.20)$$

This allows to calculate the photon absorption cross-section, which relates the transition rate given by the above equation, with the light intensity:

$$r_{n \rightarrow m} = \sigma_{n \rightarrow m}^{(1)} I \quad (2.21)$$

By substituting both the transition rate and light intensity in the equation 2.21 with the solutions obtained in equation 2.19 and 2.20:

$$\sigma_{n \rightarrow m}^{(1)} = \frac{4\pi^2 \omega |\langle \psi_n | \vec{\mu}, \hat{\xi} | \psi_m \rangle|^2}{nc} \rho(\omega = \omega_{mn}) \quad (2.22)$$

For the two-photon case we have to start with second-order perturbation probability amplitude (eq. 2.17). By taking the similar steps to the one-photon case, we arrive at the two-photon transition probability [42]:

$$P_m^{(2)} = \frac{2\pi t}{\hbar} \left| \sum_k \frac{|\langle \psi_n | \vec{\mu}, \hat{\xi} | \psi_k \rangle| |\langle \psi_k | \vec{\mu}, \hat{\xi} | \psi_m \rangle| \xi^2}{\omega_{kn} - \frac{\omega}{2}} \right|^2 \rho\left(\frac{\omega}{2} = \omega_{mn}\right) \quad (2.23)$$

The relation between transition rate and the intensity of the irradiation is given by:

$$r_{n \rightarrow m}^{(2)} = \sigma_{n \rightarrow m}^{(2)}(\omega) I^2 \quad (2.24)$$

and therefore the two-photon absorption cross-section takes the form of:

$$\sigma_{n \rightarrow m}^{(2)} = \frac{2\pi}{\hbar^3} \left| \frac{\sum_k |\vec{\mu}_{nk}| |\vec{\mu}_{km}|}{\omega_{kn} - \frac{\omega}{2}} \right|^2 \rho\left(\frac{\omega}{2} = \omega_{mn}\right) \quad (2.25)$$

as can be seen from the equation 2.24, the transition rate is proportional to the square of the irradiation intensity, and since the distribution of the Gaussian beam is given by:

$$I(r, z) = I_0 \left(\frac{w_0}{w(z)} \right)^2 \exp\left(-\frac{2r^2}{w(z)^2}\right) \quad (2.26)$$

The transition rate, and therefore the recombination intensity, is proportional to the fourth power of the inverse axial distance from the center of the beam.

$$r_{n \rightarrow m}^{(2)} \propto I_{pl} \propto \frac{1}{Z^4} \quad (2.27)$$

The above results lead to the numerous useful properties of the two-photon fluorescence.

From the equation 2.24 we can conclude that the proportion of the diameter of the area of the excitation to the energy distribution in the irradiation area is inversely squared. This property leads to the subdiffractional resolution of the two-photon method, which compensates for the diffraction limitations of the minimal size of the focal spot, twice as wide as in the conventional fluorescence microscopy.

The limitation to the central area of the focal spot holds valid in the axial direction. This gives an intrinsic ability of optical sectioning to the two-photon method, and renders it appropriate for the three dimensional imaging. The absorption cross-section in the two-photon case (eq. 2.25) is miniscule when compared to the one-photon case (eq. 2.22). The two-photon transition requires availability of two photons in the imminent vicinity, which has a much lower occurrence probability, than passing by a single photon. Because of that, the two-photon microscopy requires a much higher energy density. Proportion of a required energy density to achieve the same transition ratio is in the order of:

$$\frac{\chi^{(n+1)}}{\chi^n} \sim \frac{e}{4\pi\epsilon_0 a_0^2} \sim 5 \times 10^{11} \frac{V}{m} \quad (2.28)$$

Where ϵ_0 is the vacuum electrical permittivity, and a_0 is the Bohr radius.

Generally the intensity of the two-photon induced photoluminescence is much lower, than for the one-photon case under the similar irradiation parameters. However it does not contribute to a proportional increase in a signal to noise ratio, since the excitation and emission wavelengths are so broadly separated, and the task of the spectral filtering of the excitation light can be performed with a much higher effectiveness. However the sensitivity of the detector puts a requirement on the minimal detectable photoluminescence intensity,

which translates to the minimal density of the irradiation energy. This limitations will be considered in the further part of the dissertation.

2.4. Image formation and resolving abilities

Image formation in two-photon fluorescence microscope is achieved by the laser scanning microscopy methods. However the image formation dependence on the intensity for this kind of systems is identical to that of the conventional widefield microscopes [43]. The resolution of the conventional microscope can be estimated by finding the point spread function (PSF) which follows the classical derivation based on the theory of diffraction in the Fraunhofer region. Integral governing the propagation of wave function U in Fraunhofer limit approximation of an image of an arbitrary point P can be written as [44]:

$$U(P) = C \int \int_A e^{-ik(p\xi + q\eta)} d\xi d\eta \quad (2.29)$$

where ξ and η are the coordinates of a point in aperture.

To consider the resolving abilities of the two-photon fluorescence microscopy, the spatial distribution of the excitation probability as the function of the distance from the center of the focal spot has to be provided. As we know, the probability is squarely dependent on the intensity, which may be approximately represented as a single complex scalar wave function in the form of the formula:

$$I = |U|^2 \quad (2.30)$$

Hence, for circular aperture an intensity in the focal region of an aberration-free lens given in the axial and radial normalized coordinates:

$$I(u, v) = \left| 2 \int_0^1 J_0(v\rho) e^{\left(\frac{1}{2}iu\rho^2\right)} \rho d\rho \right|^2 \quad (2.31)$$

where

$$\begin{cases} u = 4kz \sin^2\left(\frac{\alpha}{2}\right) \\ v = krsin\alpha \end{cases} \quad (2.32)$$

Therefore the PSF for the two-photon case can be calculated by substituting the considered light beam by two-times lower frequency, and including the square dependency on the intensity:

$$I_{2P}(u, v) = I^2\left(\frac{u}{2}, \frac{v}{2}\right) \quad (2.33)$$

Which in the focal plane reduces to:

$$I_{2P}(v) = \left[\frac{2J_1\left(\frac{v}{2}\right)}{\frac{v}{2}} \right]^4 I_0 \quad (2.34)$$

As compared to the conventional microscope:

$$I(v) = \left[\frac{2J_1(v)}{v} \right]^2 I_0 \quad (2.35)$$

Where J_1 is a first order Bessel function.

This functions are compared on the Fig.2.3

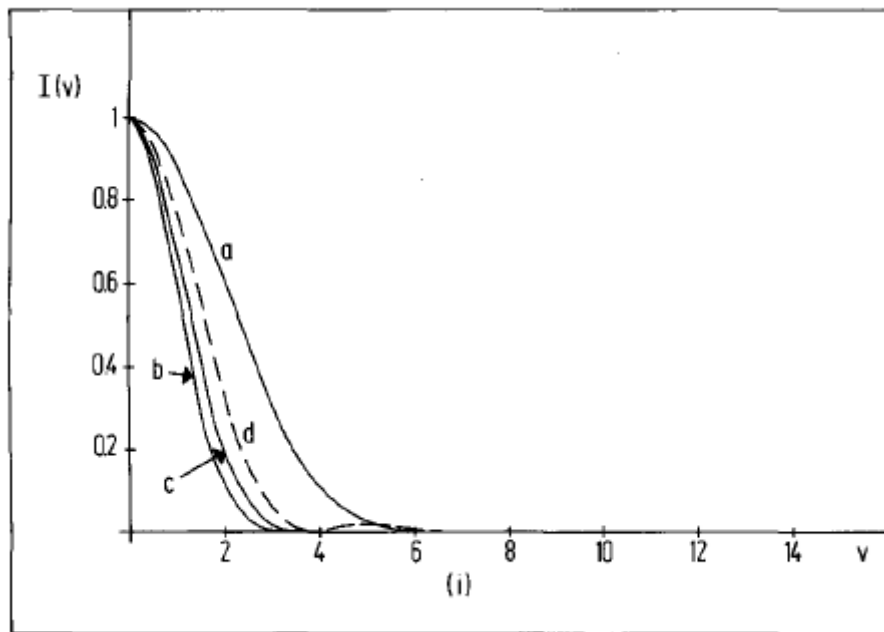


Fig. 2.3 Comparison of the intensity distribution along the lateral direction (a) two-photon absorption (b) confocal (c) two-photon confocal (d) classical microscopy. Source: Sheppard, C. J. R. (1996), Image formation in three-photon fluorescence microscopy. Bioimaging, 4: 124–128.

Since the minimum separation between two distinguishable points is dependent on the definition of distinguishability in regard to the expected contrast, there is some freedom in defining an absolute resolution. This results in an availability of a multitude of criterions which can be applied to compare various systems and calculate the resolving ability.

The most frequently used for the optical system, Rayleigh criterion, states that two points are resolved when the first minimum of one Airy disk is aligned with the central

maximum of the second Airy disk. This corresponds to a 26.4% contrast value between the imaged point's maxima and the separation area. Such requirement allows for adequate visual distinguishability of two closely spaced point. The first minimum of the Bessel function is present at the coordinate $x = 1.220\pi$. Over 85% of the total intensity is limited to the region enclosed by the circle of the radius x . This area is called Airy disk. For the quasi-monochromatic source of a wavelength λ , the radius of an Airy disk can be calculated from the formula:

$$r_{xy} = \frac{1.22\lambda}{2NA} \quad (2.36)$$

where NA is the numerical aperture of the objective.

However, as can be noticed on Fig. 2.3, the PSF in the two-photon case is noticeably wider, because of the requirement of two times longer wavelength. As noted before, the two-photon excitation occurs in a square proportion to the intensity of the laser beam. Combining it with the quadratic decrease of the intensity with the distance from the focal plane results in a fourth power decrease in the probability of the excitation with the increasing distance from the center of the focal spot. Thus the conventional formula has to be modified, by both, the changed wavelength, which broadens the effective focal spot, and the squared dependence of the excitation probability, which reduces the spot:

$$r_{xy2P} = \frac{0.383\lambda_{2p}}{(NA)^{0.93}} \quad (2.37)$$

To consider the axial direction, the axial response has to be calculated. This can be done by integrating the intensity of the single point image over the axial direction [45]:

$$I_{2P}(u) = \int_0^\infty I^2\left(\frac{u}{2}, \frac{v}{2}\right) v dv \quad (2.38)$$

Since conventional microscopy does not provide any optical sectioning, this is compared with a confocal fluorescence microscopy axial response on Fig 2.4

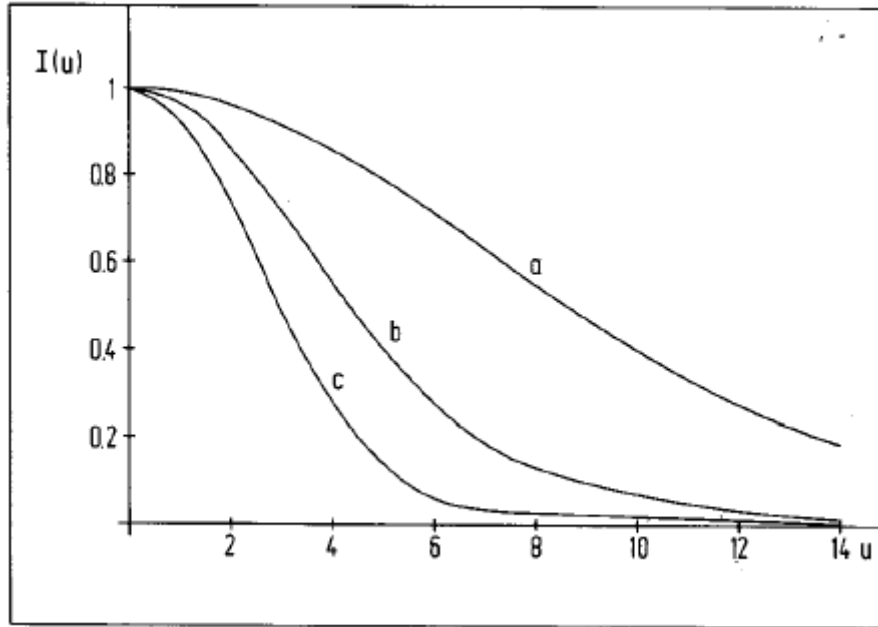


Fig. 2.4 Comparison of the intensity distribution along the axial direction (a) two-photon absorption (b) confocal (c) two-photon confocal Source: Sheppard, C. J. R. (1996), Image formation in three-photon fluorescence microscopy. *Bioimaging*, 4: 124–128.

This response results in an axial resolution equal:

$$r_{z2P} = \frac{0.626\lambda_{2p}}{n - \sqrt{n^2 - (NA)^2}} \quad (2.39)$$

This intrinsic optical sectioning can be observed in Fig. 2.5 presenting an image of powdered ZnO imaged with the reflected light laser scanning technique and the two-photon technique.

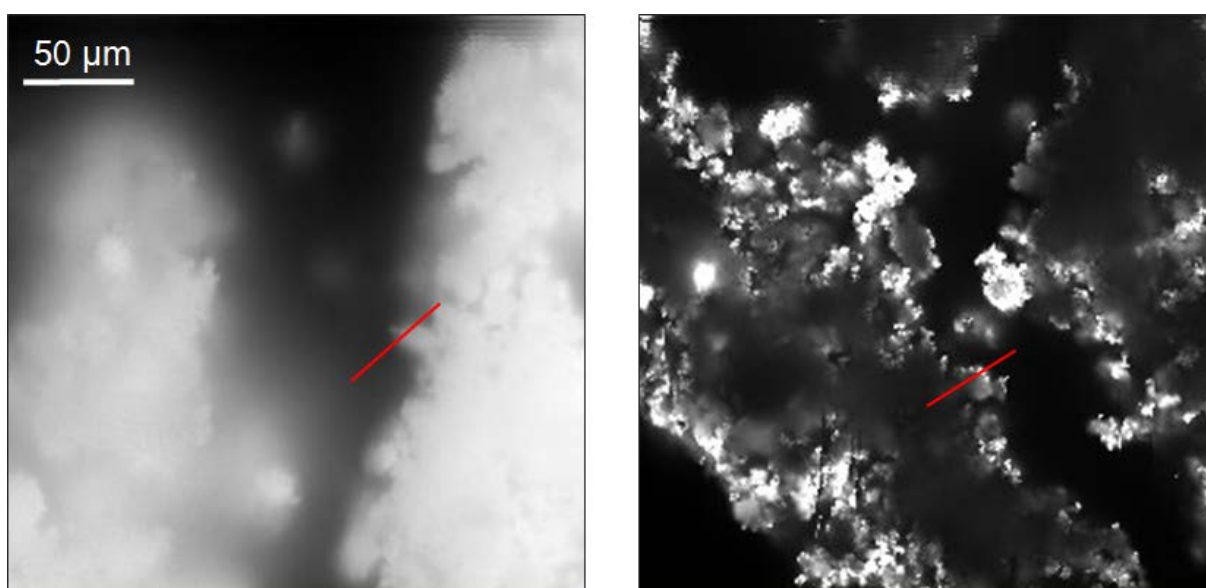


Fig. 2.5 Laser scanning image of zinc oxide, a) reflected light image, b) two-photon fluorescence image.

It is clear that the sharpness of the edges improved at the presented images which is a result of the natural filtering of the out-of-plane signal. To compare this improvement quantitatively, the intensity profile of red line markers in Fig. 2.5 are presented in Fig. 2.6. In the intensity profile taken from the reflected light image an out-of-focus signal affects the steepness of the intensity curve and leads to uncertainty as to the actual location of the edge of the sample.

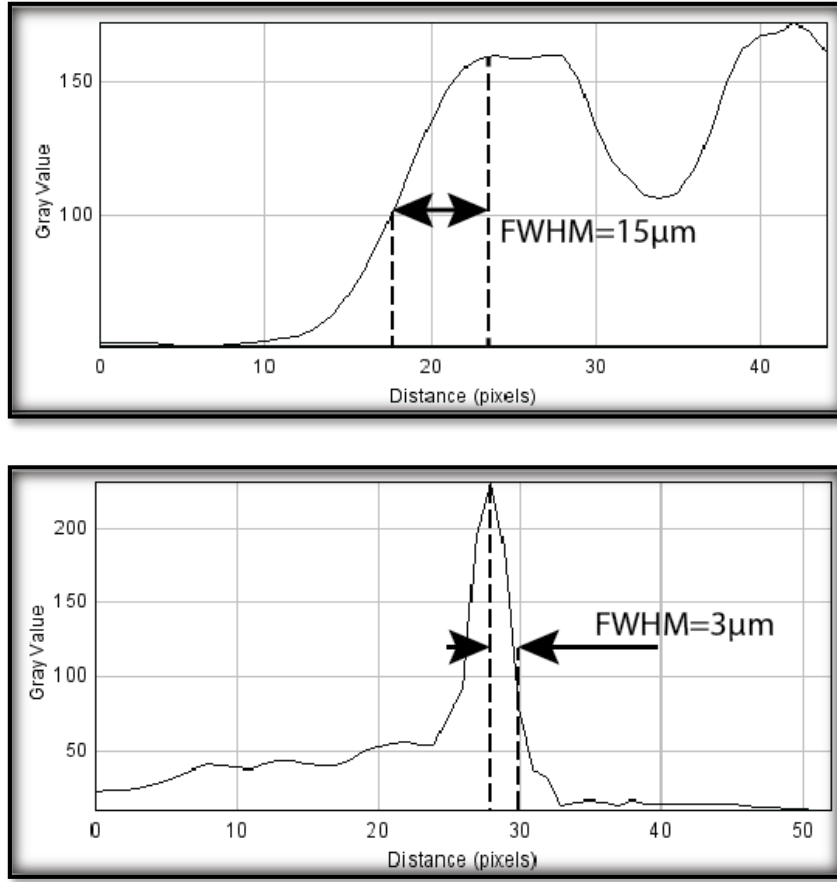


Fig. 2.6. Comparison of the fidelity of edge imaging of intensity profiles at the markers shown in Fig.2.5 (a) Reflected image (b) two-photon case.

And for comparison, the axial resolution in confocal fluorescent microscopy is given by:

$$r_{zc} = \frac{0.88\lambda}{n - \sqrt{n^2 - (NA)^2}} \quad (2.40)$$

As we can see, while due to the squared dependence on the excitation intensity the lateral resolution would improve for the same wavelength in a two-photon case, in reality it decreases when compared with other imaging methods due to the use of the longer

wavelength. However this deterioration of the resolving ability is not significant and does not negate other advantages of the multi-photon system. The obtained equations 2.33 and 2.35 will be used in the further part of this dissertation, to optimize the imaging parameters of the developed system.

It has to be noted, that in the two-photon case an increase in the excitation beam intensity results in broadening of the high excitation probability area inside the volume of focal spot. Both axial and lateral resolutions suffer due to that effect if the intensity is increased above the moderate intensity. Deeper analysis and an impact on the resolving abilities of the actual system are studied in the further part.

2.5. Advantages of the two-photon method

The use of two-photon process provides multiple advantages for semiconductor imaging. This chapter will compare two-photon microscopy with the properties of another common method, confocal fluorescent microscopy.

From the analysis of resolution conducted above, we can conclude that in general case the resolution of two-photon microscope is inferior to that, of confocal fluorescence microscopy. However, in practical applications, the confocal system is more sensitive to alignment imperfections including the finite size of the pinhole and its placement in the light path. Those imperfections reduce the difference between the resolutions of these two systems. Yet it is apparent that a conventional two-photon system cannot surpass the confocal system's imaging abilities, and thus structures that cannot be resolved with confocal system, will remain unresolved in the two-photon system.

The real advantages of the two-photon system come due to the use of 2 times longer wavelength. Firstly, due to the lack of the suitable optical equipment for the ultraviolet (UV) and deep ultraviolet (DUV), it is problematic for other methods to obtain an excitation of the

fluorophores radiating in this spectral ranges. However the two-times longer wavelength, required for the two-photon excitation falls in the vis-IR range, for which most of the modern optics is designed. This unavoidable obstacle which results in severe limitation of other methods is non-existent for the multi-photon case.

Another advantage deriving from the use of a longer wavelength, is the superior penetration ability of the multi-photon systems. The excitation wavelength can be selected in such a way (Fig. 2.7), that it omits the high absorption range of the sample, resulting in a negligible absorption in the out-of-focus areas of the specimen.

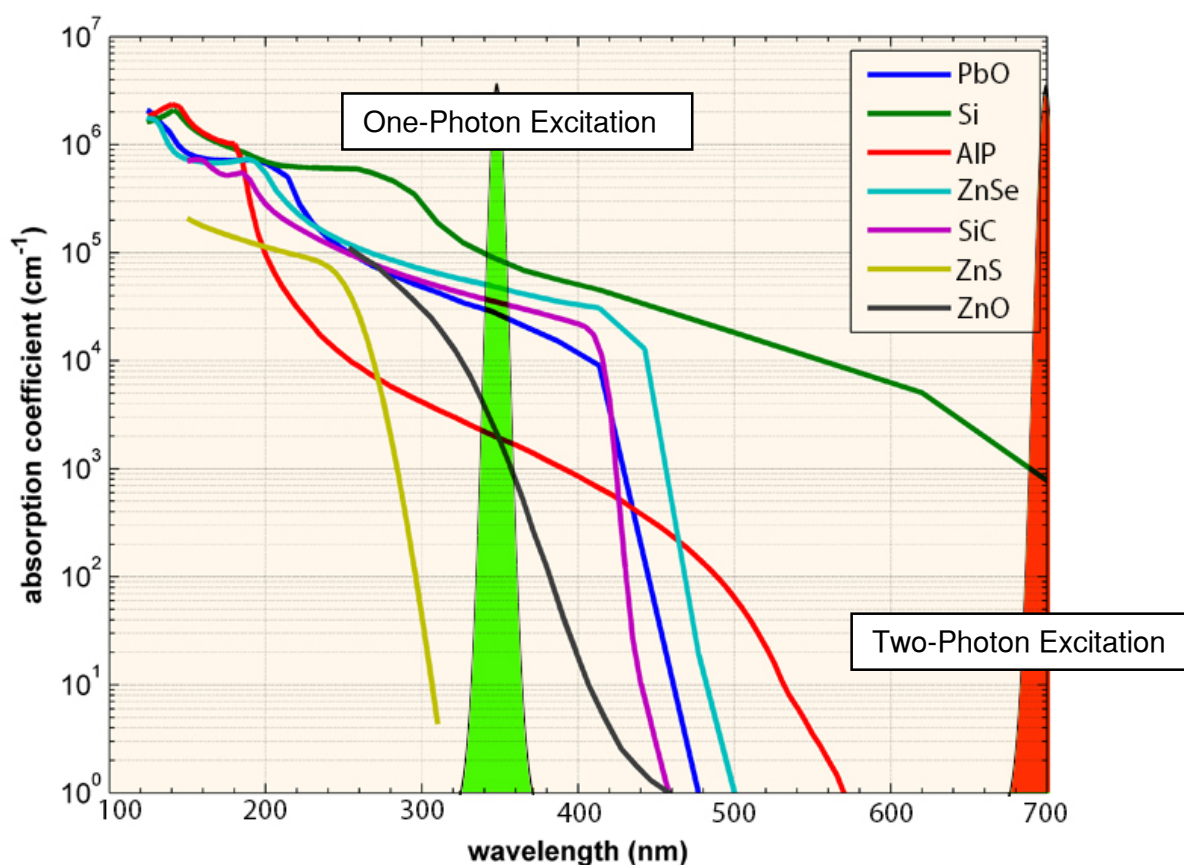


Fig. 2.7 Absorption spectra for various (marked on the image) wide band gap semiconductors with marked wavelengths required for conventional fluorescence (purple) and two-photon excitation (red).

To compare the penetration abilities of the two described method a comparative study was conducted. ZnO monocrystal was imaged both with confocal fluorescent microscope and the developed two-photon scanning laser microscope. The results for the confocal microscope are presented on Fig.2.8.

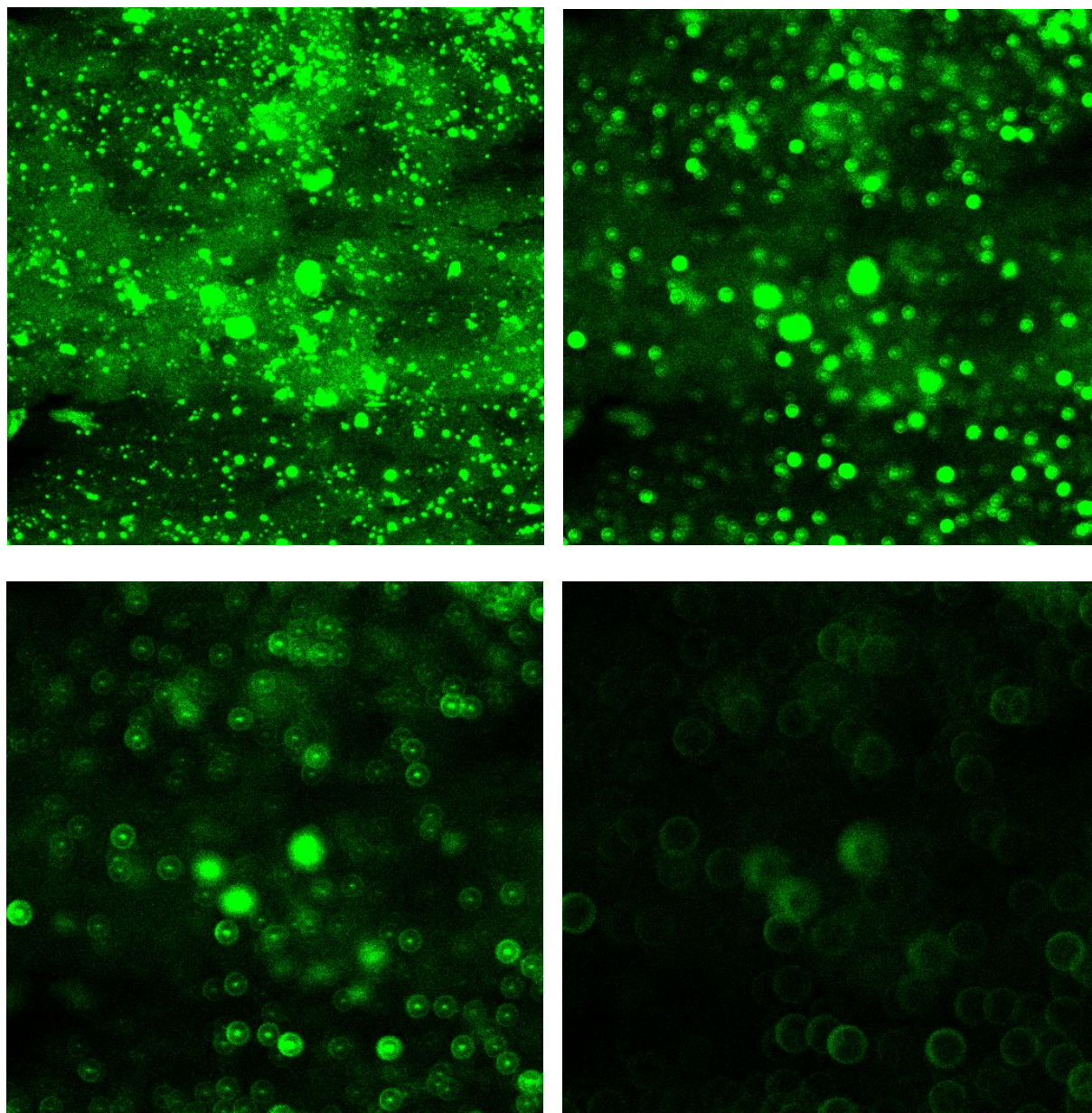


Fig. 2.8 Confocal images of the ZnO monocrystals, at different depth of imaging. (a) Surface, (b) 3 μm , (c) 6 μm , (d) 9 μm

As can be noticed, confocal imaging provides high axial resolution [46], however, as stated before, the excitation beam of the wavelength required for single-photon excitation is unable to penetrate the semiconductor effectively, and photoluminescence intensity together with resolution drops significantly at depths as shallow as 6 μm into the sample's volume. At 3 μm deep the average photoluminescence intensity at the image dropped by 22 %, and at 6 μm deep the intensity dropped by 48 % comparing to the value obtained at the surface. Intensity at the depth of 9 μm was below 1% of the initial intensity, and is considered below the point of distinguishability from noise. Roughness of the sample observed on Fig. 2.8 is a result of abrasion in the area, which was chosen purposely for the better depiction of the obtainable resolution.

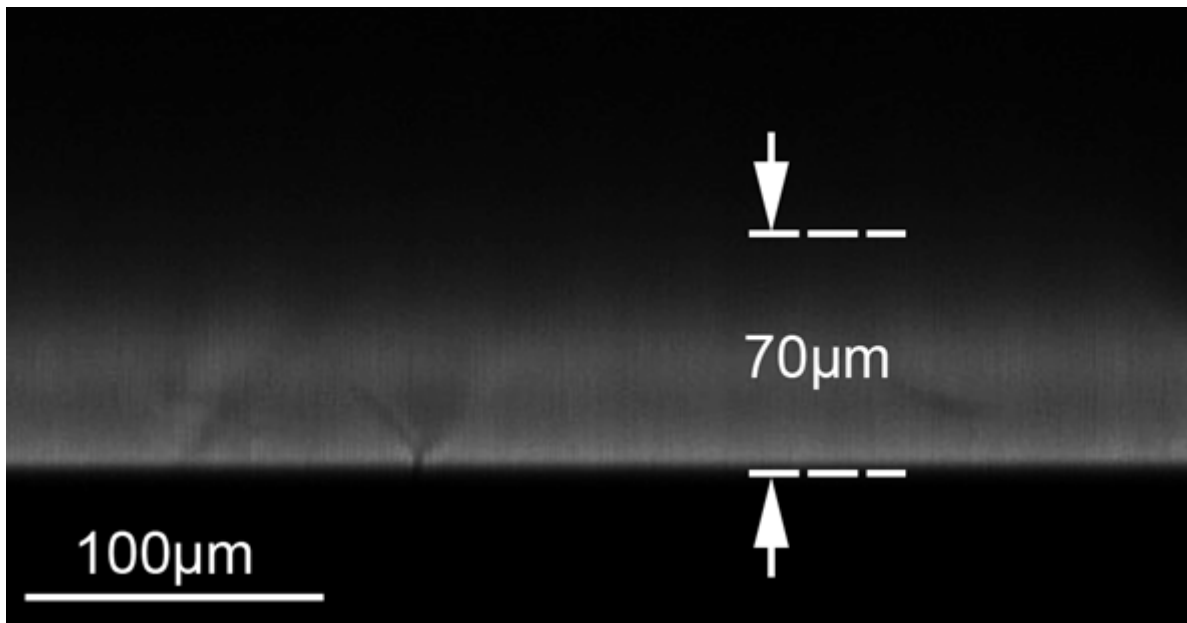


Fig. 2. 9 two-photon fluorescence image of X-Z cross-section of ZnO single crystal sample

In the case of two-photon fluorescence imaging of the same sample, 48% drop of the intensity observed at the surface was observed as deep as 70 μm inside the volume of the sample, which is presented on Fig. 2.9. Comparison of the results with the confocal image

reveals an over ten-fold increase in depth of imaging for the same sample. Lateral resolution is comparable.

Another major advantage of the multi-photon process is reduced phototoxicity, and therefore photobleaching effect on the samples. This property is especially important for the biological samples, because of their fragility. However the semiconductor samples also suffer from photobleaching [47] and to a higher degree, optical quenching [48].

The mechanism of photobleaching has to be explained on the quantum level. Excitation of a molecule leads to the promotion of an electron to an excited energy state. During the vibrational relaxation of the electron, there is a nonzero probability of an intersystem crossing from an excited state to a triplet state, instead of a desirable decay to the ground state. Triplet states have a long lifespan, compared to the excited state, and are extremely reactive. Such triplet state can react with the specimen and cause a degeneration or a rearrangement of the structure of the sample. For the biological specimens, additional negative effect of triplet states is the possibility of generation a singlet oxygen, which is harmful for the nearby molecules.

We have to realize, that for a conventional fluorescence microscopy and confocal fluorescence microscopy the excitation light interacts with all the planes through which it propagates, up to the focal spot and even beyond. It results in a probability of degeneration of all the molecules on its path, and leads to a considerable damage and photobleaching avoidable with the multi-photon techniques.

Exposure of the specimen to VIS-IR range of wavelength does not affect negatively its fluorescent properties, and therefore using such light beam for excitation does not produce any harmful effects outside of the focal spot.

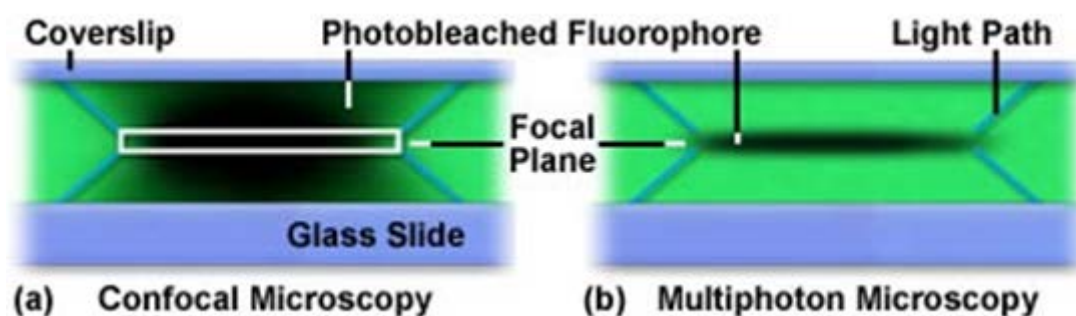


Fig. 2.10 two-photon fluorescence image of X-Z cross-section of ZnO single crystal sample.

Source: www.microscopyu.com

Photobleaching patterns presented on Fig. 2.10 result from the repeated imaging of the focal plane in a polymeric film stained with a fluorescent dye – Rhodamine. Black area shows the damage attributed to the photobleaching phenomenon. It is easy to notice that the affected area in the case of confocal imaging is multiple times wider in the axial direction than the imaged focal plane marked by the white rectangle. The blue lines represent the path of the irradiation beam through the film. In the multi-photon case, pictured on the right-hand side image, it can be clearly seen, that the damage is contained in the imaged area, since the only source of damage is, a much weaker than the excitation intensity, photoluminescence of the sample.

Decreasing the photodamage dramatically increases the viability period of the samples. The majority of the damage observed in the multi-photon case can be assigned to the excitation in the focal spot, as well as the reabsorption of the emitted light.

It is important to note that the population of the excited states does not differ, whether it is excited with single- or multi-photon process. Short pulsed lasers used for the two-photon excitation typically produces bursts of electromagnetic radiation in the order of 100 fs. Though it is indeed a short period of time, it is still a few orders of magnitude longer than the duration of the two-photon process itself, and therefore the electrons are excited in the exactly same manner as would it take place in a conventional fluorescence microscope with a continuous wave (CW) source.

3. Spectral resolving

The method of spectral resolving is based on the fact, that different radiative centers exhibit different band gap width, which results in a different wavelength of the photons emitted by the electrons recombining from the conductive band to the ground state of such radiative center. This property is exercised to differentiate between different sources of the radiation. Spectral filtering of the wavelength attributed to the defect of interest allows to image its distribution in the volume of the sample.

3.1. Kasha's rule

The phenomenon that allows for the differentiation of the radiative centers basing solely on the wavelength of the emission is called Kasha's rule, named after American spectroscopist Michael Kasha. It states that the radiative transition can take place only from the lowest excited state of a given multiplicity, to the ground state [49]. This phenomenon forces the excited electron to expend some of its energy through other mechanisms, before reaching the lowest band in the valence multiplicity, and results in a lower energy of emission than excitation – known as Stokes shift.

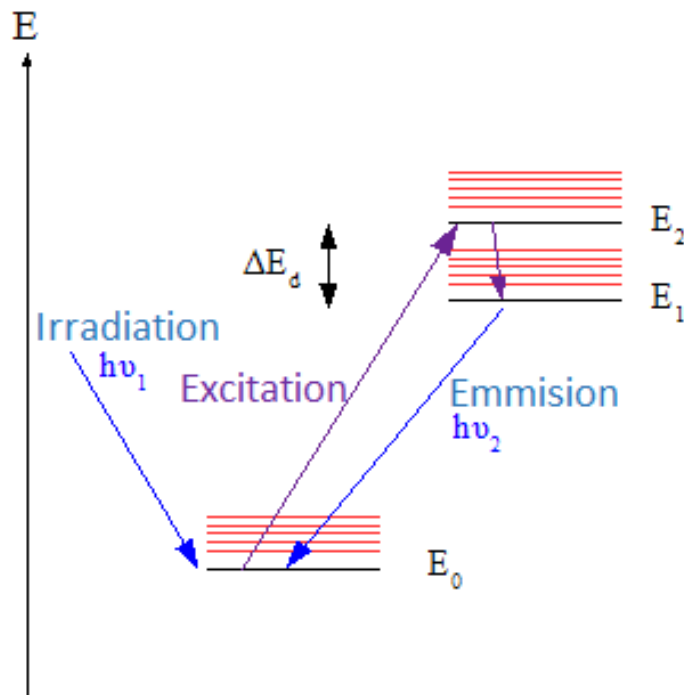


Fig. 3. 1 Graphical representation of the Kasha's rule on the Jablonski diagram.

Kasha's rule is critical for the spectral resolving, as it is the only mechanism providing the consistency of the radiation wavelength for each of the radiative centers present in the sample. If electrons could recombine from any of the excited states in the multiplicity, the range of the possible wavelengths for each defect or dopant would be too wide to distinguish it from the other peaks in the vicinity. Thanks to the phenomenon described by Kasha's rule, emission wavelength is independent of the excitation wavelength.

3.2. Certainty assessment

As stated above, Kasha's rule ensures that the recombination always takes place from the same excited state. However other phenomena can affect the wavelength of the emitted photon. Among other, thermal effects play the most important role in the broadening of the emission peak. The temperature of environment does not affect the Kasha's rule, however it modifies both the valence and the conductive bands energy by changing the rested and excited electrons kinetic energy, and rising both of them. The energy dissipation of the environmental heat is hard to assess and constantly fluctuating. The average speed v of the molecule in gas is given by thermodynamic formula:

$$\frac{1}{2}mv = kT \quad (3.1)$$

The number of molecules exhibiting this velocity can be estimated by the use of Maxwell's Law of distribution, for the x component of the velocity.

$$dN(v_x) \propto \exp\left(-\frac{mv_x^2}{2kT}\right) dv_x \quad (3.2)$$

This velocity component's distribution is described by the Gauss function. The gas particles affect the specimen's particles by colliding with them, and transferring part of their energy. This both raises and blurs the energy states in the sample and leads to a Doppler shift of the frequency of the emitted photons. In common laboratory conditions, it is the strongest phenomenon affecting the peak broadening. It has to be noted, that it is enough to consider a single, freely selected component of the velocity, since the measurements are generally taken directionally, along a chosen axis of imaging.

Another source of the broadening of the peaks is the uncertainty principle. Because of that limitation of the physical world, the energy levels of the quantum system are not infinitely sharp. Let's consider a short-lived state m . For such state, the uncertainty of its energy is proportional to its lifetime:

$$\Delta E \propto \frac{\Delta t_m}{\hbar} \quad (3.3)$$

Such short-lived state has an inversely proportional energy uncertainty, which affects all the electrons promoted to this state. An uncertainty of the frequency of a photon emitted by such electron is given by:

$$\Delta \nu \propto \frac{\Delta E}{h} \sim \frac{1}{2\pi\Delta t} \quad (3.4)$$

As we can see, the shorter lifetime of an excited state, the broader the peak of emission of the radiative center.

The peak clarity suffers also from the Lorentzian movement, which is known as natural broadening of the emission linewidth. If the spontaneous decay of an atomic state m degenerates to the lower energy levels n with a rate:

$$\gamma = \sum_n A_{mn} \quad (3.5)$$

then the line profile of the radiative recombination can be given by:

$$\phi(\nu) = \frac{\frac{\gamma}{4\pi^2}}{(\nu - \nu_0)^2 + \left(\frac{\gamma}{4\pi}\right)^2} \quad (3.6)$$

This line profile, known as the natural line profile is presented on the fig. 3.2.

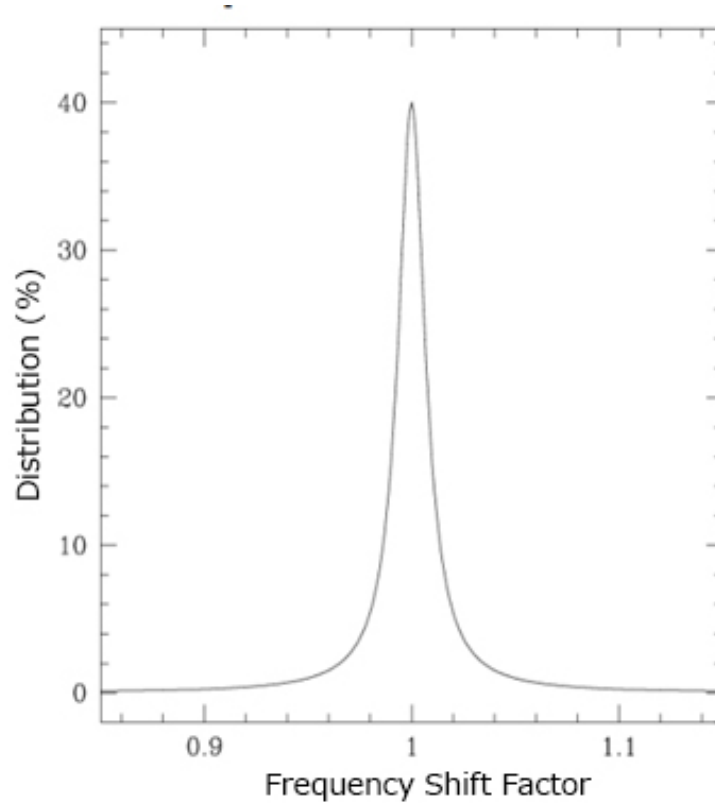


Fig. 3. 2 Natural line profile due to the Lorentzian motion of the electrons.

As we can see the decline is much steeper than the usually observed Gaussian profile of the spectral lines. This effect is present in all observed spectral measurements, however usually it is not a dominant source of the peak broadening, and it can be covered by other, stronger effects.

All of the described phenomena contribute to the widening of the individual peaks by a considerable value. Peak broadening can, and usually do lead to the peak overlapping, like presented on the spectrum of ZnO nanorods on the Fig. 3.3 where we can observe multiple

peaks separated by couple tens of nanometers in wavelength. As can be seen, filtering and acquisition at a maximum of a single peak leads to the partial acquisition of the overlapping peaks. The contribution of an overlapping peak depends on both the overlap width and the proportion of the intensities of each peak. Depending on this contribution in a sample of interest it must be decided if the overlap is negligible, or if it has to be taken into account and subtracted numerically.

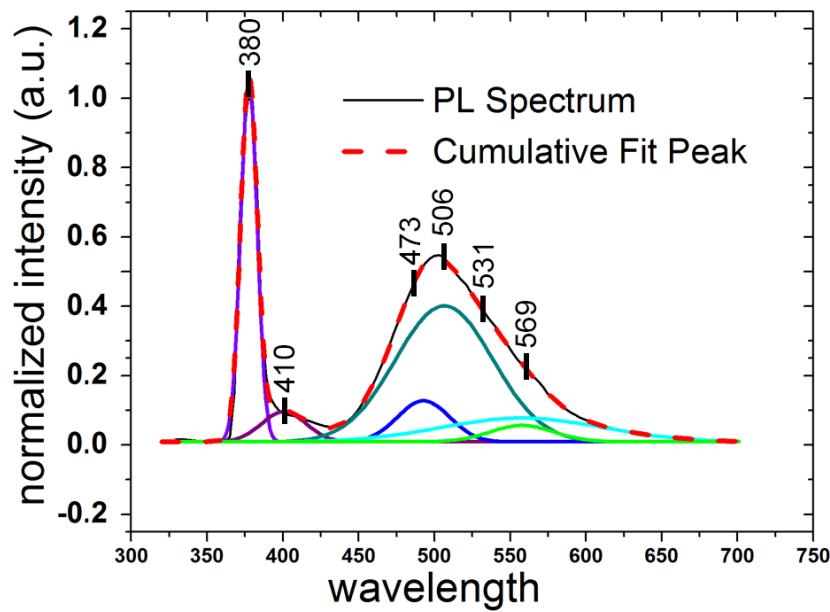


Fig. 3. 3 Photoluminescence spectrum of fluoride-containing phosphate-based glasses nanorods with Gauss fit peaks.

4. Semiconductors and defects

4.2. Semiconductors under study

As stated in the introduction, the study's focus is on the so called wide band gap semiconductors. Precisely, the semiconductors with band gap in the range from 2.4 eV to 3.4 eV, or if expressed in the term of wavelengths, from 365 nm to 515 nm. This limitation is due to the range of adjustability of the available high-power femtosecond excitation light source. The semiconductors were also selected on the basis of the popularity in the industrial applications. Among the so defined semiconductors of interest, the ones that underwent the study with their respective band gap width are listed in the table 4.1. The absorption spectra of the used samples are presented in Fig. 4.1.

Table 4.1 Properties of the studied semiconductors.

No.	Chemical Name	Chemical Formula	Band Gap @300K	Type	Source
1.	Zinc Oxide	ZnO	3.30 eV	Direct	[50]
2.	Zinc Selenide	ZnSe	2.70 eV	Direct	[51]
3.	Titanium Dioxide	TiO ₂	3.23 eV	Indirect	[52]
4.	Cadmium Sulfide	CdS	2.42 eV	Direct	[53]
5.	Silicon Carbide	SiC	3.05 eV	Indirect	[54]
6.	Gallium Nitride	GaN	3.40 eV	Direct	[54]

Preliminary study was focused on establishing the excitation efficiency of the listed materials. Among those, ZnSe exhibited the highest photoluminescence when irradiated with

780 nm light. In fact, the intensity of this photoluminescence raised concerns about the achievable resolution of the imaging while irradiated with the standard power of the light source used in the studies. Those concerns were addressed in chapter 6.4.

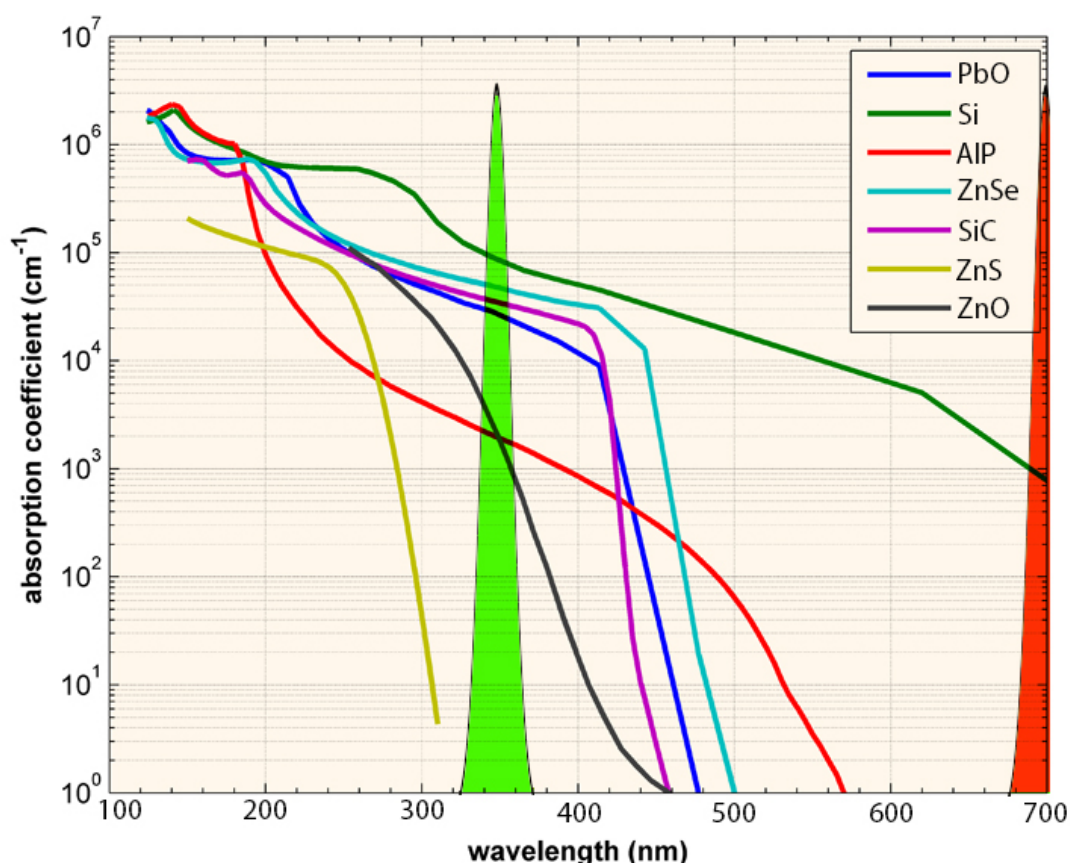


Fig. 4.1 Absorption spectra in wide band gap semiconductors with marked irradiation wave spectrum for one-photon (green) and two-photon (red) case.

Another semiconductor exhibiting efficient excitation under the conducted experiment's conditions was ZnO. While the intensity did not reach such levels as these of ZnSe, it was satisfactory for the purpose of the study. For the detailed evaluation of the developed system, ZnO in various forms, including monocrystals, nanorods and powder, was studied.

Remaining materials unfortunately did not reach the required excitation efficiency to be imaged in the developed system. Semiconductors exhibiting an indirect band gap did not

produce any photoluminescence, even under an irradiation with a wavelength matched to their absorption spectra. Radiative recombination in an indirect band gap semiconductors is an unlikely process, due to the requirement of virtual or excitonic transition states which are scarce, compared to the availability states required for non-radiative recombination.

Tested sample of GaN had an absorption edge beyond the reach of the used Ti:Sapp laser, and therefore was not excitable in the developed system.

The band gap of CdS on the opposite, is narrower than the adjustability range of the excitation beam. It was wrongly predicted, that the difference in the energy is still within the range of an available bound excited states. However lack of the photoluminescence proves otherwise, and it is impossible for the CdS electrons to absorb the energy of a photon from a 420 nm (840 nm for two-photon process) tuned source, since this energy does not correlate with excitation nor ionization.

4.3. Defects and dopants

The operation of semiconductors relies on their ability to modify electric and magnetic signals. This property is a result of their intrinsic and extrinsic electromagnetic characteristics. The most important attributes are band gap width, type of the semiconductor (n or p) and the available bands. All of these properties can be modified by dopants and defects, whether occurring naturally or introduced on demand. Most commonly the types of dopants and defects are distinguished with the use of spectroscopic methods, however following the Moore's law, it recently became possible to manufacture the electronic devices in atomic scale [55]. To image those nanoscale devices, surface imaging methods based on electron microscopy are usually incorporated. Among those we can name Scanning Electron Microscopy (SEM), Transmission Electron Microscopy (TEM), Scanning Tunneling Microscopy (STM) and Scanning Transmission Electron Microscopy (STEM). Exemplary images obtained from those devices are presented in Fig. 4.2. Those techniques provide superior resolution,

but an imaging area is limited to the surface of the sample. Furthermore, the resolution is affected by the conductivity of a studied material, and in case of the wide band gap semiconductors, charging of the sample by the electron stream significantly decreases SNR.

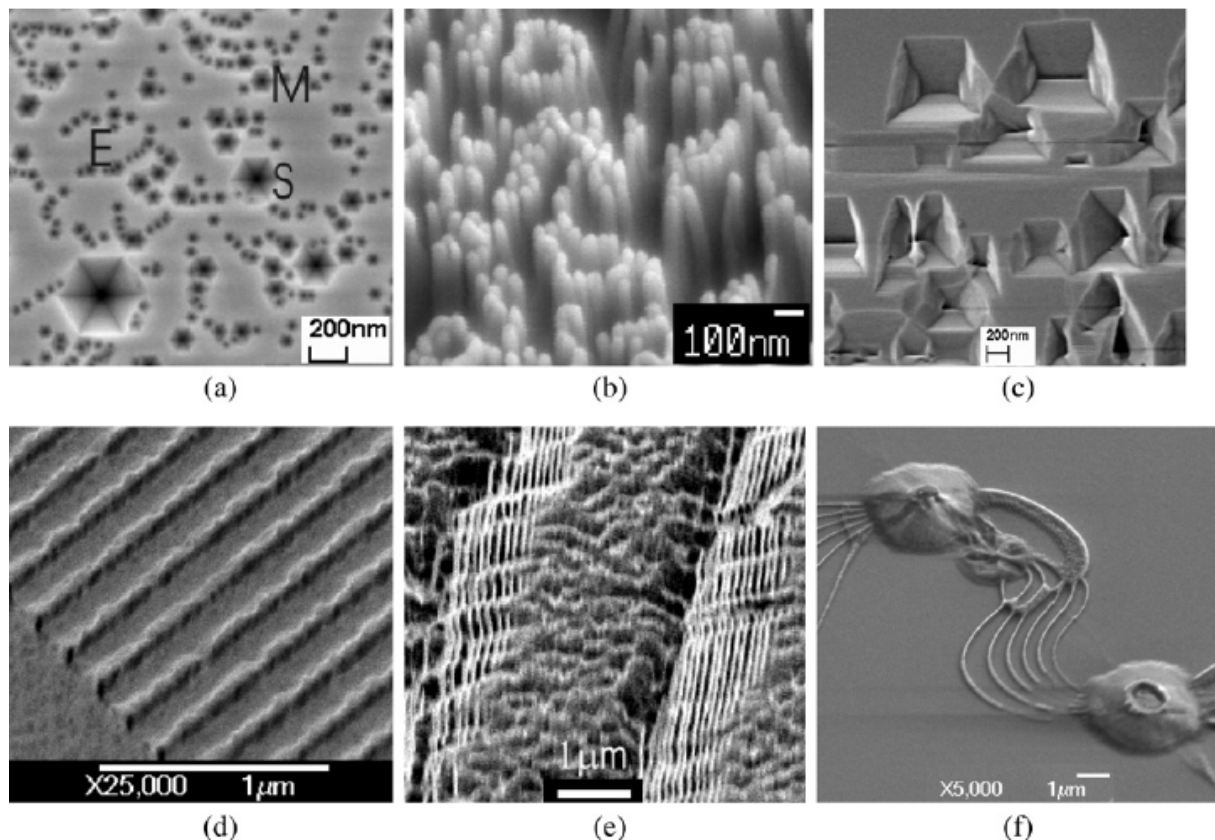


Fig. 4.2 SEM images of defects revealed in GaN (a–e) and SiC (f) by orthodox (a, c) and electroless photo-etching (b, d–f) methods. Source: Weyher, J. (2006). Superlattices and microstructures 40(4): 279-288.

Defects in semiconductors can be divided into mechanical and crystallographic defects. Mechanical defects are generally a bulk defects, affecting a volume at least two orders of magnitude larger than the periodicity of the crystal. Most commonly the mechanical defects are voids, lack of atoms in a volume considered to be a part of the sample. If the defects are located at the interface between the material of interest and its surrounding, they are classified as cracks with a suitable prefix indicating the size of the defect (micro-, nano-). The

same prefixes are used for the defects that are wholly confined inside the bulk of the material. In such case, the defects are classified as pores. While the mechanical defects do not modify the properties of semiconductor directly, they can affect processing and any structure located in its volume of occurrence. Due to this effect, it is important to track them and avoid manufacturing in the vicinity of such voids.

Crystallographic defects can be classified as three different types; point defects, line defects and planar defects. All of those types interrupt the periodicity of the crystalline structure of the semiconductor. Point defects occur at a single lattice point and do not extend into any dimension. The actual size of a defect that can be considered a point defect is not strictly limited, as long as the above conditions are met. Point defects are assisting virtually all diffusion processes in semiconductors [56] and therefore are extremely important to apprise the utility of the material. A multitude of point defects can be defined. The most common are presented in Fig 4.3.

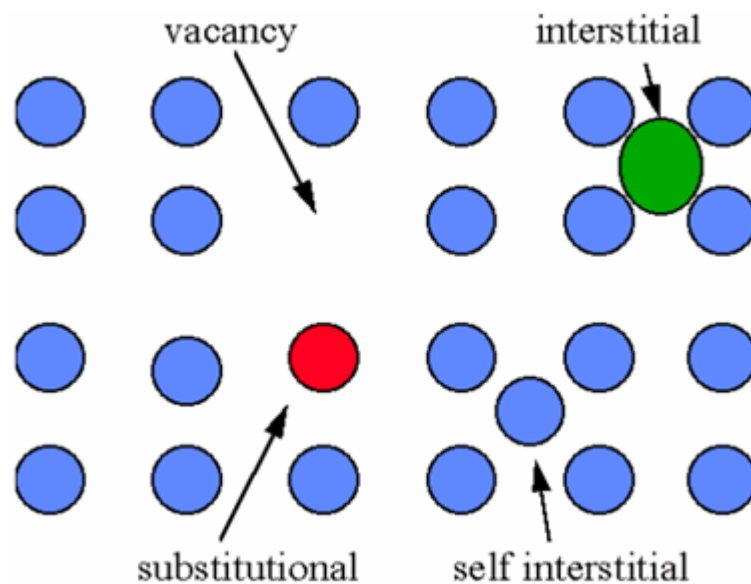


Fig. 4.3 Depiction of various point defects in crystalline structure

Vacancy defect, also known as Schottky defect, is a lack of an atom at a lattice site in an otherwise perfectly aligned crystal. This perfect alignment guarantees that the crystalline

structure will not collapse to fill the vacancy. Instead, a vacant spot might be filled by a nearby atom, which will create a vacancy at its previously occupied spot. Similarly to an electron hole, a vacancy can be treated as a quasi-particle and the movement of many separate atoms can be considered by an equivalent description of a vacancy moving in the opposite direction.

Another common type of point defects is an interstitial defect, defined as an atom occupying a lattice site which should stay vacant in a perfectly aligned crystalline structure. The site can be occupied by an atom foreign to the crystalline structure, as well as one of its own kind. In the latter case the defect is called a self-interstitial.

Analogically two cases can be distinguished if an atom of a wrong element is occupying a site that should be occupied in a perfectly aligned crystal. If such atom is foreign to the crystalline structure, the defect is called substitutional, or simply an impurity, since the source of the foreign atoms is due to the impureness of the material. However, if an atom occupying the wrong site belongs to the material, then it is an antisite defect. The properties of both those types of defects and a resulting deformation of the crystalline lattice depend on the size of the substituting atom. A significant difference of a radius from an original atom belonging to the lattice might cause a shift in an energy equilibrium position due to the weakening of the repulsive forces between the impurity ion and its nearest neighbors stabilizing the ion at the regular site in case of an substituting atoms that are over 10% smaller than the original [57], or in case of an atoms bigger than the regular ones, the displacement results from different covalency of the chemical bonds with the nearest neighbors [58].

Line defects, as the name implies, concern a part of lattice that forms a line. One example is an edge dislocation, when the plane of atoms terminate midway throughout the crystal. The surrounding planes bend to compensate for this sudden abrupton.

Planar defects concern a whole plane of atoms of the crystalline structure which interrupts the periodicity of the lattice. The most common example is an interface between two planes that exhibit different crystallographic direction. Another interesting example is a so called twin boundries defect, where the neighboring planes exhibit a symmetrical periodicity of the ordering of the atoms.

Occurrence of defects in semiconductor materials is a broadly studied topic [59-63]. Manufacturing a perfect crystal is a hopeless endeavor. Defect formation does cost energy from the system, however a certain amount of defects lowers the free energy in the equilibrium state due to the configurational entropy, and therefore will always be present. Unintentional impurities are also a part of this equation.

However to some degree the properties of the semiconductor can also be changed on demand, by introducing an intentional dopants into the crystalline structure. This goal can be achieved by various means. The most mature methods were developed for the silicon, as it is the most researched among the semiconductors. Doping methods can be classified in regard to the precision of the implementation. The base doping of the semiconductor is introduced at the stage of the growth, by adding the dopant material to the melt. This results in a fairly uniform doping of the whole bulk of the ingot. Further modification of the specific regions has to be performed with area selective methods. Traditionally it is achieved by diffusion of the dopant material placed in contact with the semiconductor, by the means of heating. The area that should not be doped is masked.

In this study a modern and vastly more precise method of ion implementation was used. The ion beam is concentrated in the area of interest and by controlling acceleration of the ions it is possible to achieve different effects, from etching to shallow doping of the sample. Ions are high-mass particles, compared with photons and electrons, and irradiation results in disintegration of the crystal lattice [64].

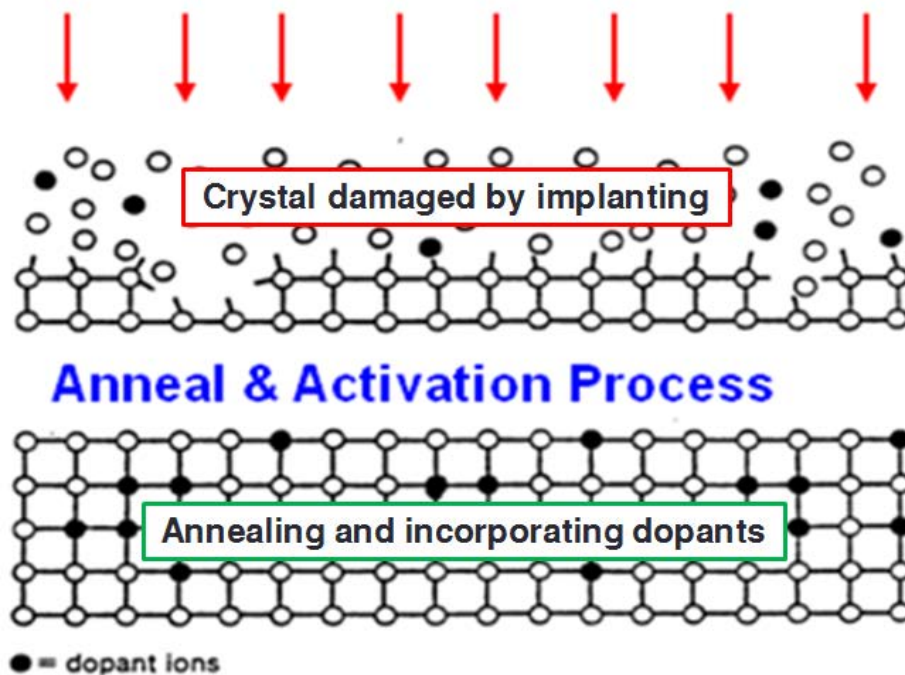


Fig. 4.4 Depiction of damage in the crystalline structure inflicted by ion beam and recovery by the annealing process.

This leads to deterioration of the semiconducting properties, including photoluminescence. To recover the crystal, it has to be annealed, which not only rebuilds the crystalline structure, but also incorporates the introduced dopants into the lattice and “activates” the expected properties. In performed studies a Focused Ion Beam (FIB) was used as a method of implementation of the Gallium ions. A schematic presentation of this process is shown in Fig 4.4.

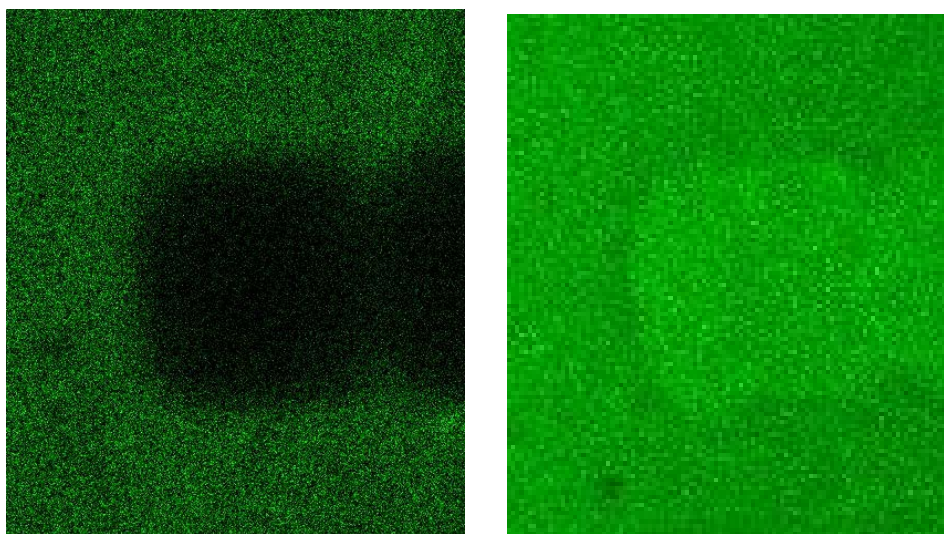


Fig. 4.5 Irradiated with FIB area of the ZnSe monocrystals (a) before and (b) after annealing.

The ZnSe was doped with gallium ion beam with acceleration voltage 15 kV and 2 mA current. Afterwards it was annealed in nitrogen for 1 hour at 500 °C. The result of this processing is presented in Fig. 4.5. As was predicted, the photoluminescence in the doped area recovered after the annealing process, and even exceeded that of the undoped area, due to the gallium ions acting as donors [65].

4.4. Native point defects in ZnO

In this chapter the energy levels of bands formed by native ZnO point defects and are presented. Additionally the possible transitions are analyzed. The purpose of this calculations is determination of the characteristic peaks in ZnO photoluminescence spectrum, in order to provide a precise filtration in the calculated range, introduced in chapter 6.2.

The presented values are derived from a number of first-principles calculations, basing on density function theory (DFT) and local density approximation (LDA). It has to be noted, that these are an estimation methods which produce significant discrepancies from the experimental data. For example band gap of ZnO calculated with LDA is only 0.8 eV, compared with experimentally obtained 3.4 eV [66]. Currently used correction methods are also not in full agreement [67-70], and therefore it is not always recommended to implement any other than the best known ones [71]. Especially, since even the experimental data, although ever-improving due to the increased availability of high quality ZnO monocrystals, still provides unsatisfactory precision and disagreement between different studies [72-75], and so an analysis of the impact of intrinsic single point defects is a significantly harder endeavor.

General approach to satisfactory estimation of the energy levels introduced with defects is by calculating the dependence of the defect induced transition levels with the corrected LDA method (LDA+U [76, 77]) based on the theoretical band gap calculation and extrapolating the results to the experimentally obtained band gap value [78, 79].

Several authors conducted a theoretical study in such defined formalism, in regard to all of the native point defect types introduced in chapter 4.2 in ZnO crystal [68, 71, 80], oxygen and zinc vacancies (V_o and V_{Zn}), antisites (O_{Zn} and Zn_o) and interstitials (O_i and Zn_i). The comparison of band gap calculation of a perfect four-atom crystal cell unit between LDA and LDA+U methods [71, 81], and experimental results [82] is presented in table 4.1.

Table 4.1 Comparison of calculated and experimental lattice parameters and band gap of ZnO perfect crystal lattice.

	<i>LDA</i>	<i>LDA+U</i>	<i>experimental</i>
<i>a</i> [Å]	3.195	3.148	3.253
<i>c</i> [Å]	5.160	5.075	5.213
<i>u</i>	0.379	0.379	0.381
<i>E_g</i> [eV]	0.80	1.51	3.44

As stated above, by implementing this theoretical values of a perfect lattice parameters to the calculations for native point defects, it is possible to estimate the introduced transition levels. For example removing a single oxygen atom from a perfect cell unit creates unattached bonds of the surrounding Zn atoms, which leads to creation of a state occupied by up to two electrons exhibiting mainly conduction-band character, as expected due to the formation from the bonds of a metal [71]. This defect acts as a donor, and is often attributed as a main source of intrinsic n-type conductivity of ZnO, since oxygen vacancy has the lowest energy of formation among donor-type native ZnO point defects. This results in the highest occurrence of oxygen vacancies, among donor-type defects, which is reflected in the highest intensity of the peak attributed to this defect in a photoluminescence spectrum of the sample studied in chapter 6.2. Corrected formation energy of oxygen vacancy, required to establish the levels introduced by this kind of defect can be calculated from the formula:

$$E^f = E^{f,LDA+U} + \frac{E_g^{exp} - E_g^{LDA+U}}{E_g^{LDA+U} - E_g^{LDA}} n \Delta \varepsilon \quad (4.1)$$

where $\Delta \varepsilon$ is a shift of transition levels between LDA and LDA+U approximation. Transition levels $\varepsilon(q,q')$ are defined as a Fermi level at which the formation energy of two neighboring charged states are equal. For example, from the depiction of the defect formation presented above, an oxygen vacancy can adopt three independent charge states, that is 2 electrons occupying the defect state and none in the excited state in the band gap ($q + 2, n=0$), 1 electron in each state ($q +, n=1$) or both bound electrons in the excited state ($q 0, n=2$). In this case the transition shift $\Delta \varepsilon$ can be calculated and compared at two intersections, between the ($q + 2, n=0$) and ($q +, n=1$) states, and between ($q +, n=1$) and ($q 0, n=2$). The results for this calculations for all types of native ZnO point defects obtained from literature position by *Janotti et al.* [71] and comparison with empirical data obtained by *Ahn et al.* [83] are presented in table 4.2.

Table 4.2 Theoretical absolute transition levels $\varepsilon(q,q')$, formation energies E^f and empirical data on transition levels of stable charged states q for all native point defects in ZnO.

Defect	q	$\varepsilon_t(q/q')$	E^f [eV]	$\varepsilon_e(q/q')$
V_O	2+	2.51	-0.60	0.90
	+	1.82	1.91	unstable
	0	NA	3.72	unstable
V_{Zn}	0	0.18	7.38	0.30
	-	0.87	7.55	unstable
	2-	NA	8.43	unstable
O_i	2+	-0.01	5.25	1.09
	+	0.00	5.24	unstable
	0	NA	5.24	unstable
Zn_i	2+	3.65	-0.45	3.14
	+	3.75	3.20	unstable
	0	NA	6.95	unstable
O_{Zn}	0	1.52	10.04	unstable
	-	1.77	10.88	unstable
	-2	NA	11.76	unstable
Zn_O	4+	1.88	-0.31	unstable
	3+	1.01	0.44	unstable
	2+	3.91	0.53	unstable
	+	3.97	2.74	unstable
	0	NA	4.98	unstable

It can be noticed, that the presented comparison of theoretical and empirical data produces significant discrepancies. Empirical data was deduced from crystal growth under changed environmental conditions. For example an increase in a green peak obtained from ZnO grown with sputtering in oxygen-less conditions were interpreted as an increased contribution of

oxygen vacancies. Since the study presented in this dissertation is purely empirical, all of the further divagations are based on this corresponding data. The presented discrepancies suggest that further investigation into correction methods of first-principles methods of energy level calculations are necessary.

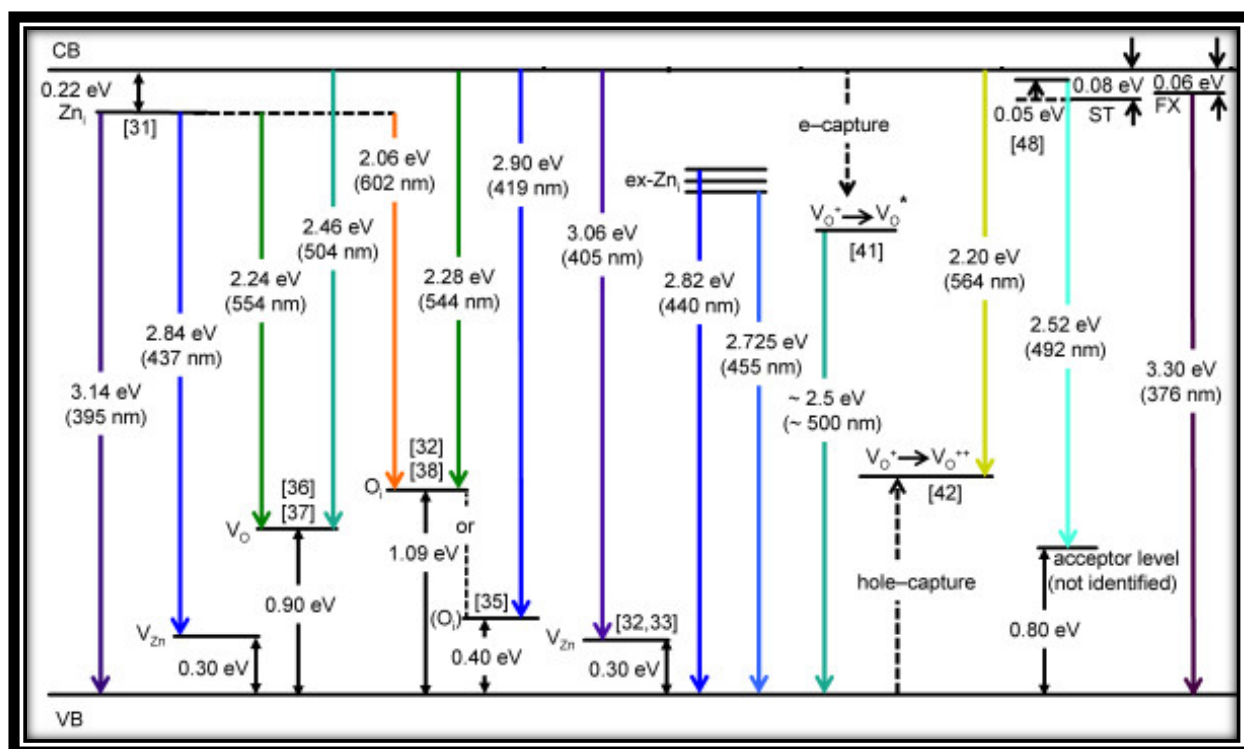


Fig. 4.6 Radiative transitions in ZnO due to the native crystalline structure point-defects.
Source: Vempati et al. [84]

The possible radiative transitions from such defined transition levels are presented on Fig. 4.6. It has to be noted, that the presented transition energies are further affected by the thermal and other effects discussed in chapter 3.2 and due to that, it is important to apply corrections to the best of our ability and experience when assigning experimentally observed peaks to the designated radiative centers. Further discussion of intrinsic ZnO defects observed in studied samples are presented in chapter 6.2.

5. Setup and software

5.1. Setup

The block diagram of the developed experimental setup is pictured in Fig. 5.1. Titanium doped sapphire (Ti:Sapp) laser in femtosecond configuration (Spectra-Physics Tsunami 3914V-Millenia, pulse width 80fs with adjustable wavelength) was used as a source of

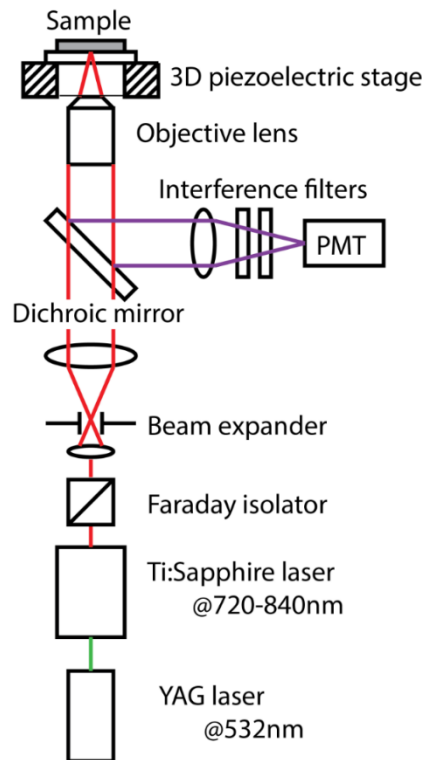


Fig. 5.1 Block diagram of the experimental setup

excitation light. The produced 5 mm diameter beam was extended twice by the use of beam expander (Thorlabs BE02-05-B) to achieve full coverage of the objective lens aperture. An extended beam was then focused inside the sample's volume with microscope objective (Olympus, NA 0.95). Light reflected by the specimen was filtered out with a dichroic mirror

and specifically selected filters for optimized attenuation of excitation beam. Photoluminescence light was collected with imaging lens into a photomultiplier tube (Hamamatsu Photonics K.K. H5784-01). Induced voltage was registered on a PC as arbitrary photoluminescence intensity and used to recreate image of the sample. Volume of interest was scanned with a three-dimensional translation stage (Physik Instrumente, P-563.3CD).

The probability of occurrence of the multi-photon process might be even a millionth part of the probability of a single-photon excitation in the same system. Thus, the requirement of a high photon density to ensure a detectable level of photoluminescence. CW lasers may provide high intensity output, but the photon flux is in general too sparsely distributed over time. Energy dissipation of the beam from the CW lasers that are capable of providing the required energy density would be very harmful to the sample and might lead to extreme photobleaching, photodarkening and ablation. Because of those reasons, mode-locked high power short pulsed lasers are used. The energy density during the pulse is high enough to excite a high number of fluorophores in the focal volume, yet the average energy output is much lower, which limits the damage to the sample.

Used in the developed setup Ti:Sapp laser source requires a supporting neodymium doped yttrium aluminum garnet (Nd:YAG) pump laser to initiate and support the lasing action. The titanium ions introduced by doping broaden the emission spectrum, and allow to adjust the output in a wide spectral range. Absorption and emission spectra of the Ti:Sapp crystal is presented on Fig. 5.2

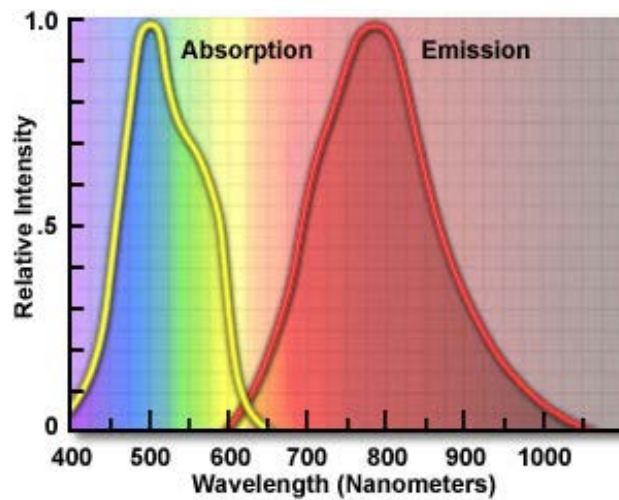


Fig. 5.2 Absorption and emission spectrum of the Ti:Sapp crystal. Source: www.microscopyu.com

Wavelength tuning is realized by a subsystem of prisms and a movable slit. Such system allows for a very narrow and efficient spectral filtration, with the output peak FWHM of 5-15 nm in the range of 720-850 nm. This laser incorporates mode-locking technique to generate spaced, short pulses of electromagnetic radiation. The Spectra Physics Tsunami laser is well known for its unique design incorporating a ten-mirror folded cavity. Since in such design the focusing mirrors are placed to work at angles other than normal incidence, the design requires a careful adjustment by utilizing Brewster-angle correcting rods and specified reflection angles to eliminate the optical aberrations that such design is prone for. Another feature characteristic for the used laser is an acousto-optic modulator that introduces an acoustic wave to control the phase difference between the longitudinal modes produced by the cavity and ensure the mode-locking ability regardless of the selected output wavelength.

Faraday insulator (Newport, ISO-05-800-BB) was used in the developed system, to guarantee that the parasitic light of the random phase generated in the imaging process have no path available to the laser cavity. Random phase reflections can break the mode-locking of the laser and hinder its ability to produce short pulses.

To ensure the maximum resolving capability, the microscopic objective lenses aperture has to be fully irradiated by the expanded light. The chosen beam expander (Thorlabs, BE02-05-B) provided an adjustable beam broadening.

The detection path was fully optimized to maximize the sensitivity of the system, since the two-photon emission is faint by itself, and spectral resolving additionally decreases the output signal. To achieve the highest technically possible detection rate, a photomultiplier tube was used as the output signal detector. The beam splitting was performed with the specifically selected dichroic mirror, to filter out the excitation light without affecting the intensity of the emitted light. Additional filtering of the remainder of the irradiation light was performed by the use of two short pass filters with the edge at 700 nm and 750 nm. This ensured over ten million times decrease in the reflected excitation signal, which introduces a negligible contribution to the total noise, and does not affect the measurements.

Spectral resolving was performed with carefully selected interference filters, which with its extremely steep edges and over 99 % transmission, is currently the most accurate technique of wavelength filtering. This advantage is critical to achieving required resolving abilities, and any inferior method, i.e. diffraction grating monochromators or color filters cannot provide the needed accuracy. The details of the used filters are provided in the further part of the thesis, together with the results of the performed spectral resolving.

Any outside and parasitic source of noise can easily suppress the measurement signal in such a sensitive system. To minimize such effects, a set of apertures and absorption screens was introduced to the system. Depending on the used sample it guaranteed the signal-to-noise ratio (SNR) of the two-photon signal up to 100 x, which is a satisfying result for a low output signal.

Scanning of the sample was realized with a closed-loop three-dimension nanopositioning stage by Physik Instrumente, model P-563.3CD. The stage uses piezoceramic actuators.. The stage provided resolution of 2 nm, which is beyond the resolving abilities of the optical system. To assure a repeatability with error 0.03 %, the stage uses integrated capacitive sensor providing a signal for an included servomechanism. The stage was directly controlled with a PI digital controller, model E-710. The intended position was supplied by the

LabView environment. The achieved speed of scanning with the described stage in a closed-loop operation is estimated at 75 points/s.

A picture of the developed system is presented on Fig. 5.3. The red envelope marks the Galilean beam expander. Blue envelope marks the dichroic mirror. Green envelope marks the PMT. Purple envelope marks the sample placement, replaced on the image by a mirror used for adjustment of the system. Brown line is aligned with the interference filters. Red line depicts the propagating beam.

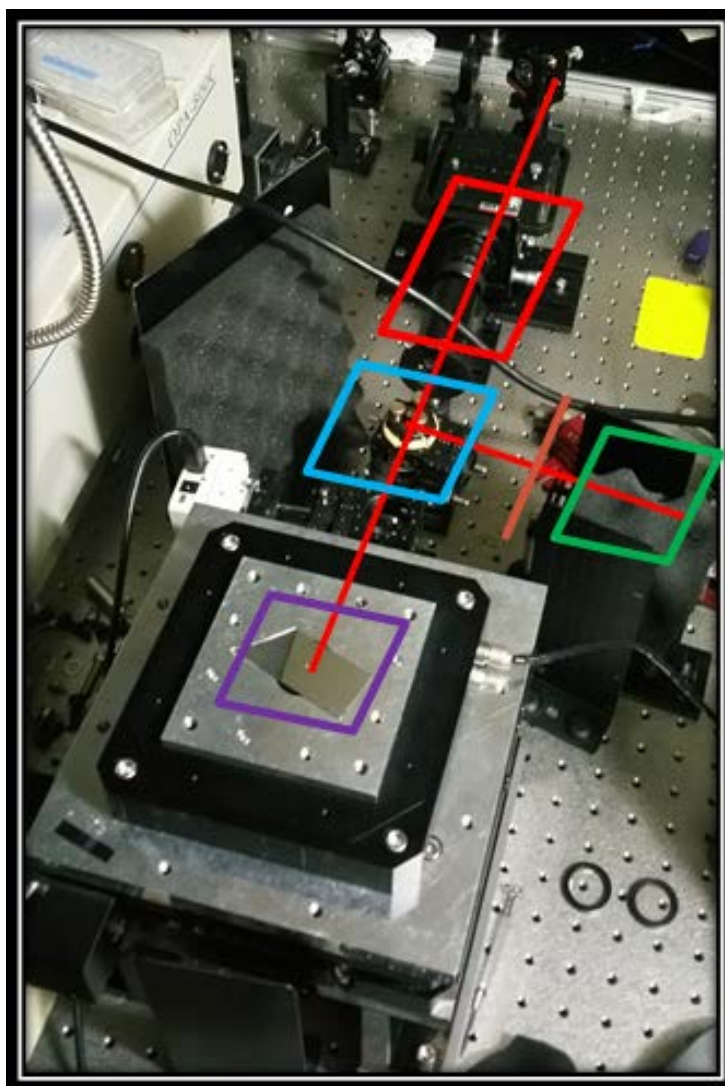


Fig. 5.3 Picture of the developed two-photon microscope system

5.2. Software

Controlling software was written in LabView environment by the author of the dissertation. Software was designed to ensure optimal efficiency and repeatability. Focus was placed on the use of the internal servosystem of the translation stage, maximizing the scanning speed and full control over the parameters of imaging. The user interface is presented in Fig 5.4.

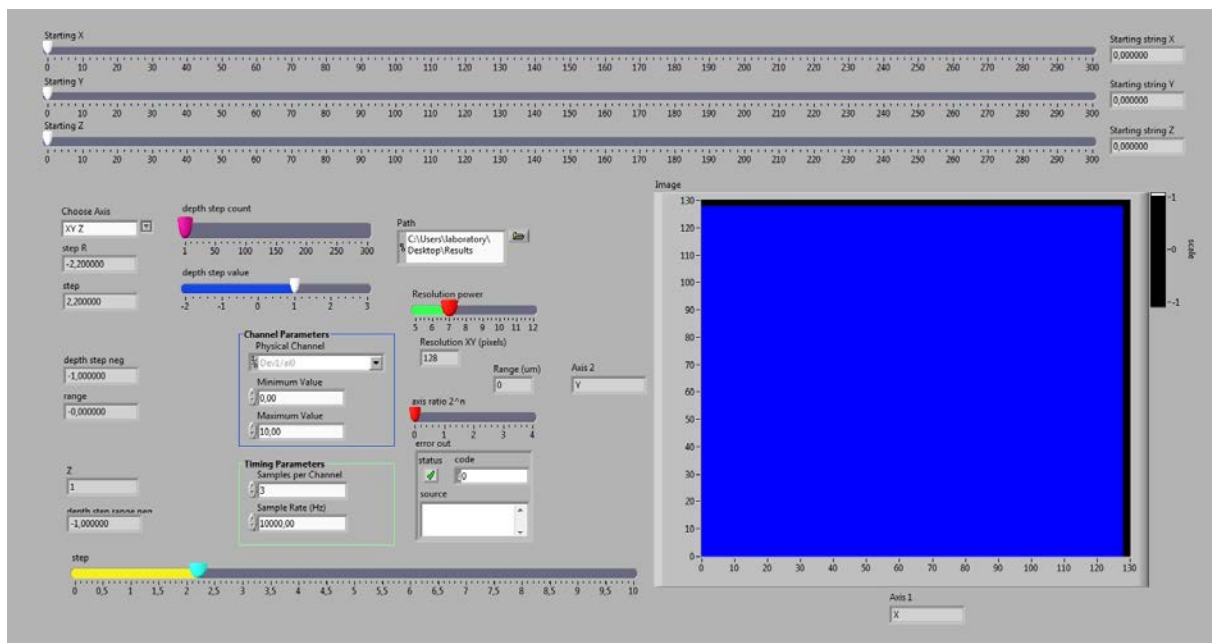


Fig. 5.4 User Interface of the developed LabView software

The choice of LabView environment was dictated by several factors. This environment provides an intrinsic control over the timing of the flow of execution, which is crucial for the synchronization of signal acquisition and positioning of the stage. Another important property is the easiness of control over inputs and outputs by automatic recognition of the

available devices, which removes the need to manually code the addresses and ports and provides flexibility of on-the-fly modifications of the system.

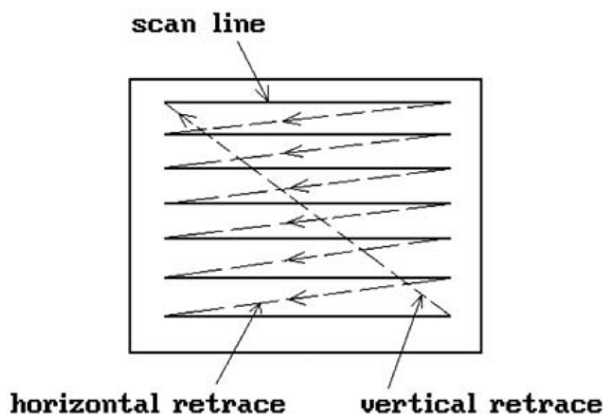


Fig. 5.5 Schematic representation of the scanning pattern utilized in the developed software.

Scanning was realized by the simple row-by-row manner shown on Fig. 5.5. The speed of scanning was tested in all possible directions for all the preprogrammed modes, and the fastest was implemented. Available modes are horizontal (X) – vertical (Y) with axial (Z) sectioning, XZ with Y sectioning and ZX with Y sectioning which allows for faster initial focusing of the system.

An amplified PMT signal was registered with integration time equal 100 μs . This value was selected basing on the maximum scanning speed of the translation stage, in order to preserve the speed of imaging.

User Interface provided control over the imaging parameters, including resolution, separate step size in all directions, starting position, integration time, averaging and image preview.

Proper alignment of the setup was confirmed with a series of measurements performed on fluorescent nanoparticles, to confirm the shape reproducibility, scale and spectral filtration. Results are presented in Fig. 5.6 and 5.7.

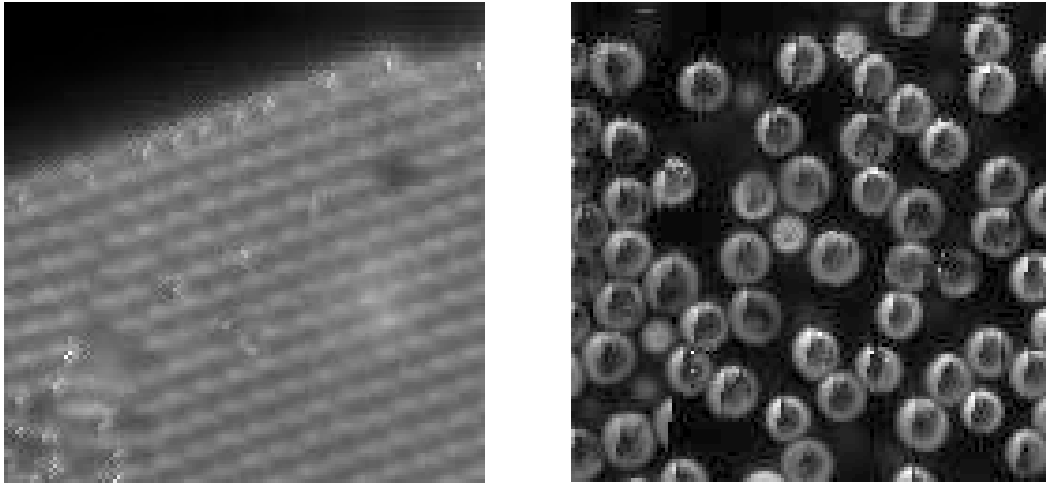


**Fig. 5.6 Two-photon image of fluorescent microparticles. Diameter: (a) $1\mu\text{m}$ (b) $5\mu\text{m}$
Resolution: 128×128 pixels. Size: $294 \times 294\mu\text{m}$**

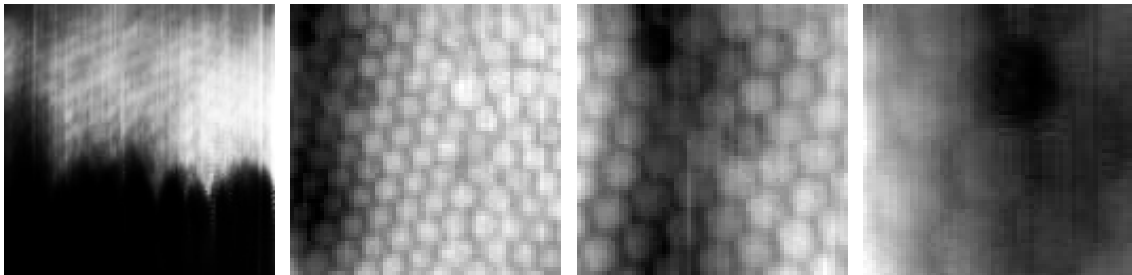


**Fig. 5.7 Two-photon image of blue fluorescent microparticles. Diameter: $2.1\mu\text{m}$
Resolution: 128×128 pixels. Size: (a) $51\mu\text{m}$, axial image (b) $19\mu\text{m}$, surface (a) $13\mu\text{m}$, surface (a) $6\mu\text{m}$, surface**

5.3. Frequent problems

During the measurements there are various parameters that have to be strictly observed to allow the imaging. The main concern is achieving and sustaining the energy density allowing for the two-photon process.

The ten-mirror folded cavity of the used laser source is very susceptible to the ambient temperature, due to the thermal effects affecting the geometry of laser and its elements, including mirrors and Kerr-lens. This might lead to breaking the mode-locking over time. To minimize this effect, the laser was used in an air-conditioned laboratory and before use was warmed up to achieve temperature equilibrium. Nevertheless, the breaking of mode-locking sporadically occurred, and laser operation required active supervision by the operator.

Focusing of the system proved to be problematic at times, depending on the class of the sample. Initial tries incorporated a CCD camera for visual assessment of the focus, however this method required splitting the measurement signal to provide part of it to the CCD camera. Additionally, low intensity of this signal affected the SNR, which lead to pure image quality and prevented effective focusing. The focusing method in the final measurements was based on digital readout of the two-photon photoluminescence (PL) intensity to find the initial focus inside the bulk of studied material. Precise focusing was performed by repetitive imaging of the XZ cross-section and adjusting the objective lens distance from the sample with the correction of a Z-axis positioning of the piezoceramic driven translation stage. This method proved to be very accurate and sufficiently fast.

The initial positioning of the sample had to be performed manually, since the range of movement of the positioning stage was only $300\text{ }\mu\text{m} \times 300\text{ }\mu\text{m}$. Depending on the performed measurements, the sample positioning could be arbitrary like in the case of homogeneous samples, or absolutely crucial like in the case of dopant imaging. Providing a coarse positioning system would lead to unnecessary increase of the size of the system, and the method at hand was deemed sufficient.

Overall geometry of the setup rendered it prone to the parasitic light and a lot of effort was put to maximize the SNR. The applied methods included fine geometry adjustment, isolation of the detector, strategic use of apertures and cutoff screens, and electrical grounding of all the electrically powered elements. All the measurements were performed in optically isolated laboratory.

5.4. Additional studies

To acquire a necessary characteristics of the used samples, a multitude of measurements was performed before the target two-photon imaging.

Nanoscale images of the surface were acquired with the Hitachi S-3000N Scanning Electron Microscope (SEM). The used filament material is Tungsten, and the accelerating voltage can be adjusted from 0.3 to 30 kV. This system allows for magnification in the range of 15 to 100 000x, with secondary electron resolution ranging from 3.5 nm to 50 nm, and backscatter electron resolution ranging from 5.5 nm to 100 nm, depending on the observed sample.

Fine processing and implementation of dopants was performed with JEOL JIB-4500 MultiBeam SEM-FIB (Focused Ion Beam) system, which allows to control the parameters of irradiation. Achievable resolution in the system is 5nm at the acceleration voltage of 30kV. Magnification adjustment is ranging from 100 to 300 000x. Ga liquid metal ion source with beam current adjustable from 0.1 nA to 30 nA is implemented. Default parameters (30kV, 2nA) resulted in etching of the sample. Decreasing the current and voltage of the treatment allowed doping the samples with gallium (Ga) molecules.

Nanoscale surface images of the semiconductors with especially wide band gap (3.5 eV+), which made them prone to charging under SEM radiation, were taken with the Atomic Force Microscope (AFM Keyence's VN-8010) in the tapping mode, to prevent the influence of an ambient humidity on the coarse surfaces.

To compare the developed method with methods available on the market, the samples were imaged with confocal (Leica TCS SP8) and phase-contrast (Olympus IX71) microscopes.

Absorption and emission spectra of the studied samples was measured with three different systems.

Absorption spectra was measured with V-670 UV-VIS-NIR Spectrophotometer by Jasco. Covered wavelength range extended from 190 nm to 2500 nm. In the UV-Vis range of interest, a grating with spatial frequency of 1200 grooves/mm was utilized.

Room temperature photoluminescence was measured with Jasco FP-8600 Fluorescence Spectrometer. The range of excitation wavelength from 200 nm to 850 nm. Photoluminescence detection in the range from 200 to 1010 nm. Scanning speed for excitation: 60,000 nm/min, for emission: 120,000 nm/min.

Low-temperature spectrum was obtained in a self-developed system utilizing a spectrometer and cryostat DSC600 by Linkam equipped with liquid nitrogen pump (LNP95) and system controller (T95). Such system is capable of controlling the samples temperature in the range from -196 °C to 600 °C with heating/cooling range from 0.1 °C/min to 100 °C/min. The light aperture diameter is 1.3 mm. To excite the sample, Nd:YAG laser working at fourth harmonic (266 nm) was used. The developed system is presented on Fig. 5.8.

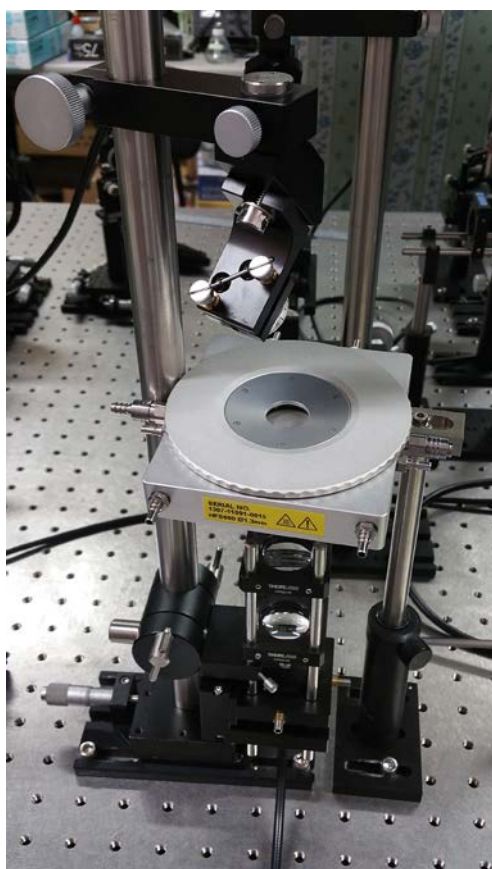


Fig. 5.8 Low-temperature photoluminescence spectrometer.

6. IMAGING OF NONUNIFORMITIES

6.1. Mechanical defects in ZnO monocrystal

To evaluate the two-photon system's depth of imaging we conducted initial measurements, which were focused on estimating the maximum depth of imaging of the mechanical defects in ZnO monocrystal. To ensure optimum conditions of excitation, the PL intensity dependence on the wavelength of excitation was compared for not processed and annealed ZnO monocrystal. The curves shown on Fig. 6.1 were obtained by analyzing a data obtained from spectrofluorometer.

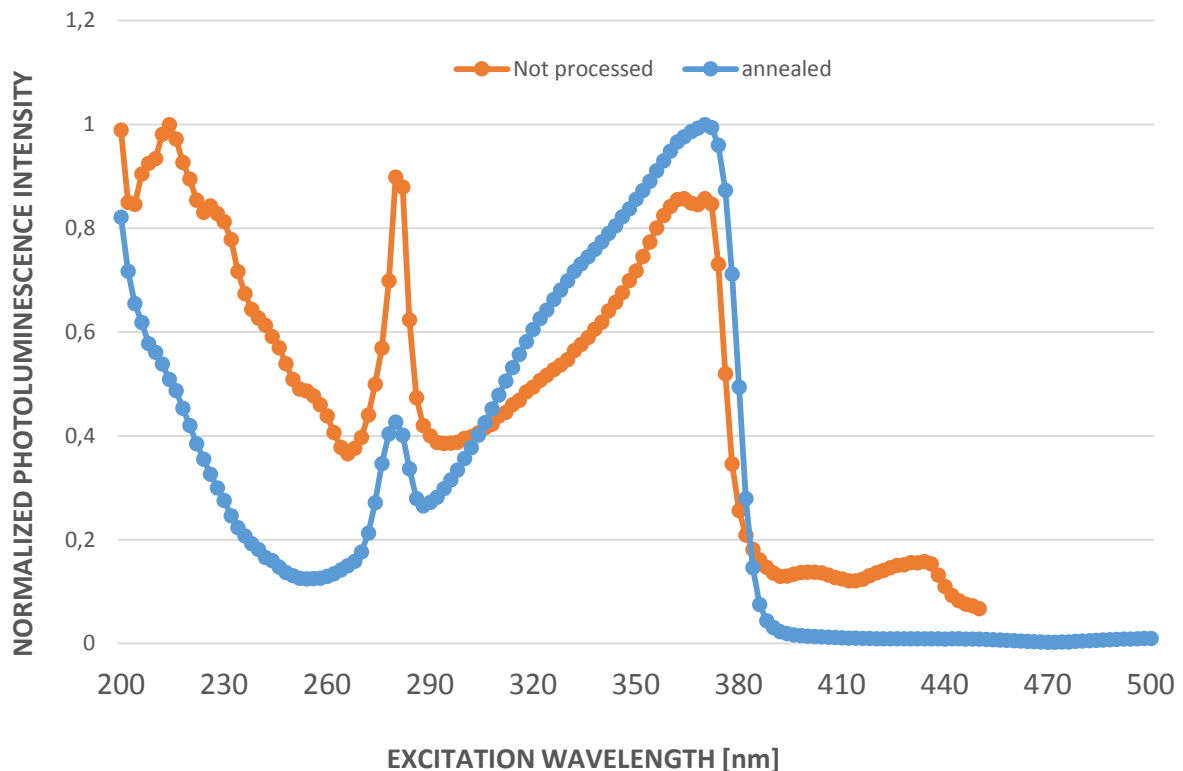


Fig. 6.1 Photoluminescence response dependence on the changing excitation wavelength

As can be seen, the most suitable wavelength to obtain high intensity emission from the ZnO monocrystal that was not subjected to annealing process under two-photon process is in range of 728 nm – 734 nm. The result of this imaging under excitation with 730 nm is shown in Fig. 6.2 and Fig. 6.3. Fig 6.2 shows two-photon imaged longitudinal section of ZnO monocrystal, where we can observe mechanical defects, in particular a microcrack propagating from the surface of the crystal as well as a fully internal defect - pore.

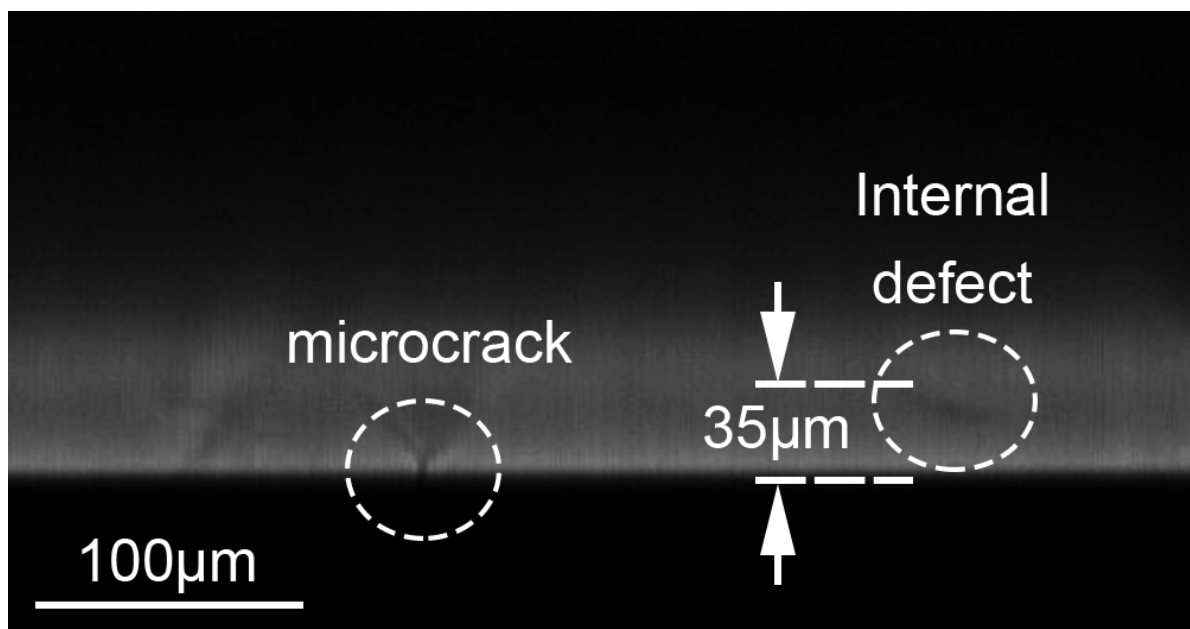


Fig. 6.2 Two-photon cross-section image of the ZnO monocrystals with marked mechanical defects.

For the microcrack the depth of the observed defect was 27 μm . Shape and propagation were also observable. The observed internal defect extends from 15 μm to 35 μm below the crystal's surface. These results allow us to estimate the depth limit of the imaging capabilities to be no less than 35 μm . Photoluminescence can be detected while focusing the irradiation light at up to 70 μm depth; however, due to scattering inside the crystal, in the current setup and with the measured sample, relevant information is obtained

only up to around half of this value, irrespectively of the given contrast of the image. Depth range also suffers from the loss of excitation light intensity with depth increase, due to spherical aberration, especially harmful in materials with high refractive index. Semiconductors generally fall into this group.

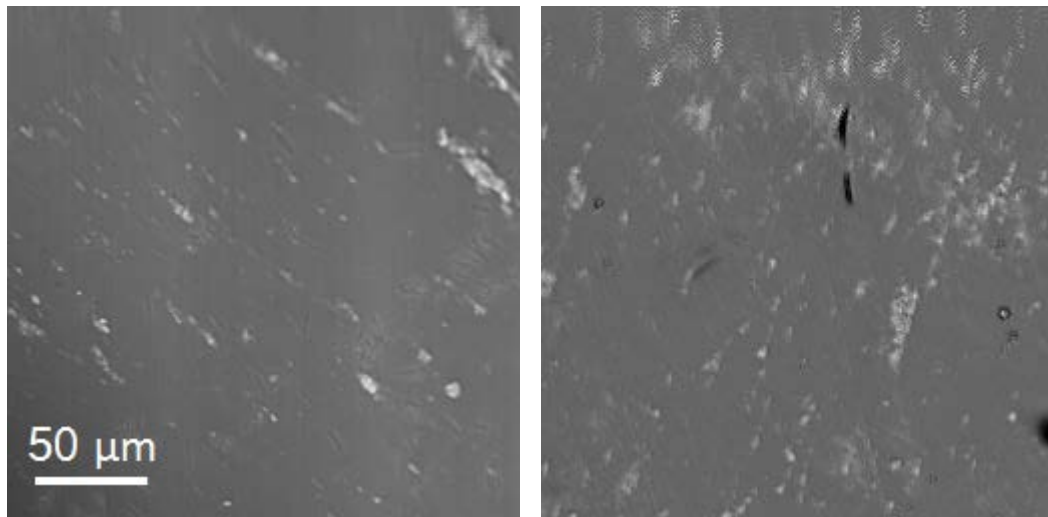


Fig. 6.3 Two-photon top-down image of the ZnO monocrystals surface.

Additionally due to the upconversional wavelength shift into the material's high absorption range, some of the emitted light gets reabsorbed inside the crystal [85], which attenuates the signal from deep regions even further.

Under the conditions of the conducted experiment, the theoretical lateral resolution is 310 nm. Axial resolution is deteriorated due to the spherical aberration in the semiconductor occurring due to the high refractive index and equals 1908 nm.

6.2. Point defects in ZnO nanorods

Different intrinsic defects exhibit characteristic transition energies, which can be used to distinguish the defects by filtering the photoluminescence spectrum in wavelengths range corresponding to the characteristic emission line of the defect. Repeating the measurement for the same area with the focus on various defects gives a full information on the amount and location of examined impurities in the semiconductor. For observation of the intrinsic defects we used ZnO nanorods as a specimen, since single crystals have a relatively content of intrinsic defects.

The ZnO nanorods were grown with a two-step process: firstly, a seed layer was formed by dip-coating a substrate in the solution of zinc acetate dehydrate ($\text{Zn}(\text{CH}_3\text{COO})_2 \cdot \text{H}_2\text{O}$, 99.0 %) and diethanolamine ($\text{HOCH}_2\text{CH}_2\text{NH}_2$, 99.0 %) and annealing it at 150 °C. Secondly, ZnO nanorods were grown with the hydrothermal method in the solution of zinc nitrate hexahydrate ($\text{Zn}(\text{NO}_3)_2$, 99.0 %) and hexamethylenetetramine (HMTA, ($\text{C}_6\text{H}_{12}\text{N}_4$, 99.0 %)). The length of nanorods obtained with this method is in the range of 2.5-3.5 μm and diameter is in the range of 0.3-0.5 μm . The process is schematically pictured in Fig. 6.4

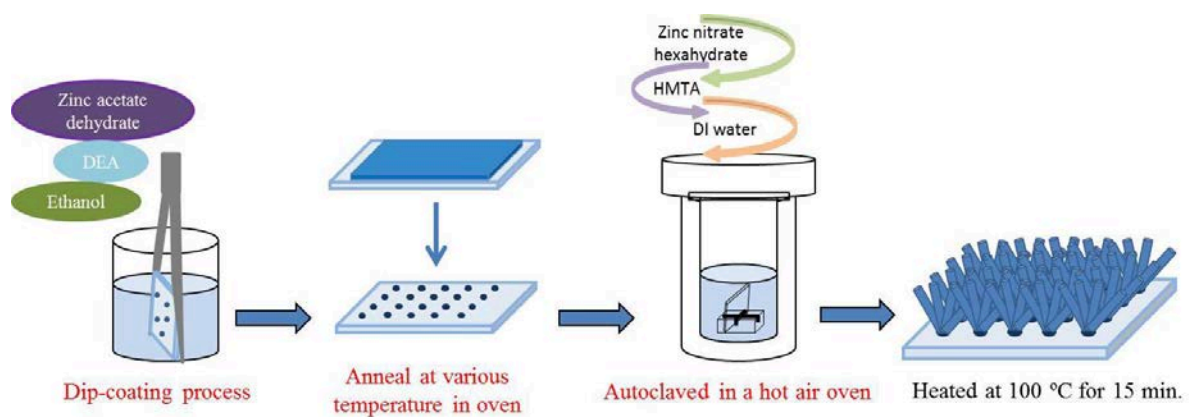


Fig. 6.4 The schematic representation of ZnO nanorods growing process.

The obtained nanorods are presented by SEM in Fig. 6.5. As can be noticed, the nanorods are randomly distributed, and did not align during the growing process. SEM image was taken in the area where the nanorods growth was dense. That increased the conductivity and allowed for SEM imaging

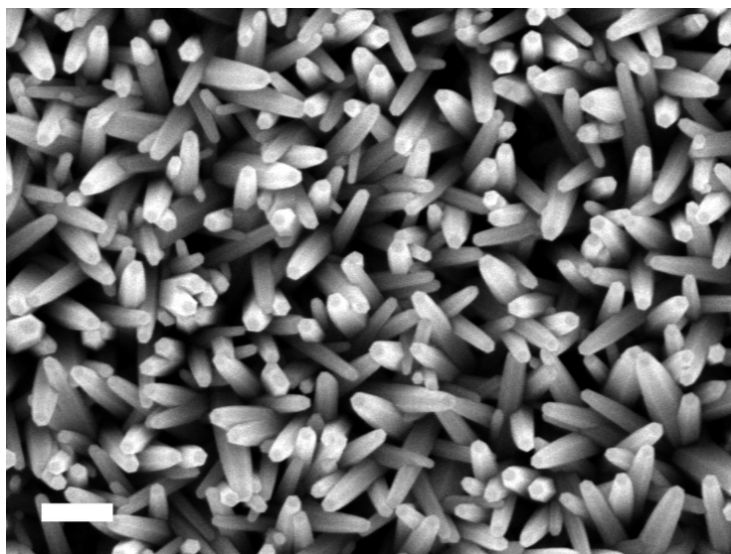


Fig. 6.5 SEM image of the ZnO nanorods sample. The nanorods did not align during the growth period. Scale bar: 1 μ m.

The area with scarce number of nanorods was prone to charging under the electron beam, and thus it was impossible to obtain a representative image of nanorods in this area. To overcome this obstacle, an image of this area was taken with DFM and is presented in Fig. 6.6



Fig. 6.6 DFM image of the ZnO nanorods sample. Picture width: 5 μm .

The roughness of the sample caused an artifacts on the image, as can be seen at the middle of the DFM image.

The fluorescence emission spectrum measured with a spectrofluorometer was used for the initial estimation of the defects content of the sample. All measurements were conducted at a room temperature.

The fluorescence emission spectrum, acquired by irradiation of the whole sample (10x10 mm), is shown on Fig. 6.7 and consists of 5 distinguishable peaks marked in the image.

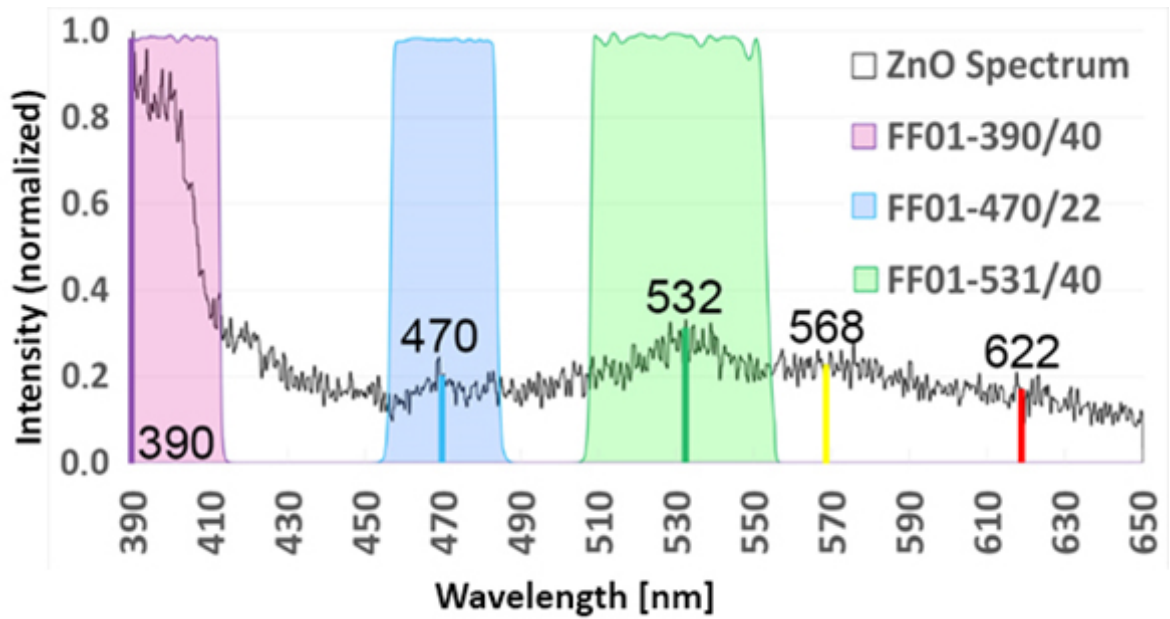


Fig. 6.7 Normalized fluorescence emission spectrum of ZnO nanorods sample excited @372nm with marked characteristic peaks and transition spectrum of the filters used for spectral measurements

The corresponding source of each peak was established in accordance with literature [83, 86]. The expected transition levels presented in chapter 4.3 had to be corrected by the redshift occurring in the room temperature by about 0.2-0.3 eV. Under this conditions, the highest peak at ~390 nm corresponds to the band gap E_g of undefected ZnO crystal lattice and, nearly indistinguishable, free excitons transition energy, which was treated collectively, since the free excitons of this energy also form in parts of the crystal structure without defects [87]. A peak at 470nm is commonly associated with zinc interstitials Zn_i . Both peaks at 531 nm and 568 nm are correlated with transitions from various bands to oxygen vacancy band V_o . Since both are correlated with the same type of defects, only the strongest one at 531 nm was considered. The peak at 622 nm is most likely due to the excess oxygen atoms at the surface of the crystal [88] and will be ignored in the further study due to insufficient intensity and the existence of alternative, higher resolution methods for observing the surface of the sample.

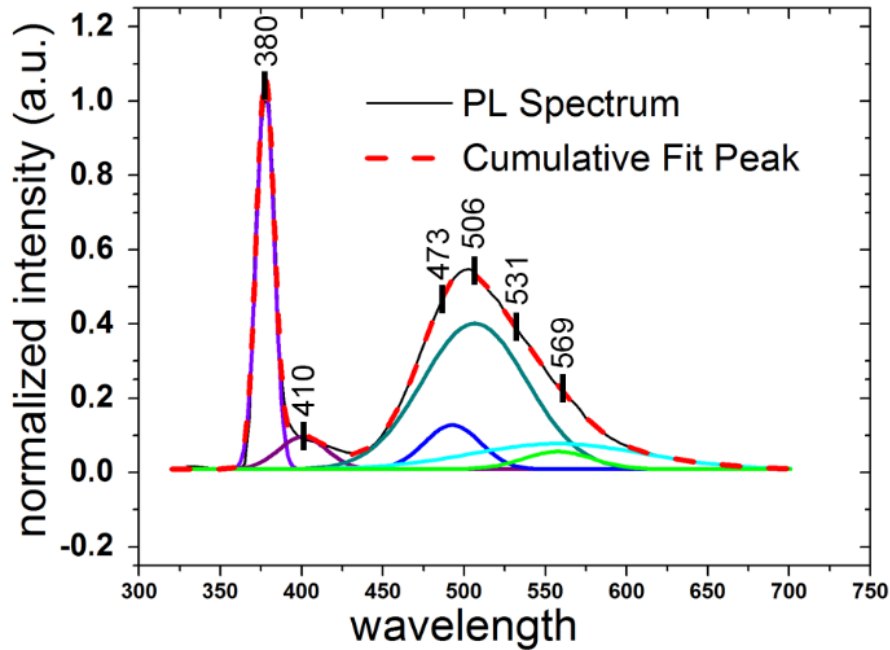


Fig. 6.8 Normalized photoluminescence spectrum of ZnO nanorods sample excited with Nd:Yag@266nm at 77 K.

For additional confirmation of the defects content in the total spectrum, we measured the low-temperature photoluminescence spectrum of the sample, which is presented in Fig. 6.8, together with the Gaussian analysis of the contribution of the peaks found with the second derivative analysis. The main peak shifted towards higher energy wavelength due to the widening of the band gap, as is expected in low-temperature measurements [89]. An additional peak at 410 nm that was not visible in room temperature is typically attributed to the exciton recombination between the holes in the valence band and the electrons localized at the Zn_i - shallow donor levels [86], and is not observable at the room temperature. Peak at 506 nm, indiscernible at the room temperature, became the prevalent source of green luminescence at 77 K. Exact contribution of this radiative center to the total spectrum at room temperature is not clear. Because of that, the main part of the peak is filtered out in the conducted measurements. Change of the proportions of the peaks can be attributed to the inhomogeneity of the sample and limited aperture of the used cryostat. Separation between the peaks of interest decreased in the low temperature conditions, however no additional

peaks in the imminent vicinity were detected, allowing to believe that at room temperature the overlap between the radiation spectra of the observed centers is separable.

The top-down image of the surface without spectral filtering is presented in Fig. 6.9.

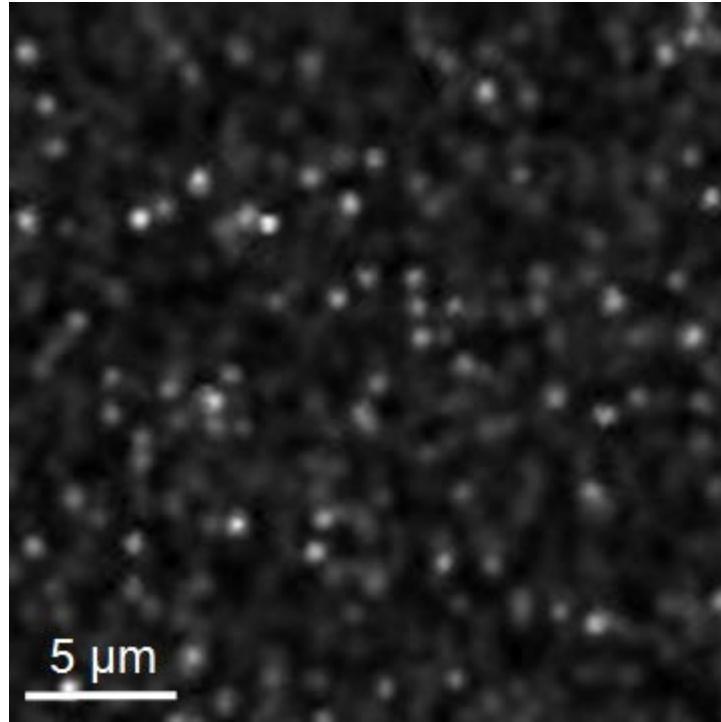


Fig. 6.9 Top-down two-photon image of the surface of ZnO nanorods sample.

The photoluminescence signal for the 3 peaks of concern was filtered with the use of interference filters (Semrock, FF01-390/40-25; FF01-470/22-25; FF01-531/40-25) whose transmission spectra are marked in the Fig. 6.7. Excitation wavelength was adjusted according to obtained spectral measurements, to maximize the fluorescence response for the wavelength of interest, since optimal energy of excitation depends on the type of defect. The Eg band gap was observed with the strongest intensity while exciting with 772 nm, O_{Zn} with 828 nm and Vo with 740 nm.

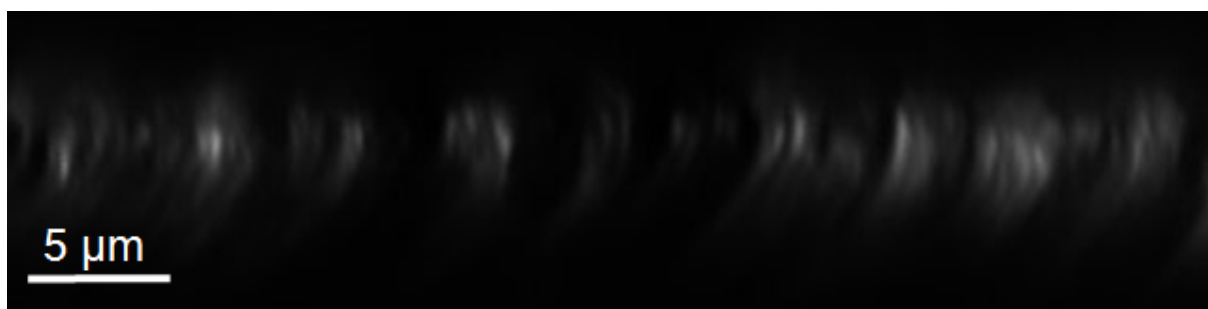


Fig. 6.10. Two-photon image of the XZ cross-section of the nanorods sample filtered at 390 nm. Image size: 16 μm x 64 μm

The image of the 390 nm peak (Fig. 6.10) was clear after single pass; however, the images of the remaining peaks had to be processed to improve the clarity. To achieve that, multiple images of the same plane were accumulated.

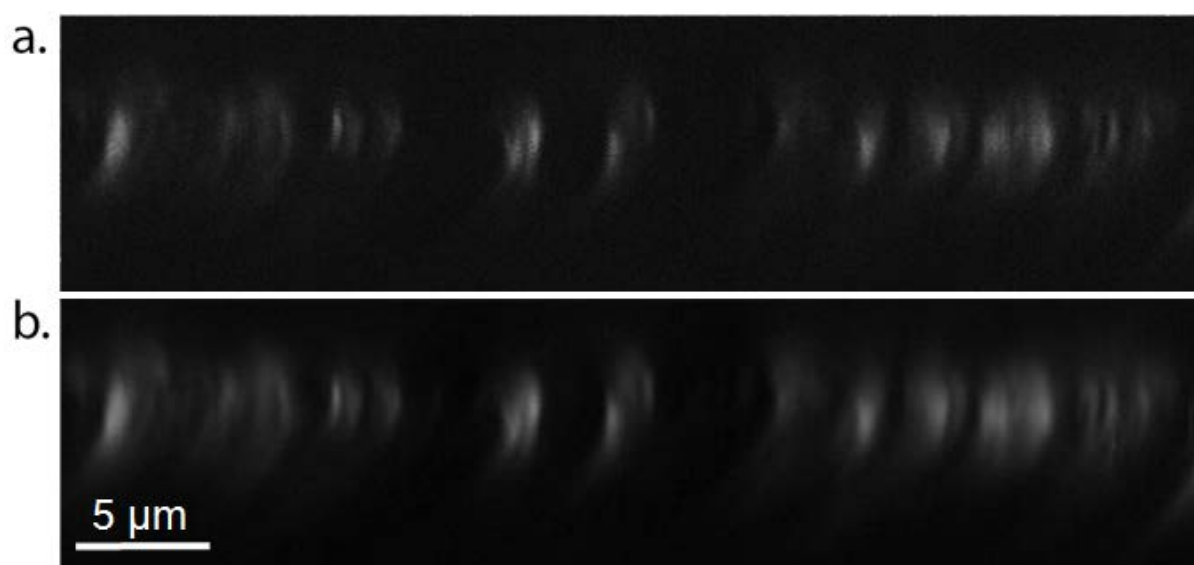


Fig. 6.11 Two-photon image of the XZ cross-section of the nanorods sample filtered at 531 nm. (a) single pass (b) result of accumulation of 10 images. Image size: 16 μm x 64 μm

The established number of accumulations sufficient to reduce the noise content without excessive blurring the image was 10 images for 531 nm peak (Fig. 6.11), and 40 accumulations for peak at 470nm (Fig 6.12).

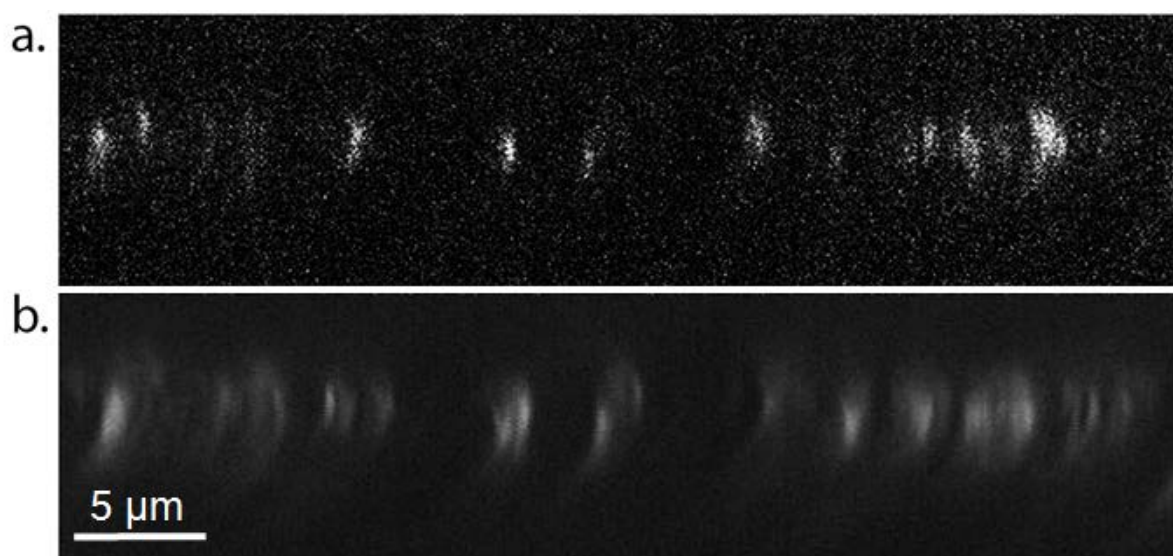


Fig. 6.12 Two-photon image of the XZ cross-section of the nanorods sample filtered at 470 nm. (a) single pass (b) result of accumulation of 40 images. Image size: 16 μm x 64 μm

Analysis of the obtained results is presented on Fig. 6.13. Fig. 6.13(d) shows intensity profile at the middle line of each image. Intensity was normalized and contrast was adjusted for the ease of comparison. High overlap of the obtained profiles are a further proof, that indeed the same region was imaged in all 3 figures. Vertical lines A,B,C,D and E mark the five largest discrepancies between the obtained images calculated as the difference between intensity in pixel number n of each profile, compared with the averaged local intensity of the remaining two profiles.

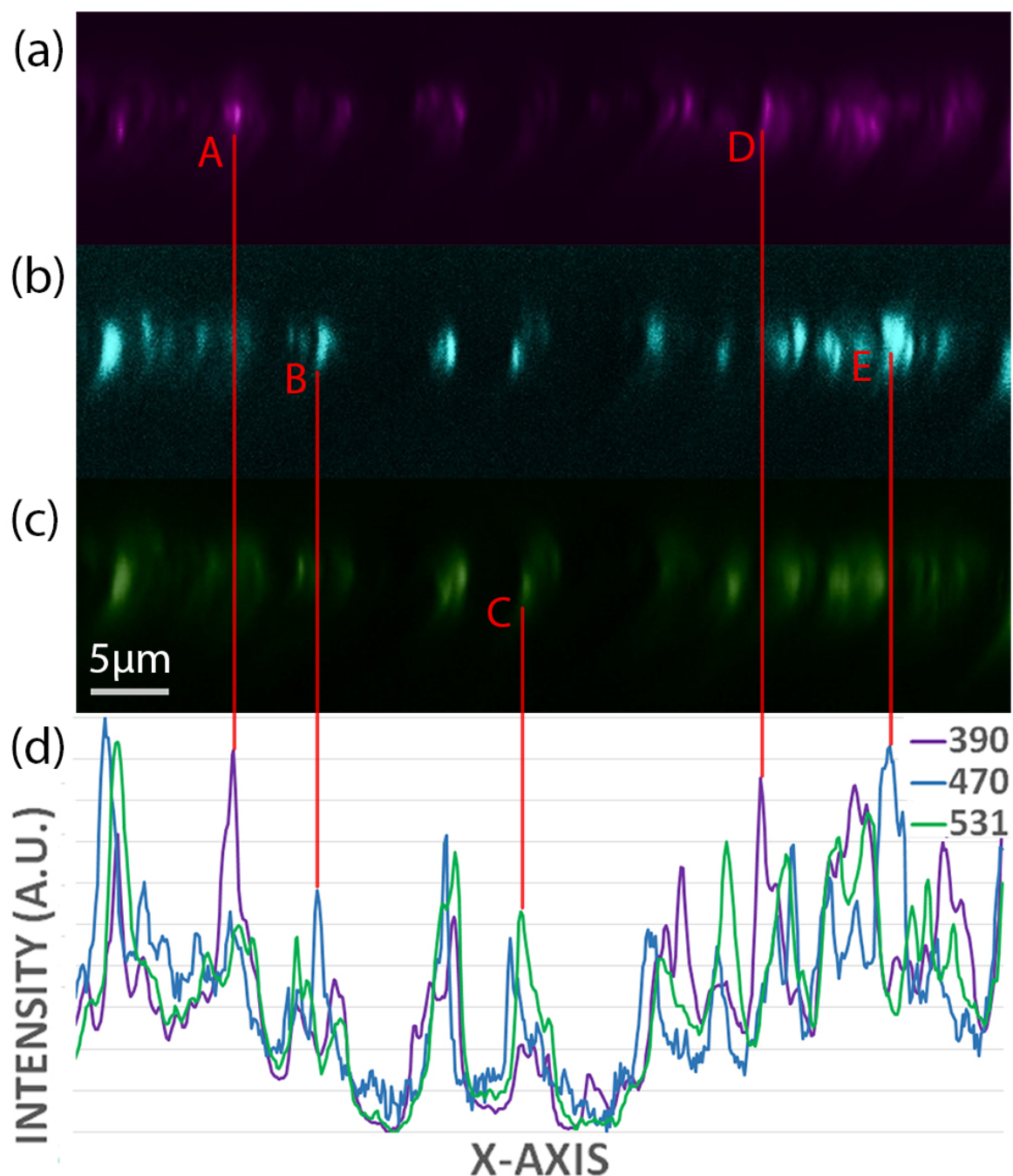


Fig. 6.13 Spectrally resolved two-photon fluorescence X-Z profile image of ZnO nanorods sample (a) Filtered for undefected ZnO (b) Image of zinc interstitials Zn_i obtained from averaging 40 single-pass images (c) Image of oxygen vacancies V_o obtained from averaging 10 single-pass images (d) Normalized and contrast adjusted profiles of images (d,e,f).

This approach allowed us to find the most and least defected regions of the sample. The least defected regions of the sample are marked with lines A and D, where the intensity for 390nm image is in proportion over 2 times higher than for the remaining wavelengths. Zinc interstitials Zn_i are the most common in the areas marked by lines B and D, while oxygen vacancies V_O are most concentrated in the region marked by line C.

The obtained results indicate that the developed method is well suited for the defect imaging in small ZnO samples and since the method is nondestructive, it can be used for tracking of the defects forming on various steps of processing during the manufacturing.

6.3. Effects of FIB etching on ZnO monocrystal

The ZnO sample in the form of single crystal was subjected to etching with the focused ion beam technique. The ion beam was formed under acceleration voltage of 30 kV, 2 nA current and the dose of 3 nC/ μm^2 . To evaluate the imaging abilities of the two-photon system various patterns, shown in Fig. 6.14 were etched into the sample. The dot patterns were etched in the 10 μm in 10 μm wide area. The size of the dots confined to such area at the regular pattern (top image) is 200 nm. Spacing is 800 nm. Fig. 6.15 shows an SEM image before processing and FIB image of the etched area.

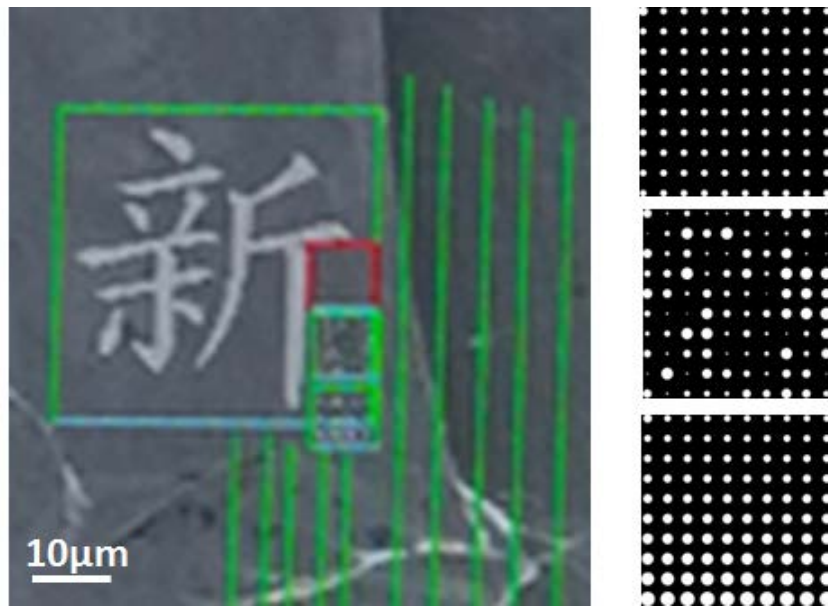


Fig. 6.14 Depiction of patterns etched with FIB on the surface of ZnSe monocrystal.

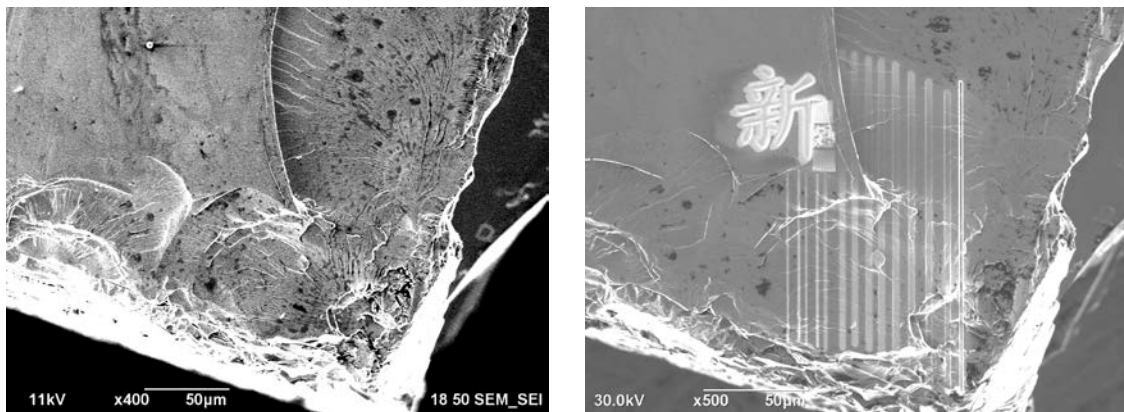


Fig. 6.15 Processed area of ZnSe monocrystal (a) before and (b) after etching.

The same area was imaged in the developed system, in a reflected light laser scanning configuration.

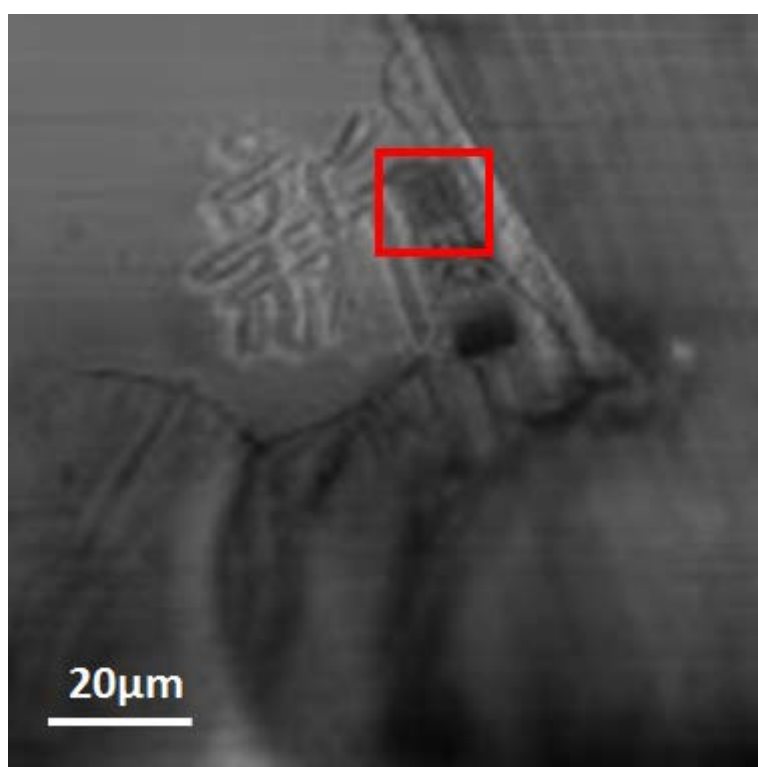


Fig. 6.16 Reflected light laser scanning image of the processed area. Red square marks the area etched with the top first dot pattern from Fig. 6.14.

The obtained image is presented in Fig. 6.16. The red square marks the area imaged under two-photon excitation conditions, presented on Fig. 6.17. The size of the marked area is 15 μm x 15 μm .

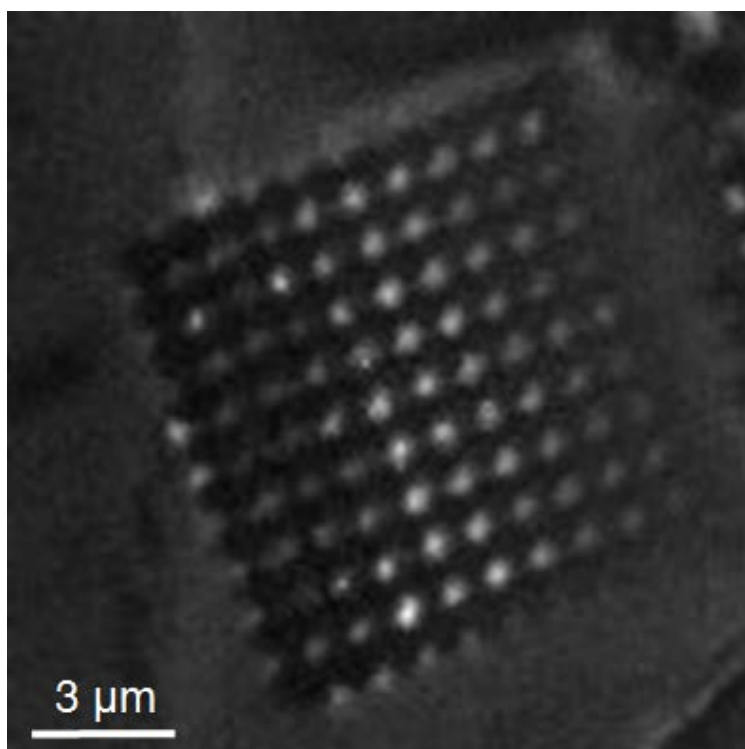


Fig. 6.17 Two-photon image of the marked area in Fig. 6.16.

A series of images distanced in the axial direction by 1 μm was obtained to illustrate the optical sectioning capabilities of the system. This image sequence is presented in Fig. 6.18.

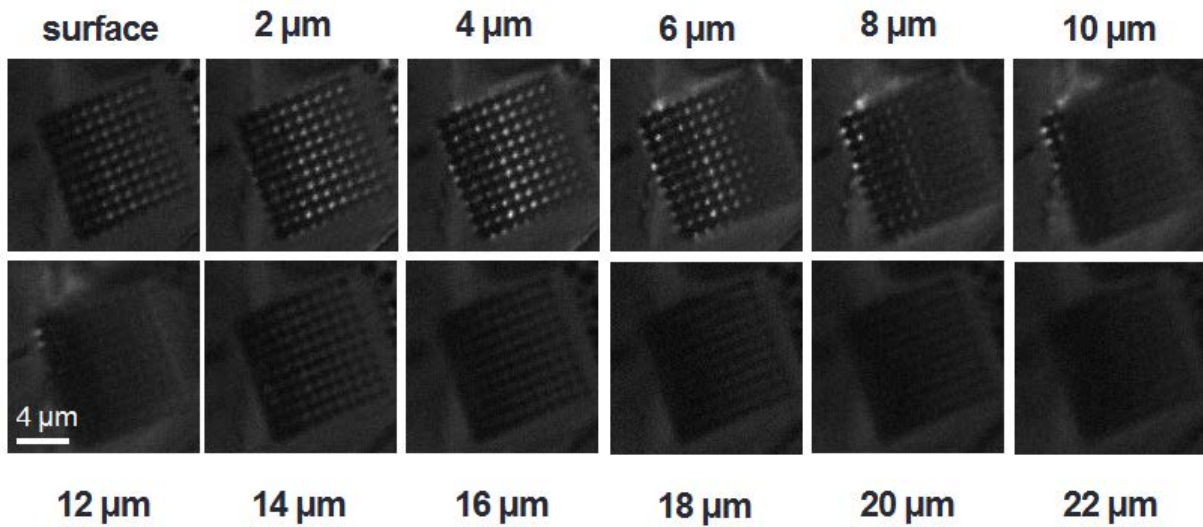


Fig. 6.18 Sequence of two-photon images along the axial direction. Spacing in axial direction = 2 μm

While the step of the piezoelectric stage was set to 1 μm as mentioned above, the distance between the imaged planes has to be calculated by multiplying the step size times the refractive index of the ZnO, which with good approximation is equal 2. Therefore the axial resolution of imaging is approximately 2 μm . As can be noticed by comparing this image with etching pattern in Fig. 6.14, the edges between the dots were not supposed to get etched. Lack of photoluminescence in this area indicates that the precision of the FIB system under set conditions was unsatisfactory and failed to produce the programmed pattern.

Two-photon system allows us to also observe the depth of processing, which cannot be observed under SEM or FIB imaging methods. As can be seen on Fig. 6.18, etching extends from the surface to 12 μm deep into the sample, and beyond. Exact depth of the etching was impossible to image, due to high fluctuation of the refractive index in this area resulting from the density of the etching pattern. Unpredictable changes of the refractive index in small volume of the sample result in additional blurring of the image. The depth of imaging can be increased by etching a simpler pattern under the same ion beam conditions, to establish the depth of processing. Similar study is presented in the next chapter.

6.4. Gallium doped ZnSe monocrystal

Another proposed application of two-photon fluorescence microscopy is dopant observation in wide band gap semiconductors. To evaluate the abilities of the developed system, the ZnSe monocrystals was studied. First step was measuring the ZnSe emission and absorption spectra (Fig. 6.19 and 6.20). Absorption edge maximum of the studied sample was at 405 nm.

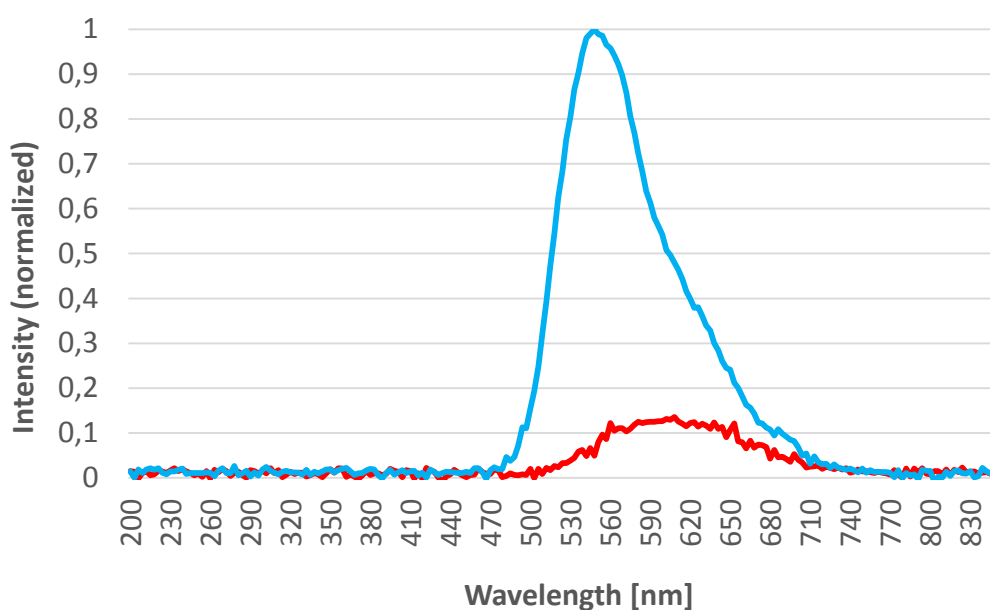


Fig. 6.19 Emission spectra of the ZnSe monocrystals taken at 300K (red line) and 77K (blue line)

As can be noticed from the emission spectrum, the intensity of emission at liquid nitrogen temperature increased almost six-fold. Substantial blue-shift was also observed. We can also notice that the single peak visible in room temperature consists of two overlapping peaks,

which can only be distinguished at the low-temperature spectrum. This second peak can be attributed to the donor-acceptor pair (DAP) recombination.

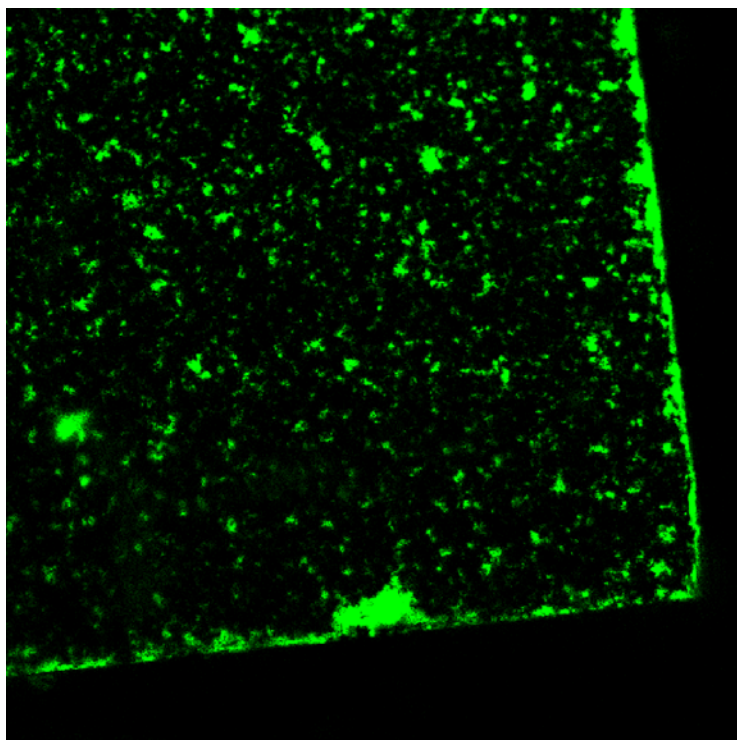


Fig. 6.20 Confocal fluorescence microscopy image of ZnSe monocrystals.

Before processing the sample, a confocal image was taken to confirm the quality of the surface under optical imaging conditions. The image is presented in Fig. 6.20 and as can be seen, the surface appears only slightly coarse. However there are no obvious defects in a wide area to prevent processing.

The sample was processed by the FIB to introduce Ga dopants into its volume. Various irradiation parameters, current varying from 0.1 to 1 nA and voltage equal 15 kV and 10 kV was tested to study the difference in the depth and nature of the doped area. Confocal image of the surface of processed crystal is shown on Fig. 6.21.

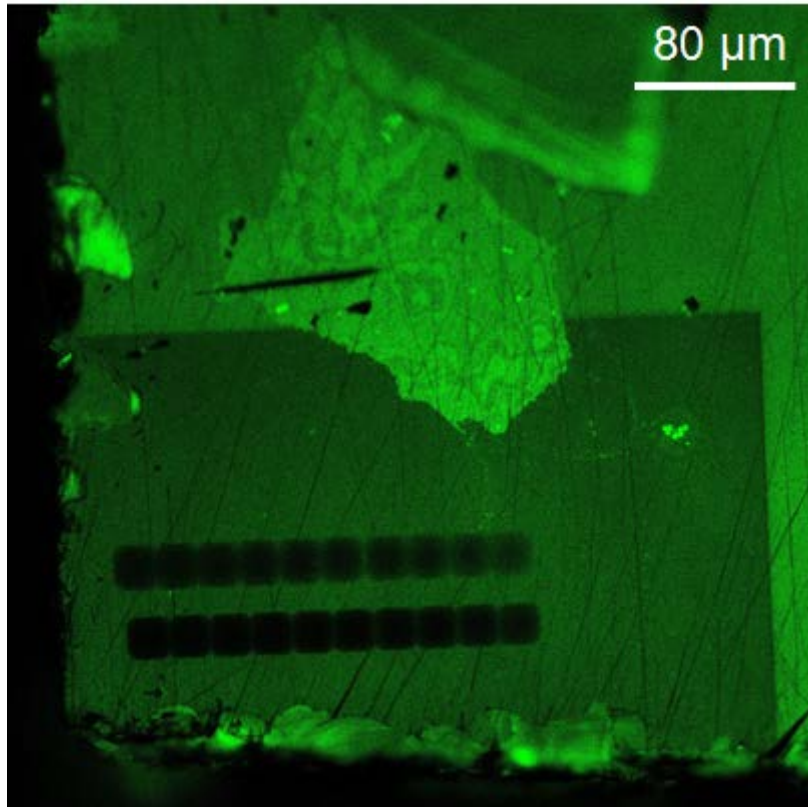


Fig. 6.21 Confocal fluorescence microscopy image of the processed Ga:ZnSe monocrystal.

Resolution: 4096 x 4096 pixels.

As can be noticed, not only the directly processed area is distinguishable on the confocal image, but also the square area that was affected by a very low current used for imaging. Close up of the processed area is shown on Fig. 6.22. Each sub-image is spaced in axial direction by 9.35 μm to present how the contrast and intensity changes with the increase of the depth.

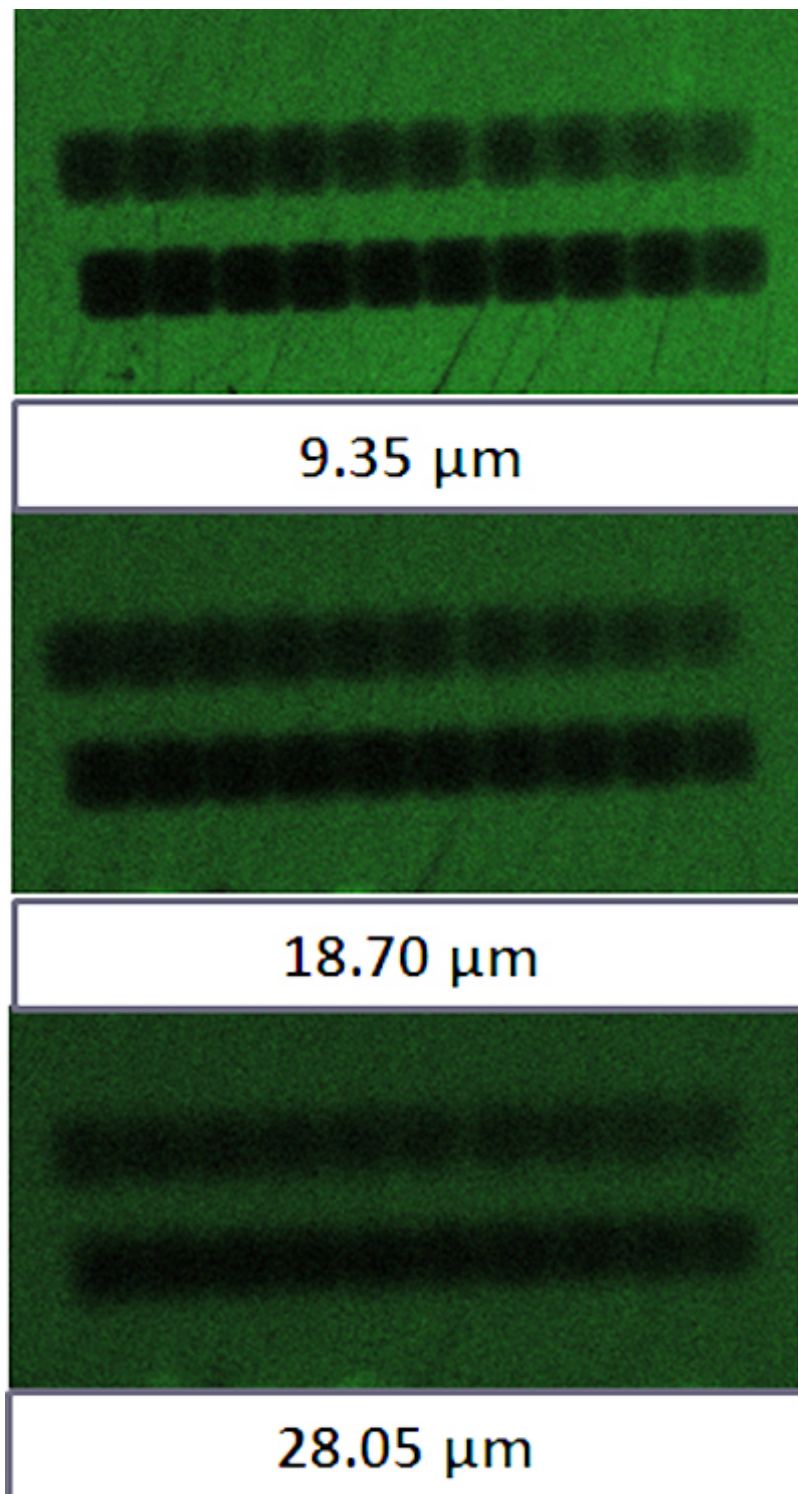


Fig. 6.22 Close up of confocal fluorescence microscopy image of the processed area of Ga:ZnSe monocrystal at various imaging depths.

As can be seen, the doping pattern is observable throughout the whole volume imaged with the confocal microscopy. Therefore this method has no ability to observe the depth of ionization.

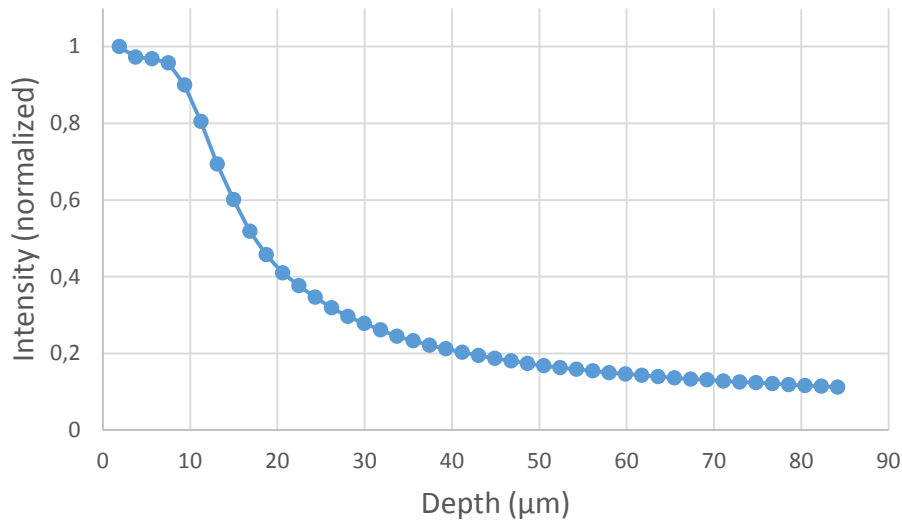


Fig. 6.23 The decrease of intensity of photoluminescence with the depth of imaging in ZnSe under irradiation with one-photon process.

The relative intensity decrease was calculated and is presented in Fig. 6.23. High intensity is preserved for 10 μm from the surface of the sample, but beyond that point a steep decline is observed, due to the excitation light absorption in the shallow part of the sample.

As presented in chapter 4.2, the ion implementation process leads to disintegration of the crystal lattice. The doped ZnSe crystalline structure was recovered by annealing in gaseous nitrogen flow to prevent the oxidation, for 1 hour at 500 °C. A side by side comparison of confocal images before and after annealing is shown in Fig. 6.24.

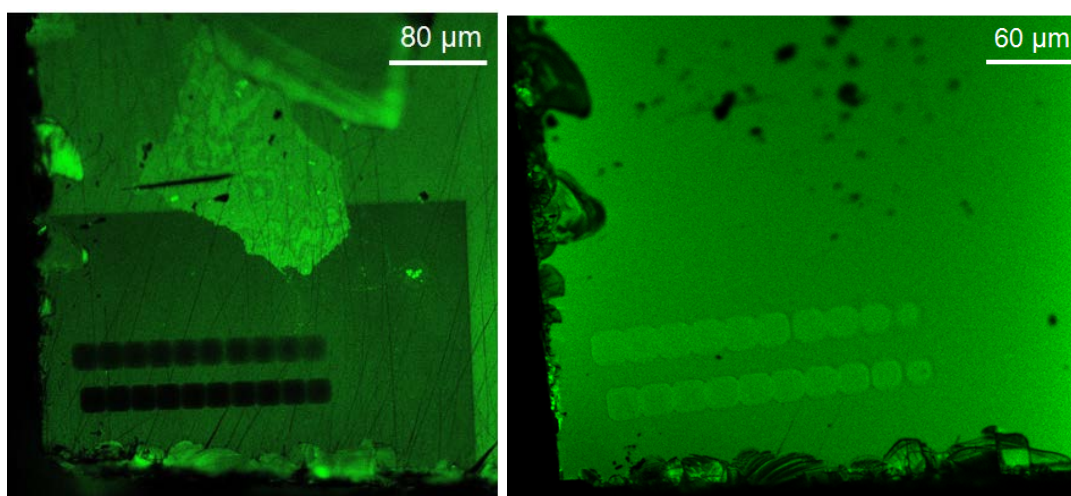


Fig. 6.24 Processed surface of ZnSe monocrystal (a) before and (b) after annealing in nitrogen for 1 h at 500 °C.

The doped area recovered, and the photoluminescence additionally increased, compared to the undoped area, as explained in chapter 4.2. Furthermore, it can be noticed that the area irradiated with low-energy gallium ions during imaging in FIB system, that previously formed a characteristic rectangular area around the processed part, completely disappeared after annealing. This is due to the diffusion of dopants throughout the volume of the sample. Moreover, regarding the scratches and mechanical defects, an overall quality of the surface increased.

Strong photoluminescence of ZnSe indicates that the material is easily excited, which raises concerns about the achievable resolution of imaging. Annealing increased this unexpected problem even further. As explained in chapter 2.4, the lateral and axial resolution is confined in the focal volume, however exact size of the excitation volume depends on the energy density and density of the fluorophores. If both values are high, the threshold for the two-photon excitation is met at a wider part of the beam diameter, and excited volume extends. This effect has to be studied individually for each sample of material that exhibits high photoluminescence.

To evaluate the axial resolving abilities, the cross-section image of the sample was acquired under various irradiation power. The exemplary images are shown in Fig. 6.25.

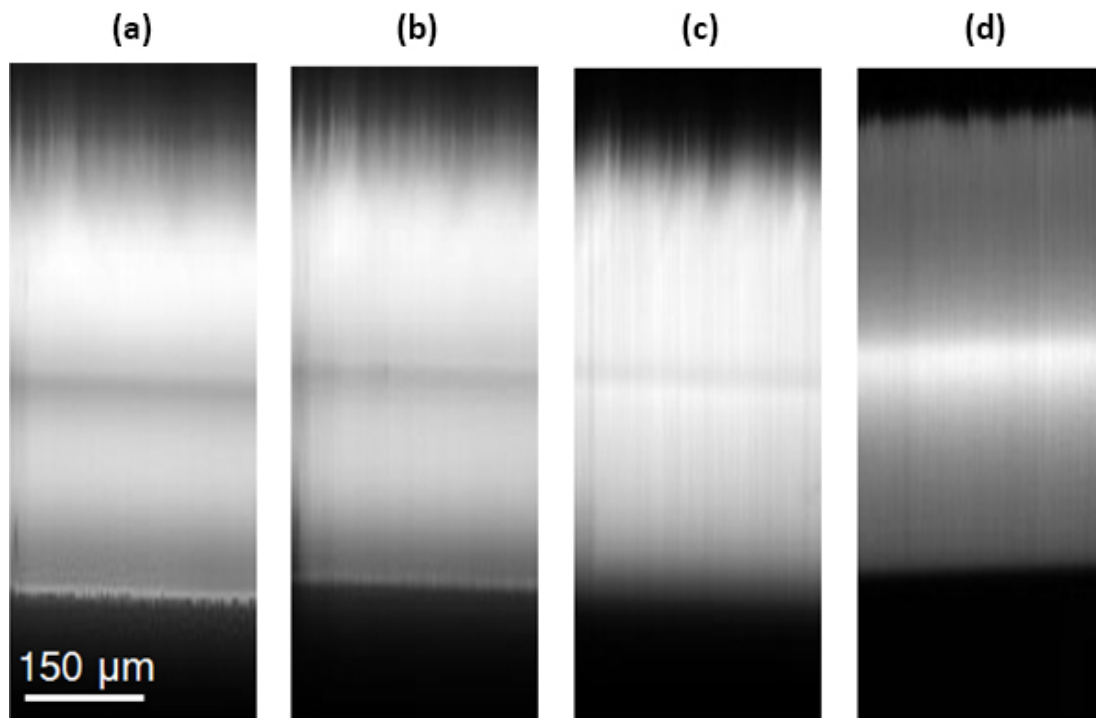


Fig. 6.25 Cross-section two-photon image of the ZnSe monocrystal under varying irradiation power. (a) 242 mW (b) 100 mW (c) 10 mW (d) 2 mW.

From the presented images it can be noticed, that the photoluminescence was detectable throughout the whole volume of the 0.5 mm thick crystal. The vertical lines, which are more pronounced with the decreasing power, are aligned with the scanning direction, and are a result of laser power fluctuation. While the nominal value of fluctuations of the used laser source is <1%, the significance of this fluctuations increases with the decreasing SNR.

It can also be noticed, that the surface of the crystal from the irradiation side is imaged much more smoothly, than at the opposite side. This surface was imaged with a comb-like shape. However the periodicity of the thicker and thinner regions does not correspond to the pixel size. Furthermore, the pattern repeats itself on all of the images, regardless of the irradiation power. And because the semiconductor sample did not exhibit such roughness of any of the surfaces, the image is a result of the refractive index inhomogeneity throughout the sample. Higher local refractive index produces an image that appears to be extending

deeper, than the one obtained from lower local refractive index, despite lack of the actual difference in the thickness of the sample. Additionally, the refractive index fluctuation occurs on a wider area than the imaging resolution. This might be used as an additional insight into the distribution of the defects in the bulk of the semiconductor.

On the image obtained under the highest irradiation power it can be noticed, that the surface appears significantly brighter than the volume directly below it. The effect is reduced with the decreasing power of irradiation. This effect indicates that the surface is strongly excited even when the irradiation beam is focused on a different plane. Such effect leads to obscuration of the image of in-focus plane, by the out-of-focus surface image and should be avoided.

To quantitatively compare the fidelity of imaging, the acquired averaged profiles of the cross-section scans were compared by the statistical analysis of the sharpness of the edge. The obtained profiles are presented in Fig. 6.25. The intensity was normalized, however the source images were not contrast enhanced, in order to reproduce an impact of the increased noise. In an attempt to increase graph's clarity the profiles were spread horizontally, and the number of pixels on the horizontal axis does not represent an absolute depth into the sample.

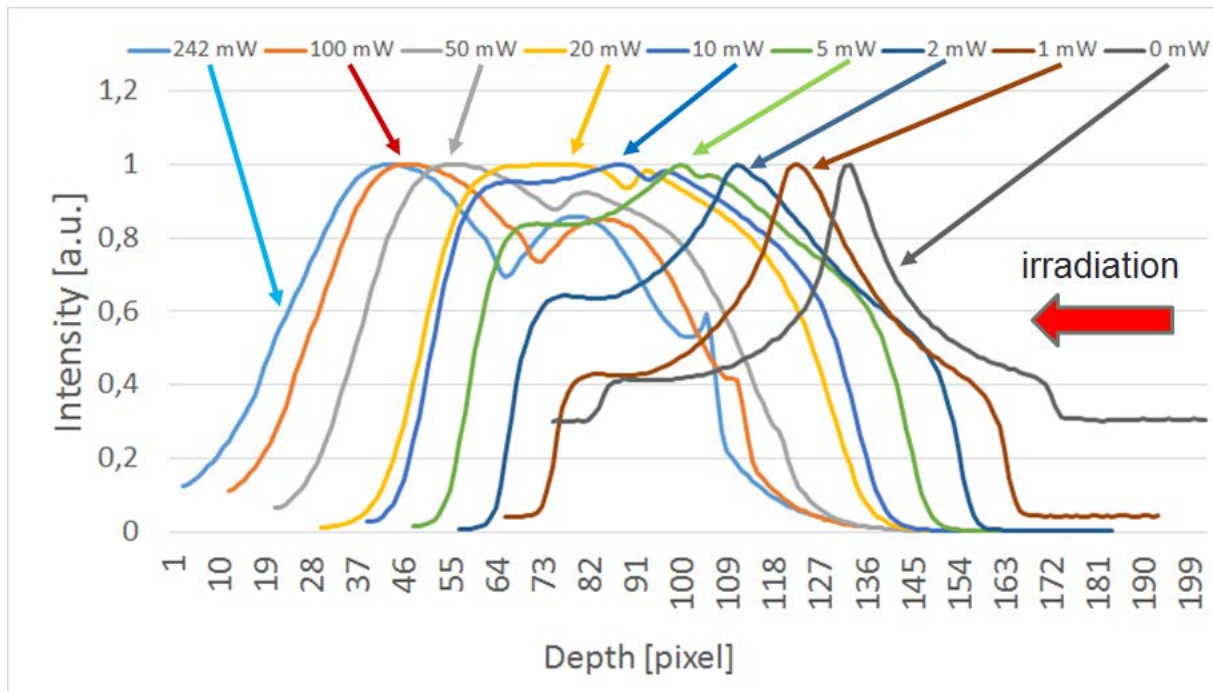


Fig. 6.26 Normalized intensity profiles of cross-section two-photon images taken under various (marked on the figure) irradiation powers.

The width of the edge was analyzed at both of the surfaces, for comparison. The analysis consisted of derivation of the linear equation of a tangent of both edges at each of the 128 horizontal pixels. Accumulated data was used to reproduce the edge fidelity and its spread. Obtained results are presented in Fig. 6.27 and Fig. 6.28.

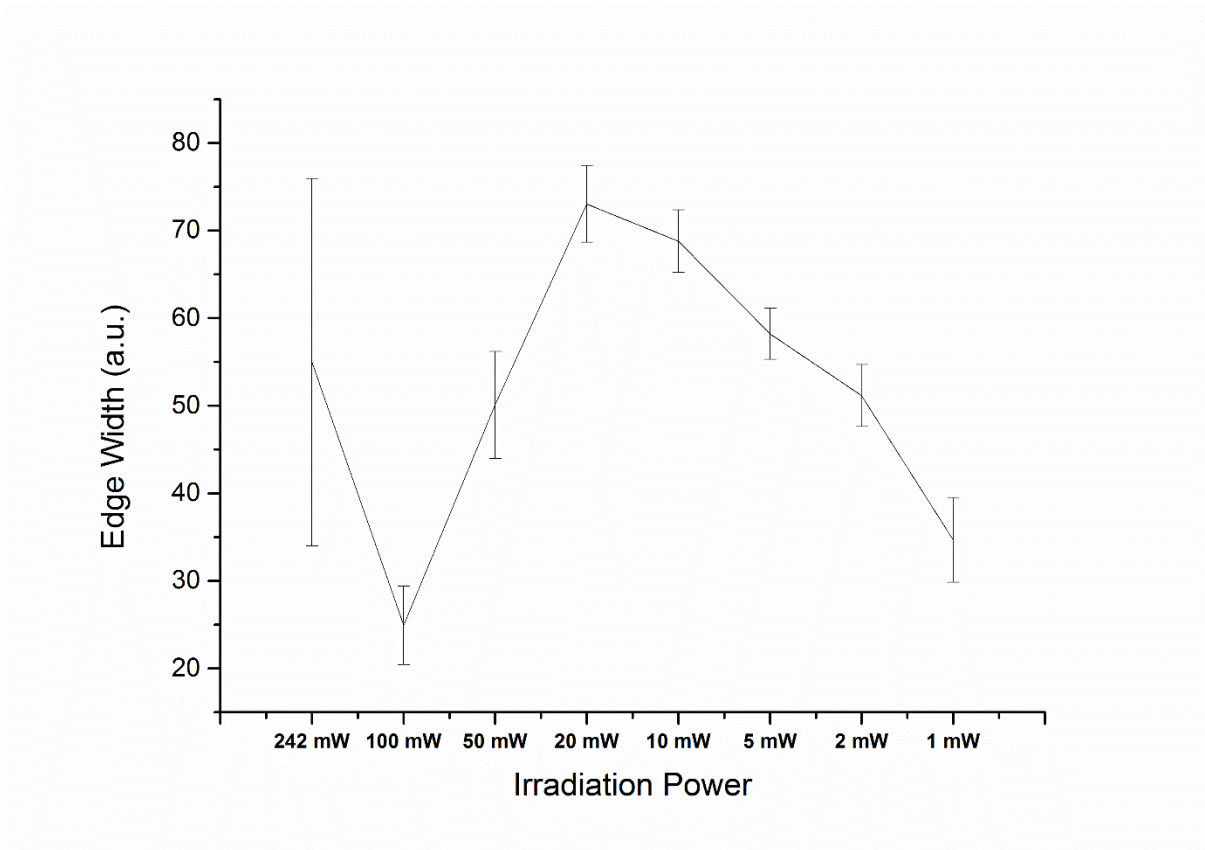


Fig. 6.27 Edge fidelity under varying irradiation power at the surface from the irradiation direction.

An analysis of the surface from the irradiation side shows, that the edge fidelity increases if the power of the excitation beam is attenuated to 100 mW. Below this value the fidelity degenerates due to the decrease of SNR and overall decrease of the signal. A high spread of the value at 242 mW irradiation power is a result of an optical sectioning failure, described in previous chapters. At such high power, with the given high photoluminescence response characteristic to the material, an excited area extends beyond the Airy disc. The sample is overexposed.

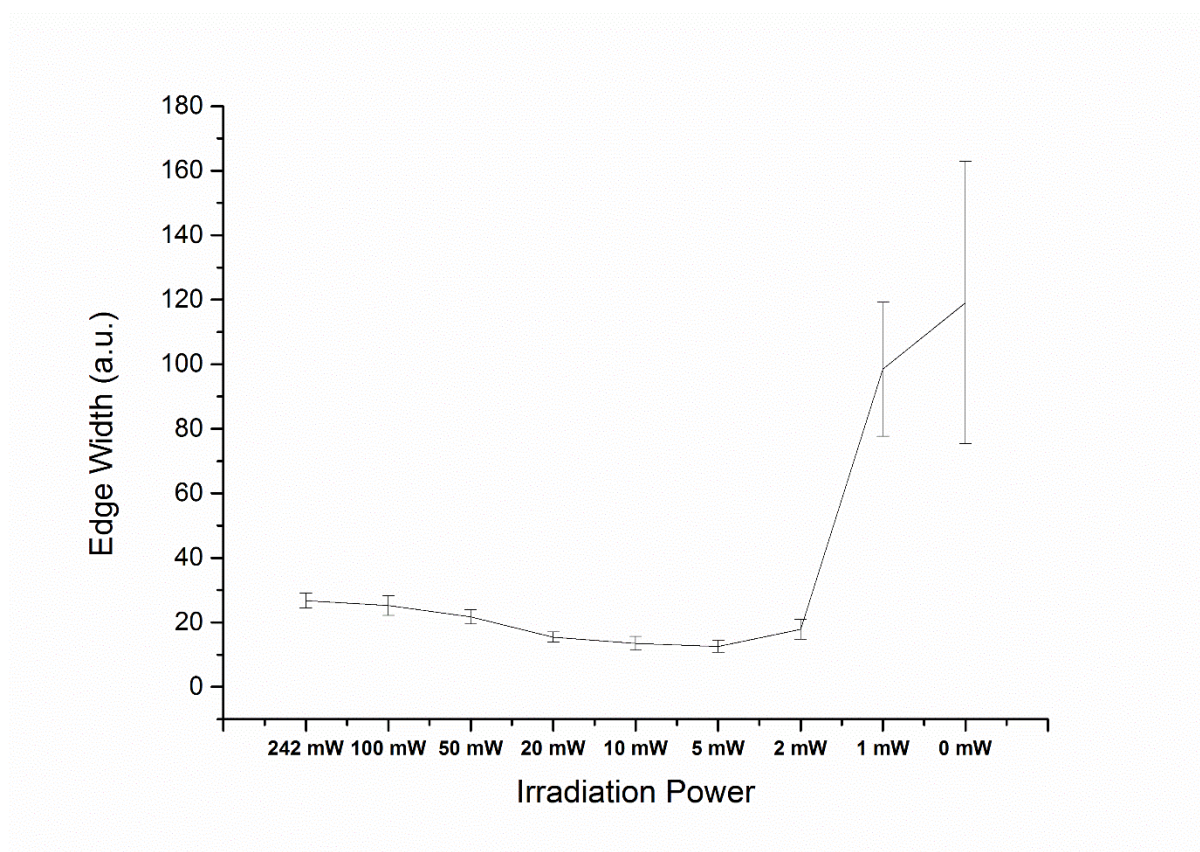


Fig. 6.28 Edge fidelity under varying irradiation power at the surface from the direction opposite to irradiation.

An analysis of the opposite surface shows that the optimal power is in the range of 5 mW – 20 mW. Below those values the spread increases due to the noise. As can be noticed, the optimal irradiation power dropped significantly, compared to the case of surface at the irradiation side. In conclusion, in the case of ZnSe monocrystals, the imaging fidelity at the deep regions of the crystal is affected by an out-of-plane excitation to a higher extent, than the decrease of SNR.

The following measurements were performed with the power of irradiation beam attenuated to 100 mW.

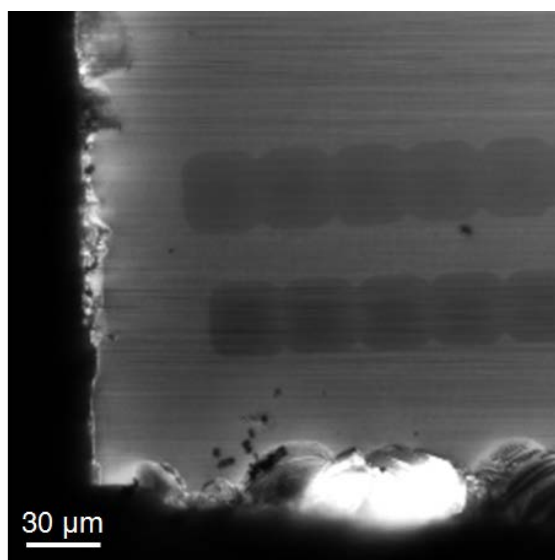


Fig. 6.29 Two-photon image of the processed surface

The two-photon image of the surface at the doped area is shown in Fig. 6.29. Comparing it with a confocal image (Fig. 6.23) reveals that the doped area excited by the means of two-photon process exhibits decrease in luminescence intensity, while single-photon case provided an opposite effect. There are multiple possible explanations to that phenomenon.

If we assume that the system is working correctly, as was proven in the previous chapters, two cases can be considered. The difference in photoluminescence can be caused either by the intrinsic properties of the two-photon process, or by the difference in the method of excitation. Let's consider the former possibility.

In this case, reduced photoluminescence in the doped area leads to a conclusion, that the probability of two-photon process was decreased by the dopants. The cross-section of two-photon absorption is well known to be dependent on the third-order hyperpolarizability of the molecule, which in return is linked with the centrosymmetry. ZnSe exhibits F43m type of symmetry and therefore this requirement is met.

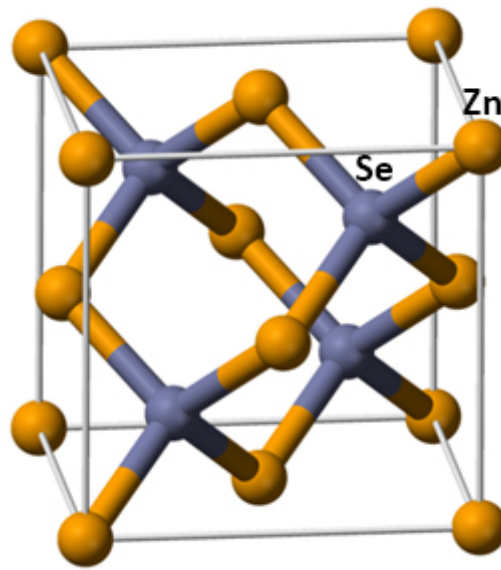


Fig. 6.30 Crystal structure of ZnSe cell unit

In case of doped unit cells, the Ga atoms can either be included into the crystalline lattice, or form an interstitial. To consider a substitution case, the atomic radius of the atoms has to be provided

Table 6.1 Size of the elements present in Ga:ZnSe

<i>Element</i>	<i>Atomic Radius</i>
<i>Zinc</i>	142 pm
<i>Selene</i>	103 pm
<i>Gallium</i>	136 pm

Ga atom is 4.2% smaller than Zn atom, and 32% bigger than Sn atom. Furthermore, it has been reported, that dopants in ZnSe exhibit a tendency to substitute Zn atoms in the crystalline structure [90]. Since the difference in atomic radii of this atoms is insignificant (<10%) the crystal lattice should not undergo distortion, and the symmetry would be preserved. However in [90] the doping was implemented at the growth stage, by the

molecular beam epitaxy, which is a considerable less abrupt process, than applied in the study FIB. This might lead to increased probability of forming of the interstitial defects, which in fact would affect the symmetry of the lattice.

Another explanation of the decrease in photoluminescence under two-photon conditions might be forming of mixed phase of ZnSe and Gallium Selenide (GaSe) in the doped volume. Under high concentrations of doping, it is possible that the dopant substitutes the atoms of the original material, as it takes place in aluminum doped ZnO [91]. This substitution is further promoted by the performed annealing.

GaSe is a semiconductor with significantly different properties to these of ZnSe. Hexagonal crystalline structure and 2.1 eV indirect band gap, to name a few. Additionally, it does not exhibit centrosymmetry. These properties affect two-photon absorption cross-section. The hexagonal crystal structure can also affect the polarization properties. To study this effect, sample was irradiated with 0°, 60° and 120° linearly polarized beam. The irradiation power was adjusted to equal 100 mW at all polarization angles. The images of the surface of the doped ZnSe under these conditions are shown in Fig. 6.31.

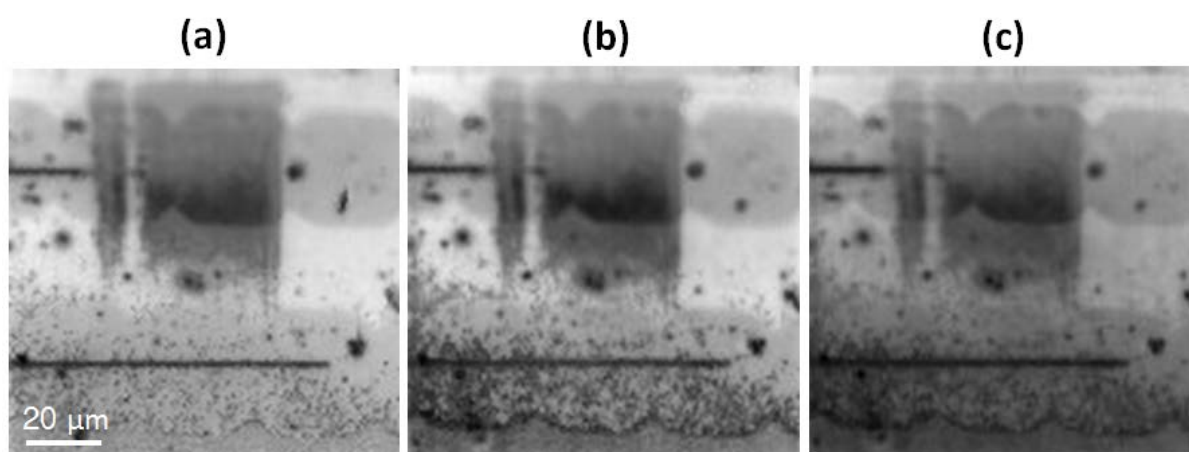


Fig. 6.31 Image of the processed surface irradiated with (a) 0°, (b) 60° and (c) 120° linearly polarized beam.

As can be observed, irrespectively of the polarization angle, the doped area appears darker, than the surrounding, unaffected ZnSe. This results does not clarify if the GaSe formed in the doped area, since it might be simply impossible to excite this semiconductor under conditions found in the developed system.

More in-depth analysis of the decrease of two-photon absorption (TPA) and increase of one-photon absorption (OPA) requires considering the effect of distinct irradiation methods. In case of OPA in confocal microscope, the sample is irradiated with continuous wave laser diode, while in the developed two-photon system, the TPA is induced with a femtosecond laser. Excitation for a prolonged time frame with continuous wave leads to higher charge carrier concentrations, than is obtainable with the pulsed source. High carrier density results in division of the population due to the lack of available states in the conductive band. This finally results to creation of excitonic states, which exhibit prolonged lifetime and significant diffusion length [92], in the order of magnitude of micrometers for semiconductor crystals. Diffusing excitons can recombine in other, not affected crystal cell units [93].

Despite the ambiguity of the photoluminescence decrease, it does not diminish the ability to differentiate the doped volume. Inversely to the confocal images, the density of dopants correlates with the decrease of the intensity, and can be estimated with the same analytical methods.

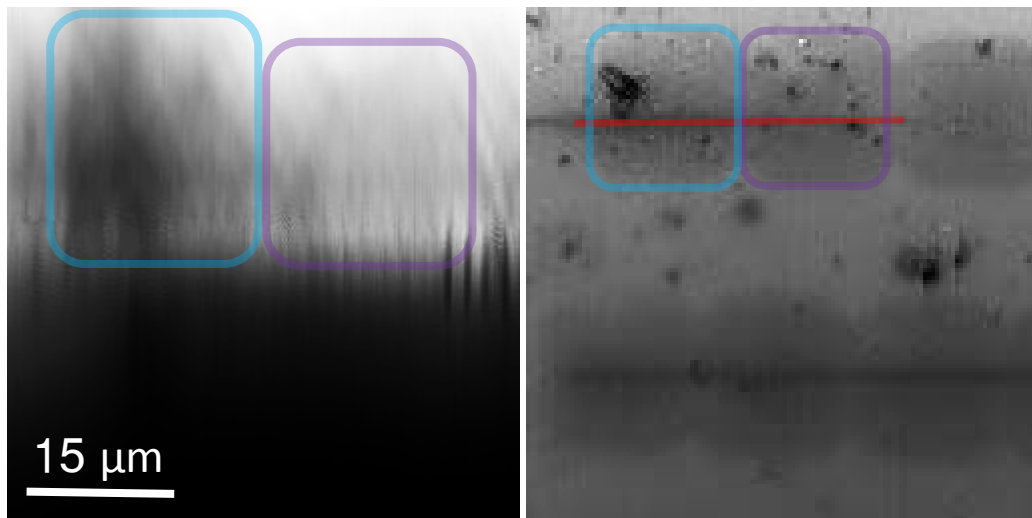


Fig. 6.32 Two-photon (a) cross section (b) top-down image of the doped area. Cross-section image is take along the red marker. Blue and purple squares mark the related doping areas.

A cross-section two-photon image is shown in Fig. 6.32. The cross-section was imaged along the area doped with acceleration voltage of 15 kV. The red line on the right hand-side figure marks the exact imaging path. Annealing resulted in increased sensitivity of the sample. So far, the two-photon imaging did not leave any visible damage on the samples. However ZnSe after annealing is significantly affected by the radiation. The damage can be clearly seen on Fig. 6.31. Both, marks of plane scanning, and cross-sectional scanning are clearly visible.

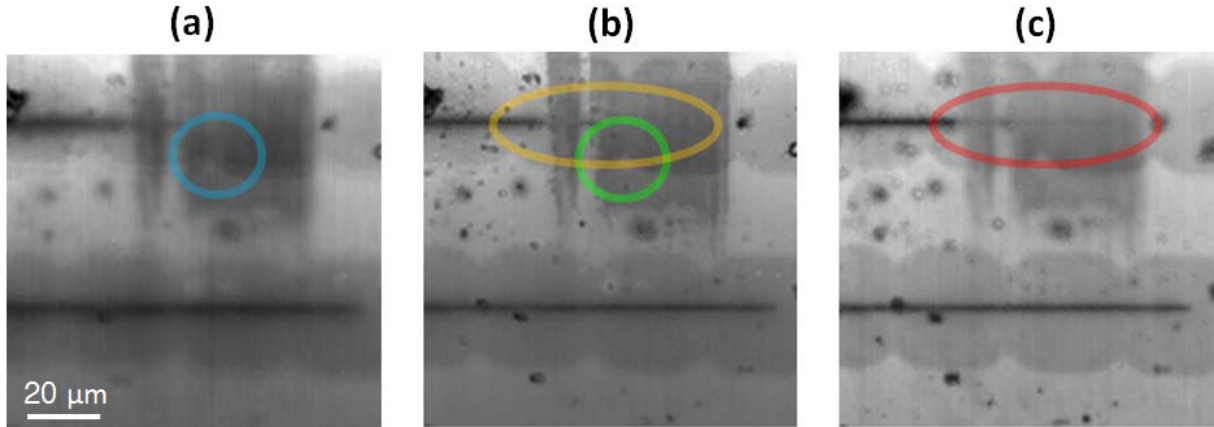


Fig. 6.33 Two-photon image of the doped ZnSe monocrystal at different depths of focusing. Markers indicate the areas with clear change of the image.

Fig. 6.33 shows a two-photon image of the doped area at different depths. The area was doped from a vertical direction, therefore the shape of the doping does not change or shift. Red oval visible at the image of the surface and 21.36 μm deep marks the defect inflicted by the two-photon imaging at a depth below 10.68 μm inside the sample, which was not visible at the surface. The damage inflicted by the cross-sectional scans was visible through all the volume of the imaging.

Fig. 6.32 can provide an information about the depth of the doping. Blue and purple square markings enclose the doped volume, differentiated by the decrease of the photoluminescence. The blue marking encircles a volume doped with a dose of 1.0 $\text{nC}/\mu\text{m}^2$. The purple marking encloses a volume doped with 0.9 $\text{nC}/\mu\text{m}^2$. To better visualize the intensity decrease in the doped area, a colorized intensity distribution of the cross-section image is presented in Fig. 6.34.

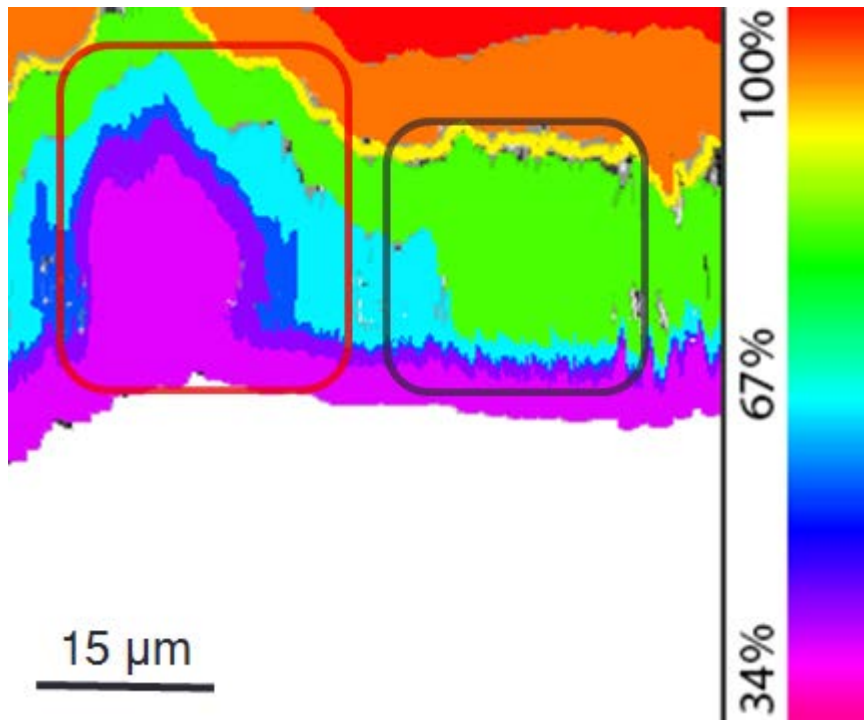


Fig. 6.34 Intensity distribution of ZnSe monocrystal in the doped volume.

The depth of the doped area for the $1.0 \text{ nC}/\mu\text{m}^2$ implemented with acceleration voltage of 15 kV and 10 kV was calculated as a difference of relative average intensity of the doped area in comparison with the average intensity of the undoped area at the same depth of the semiconductor crystal, to remove the effect of changing photoluminescence with the depth of imaging. The result of this calculation is shown in Fig. 6.35. The presented result indicates that the depth for strong doping is dependent on the acceleration voltage. For the 15 kV case, the doping started to dilute at $73 \mu\text{m}$ of depth. For 10 kV, this depth equaled $64 \mu\text{m}$. Below this values, the effect of dopant diffusion can be observed as a slope, indicating a gradual increase of the photoluminescence intensity, back to the level of undoped parts of the semiconductor. For both cases, after about $30 \mu\text{m}$ flattening of the curve can be noticed, which can be attributed to the complete recovery of the original crystalline structure.

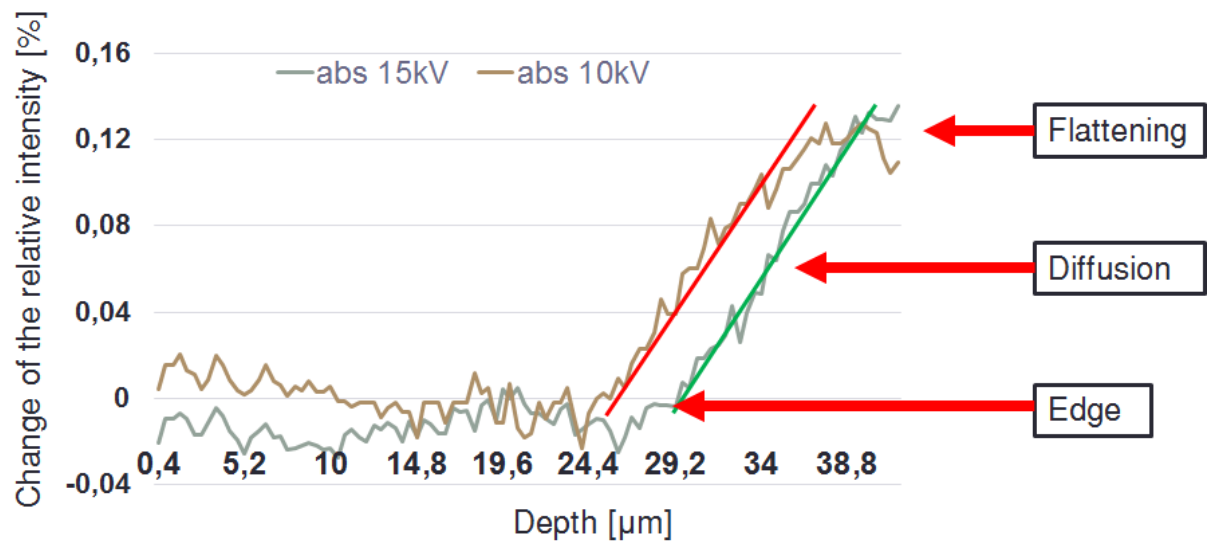


Fig. 6.35 Relative intensity between doped and not processed volume at given depth of focusing, for 10 kV and 15 kV acceleration voltage of dopant implantation.

7. Measurement Uncertainty

To illustrate the achievable precision of the developed system measurement uncertainty of the depth of uniformly doped volume of ZnSe calculated in chapter 6.4 will be estimated. The biggest advantage of two-photon microscopy is an ability of deep in-bulk imaging with high optical sectioning. Therefore determination of depth of nonuniformity is the primary function of such system, and seems most appropriate to focus on.

Since the measurement was performed once, type B evaluation of uncertainty has to be adopted. The result of depth measurement is obtained by the analysis of intensity measurement and therefore is an indirect measurement. An uncertainty of intensity measurement is a result of various noises and fluctuations in the system which can be specified as:

- Laser intensity fluctuations
- Dark counts of PMT
- Temperature dependence of laser and PMT fluctuations
- Parasitic light

Additionally, positioning uncertainty of the sample affects the absolute measurement of the depth. This uncertainty is mostly a result of the following factors:

- Positioning stage error
- Thermal expansion
- Vibrations
- Uncertainty of calibration (pixel size)

Uncertainty of positioning in axial direction has a direct impact on the measurand as it runs parallel to the measured value and is expressed in the same units.

$$u(z) = \sqrt{\frac{\Delta r_{z2P}^2}{3} + \frac{\Delta x^2}{3} + \Delta p^2} \quad (7.141)$$

where:

Δr_{z2P} – pixel size in axial direction

Δx – pixel size in axial direction

Δp – uncertainty of the stage positioning

Neglected are amplitude of vibrations due to optical table dampening, thermal expansion due to stabilized thermal conditions, and diffusion of charged careers through excitonic recombination path as it affects the final result by negligible vaue.

Standard intensity uncertainty can be evaluated from:

$$u(I) = \sqrt{\Delta I_{Ti:Sapp}^2 + \Delta I_{PMT(temp)}^2} \quad (7.242)$$

where:

$\Delta I_{Ti:Sapp}$ – short-term laser fluctuations

$\Delta I_{PMT(temp)}$ – dark counts of PMT at the measurement temperature

Impact of parasitic light was neglected, since the achieved signal to noise ratio in the system exceeded 1000.

The measurement is made by finding the depth at which relative intensity starts to increase compared to the not doped volume. This method increases the uncertainty further, since both doped and not doped volume fluorecence affect the readout. Combined standard uncertainty of relative intensity can be derived from:

$$u_c(\Delta I) = \sqrt{\frac{\partial(I_d - I_u)}{\partial I_d} u^2(I_d) + \frac{\partial(I_d - I_u)}{\partial I_u} u^2(I_u)} \quad (7.343)$$

where:

I_d – Intensity in the doped volume

I_u – Intensity out of the doped volume

and reduces to doubled standard intensity uncertainty.

Since two presented uncertainties affect the measurand differently and have to be combined, it is important to analyze the effect of indirect intensity uncertainty on the final result. In this case the doping depth estimation is obtained by fitting a line and taking the depth value at its cross point with the X axis as shown in Fig 6.35. An impact of intensity uncertainty can be included by its potential to affect the shift of position of this cross point. This potential is illustrated on Fig. 7.1.

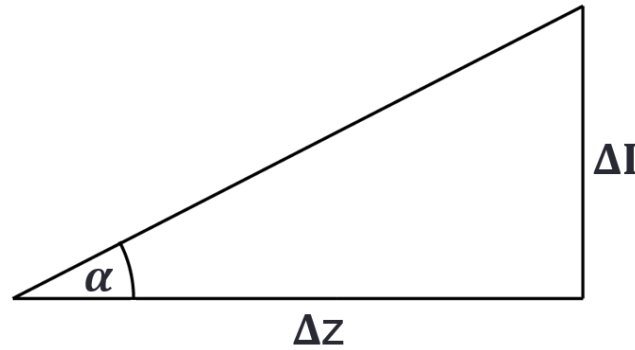


Fig. 7.1 Influence of intensity measurement uncertainty on the depth reading. α – angle between the fitted line and X axis obtained from Fig. 6.35.

Therefore the combined depth measurement uncertainty is:

$$u_c(d) = \sqrt{\frac{\partial \left(z + \frac{\Delta I}{\tan \alpha} \right)}{\partial z} u^2(z) + \frac{\partial \left(z + \frac{\Delta I}{\tan \alpha} \right)}{\partial (\Delta I)} u_c^2(\Delta I)} \quad (7.444)$$

By substituting the variables with catalog and measured values an estimated measurement uncertainty for this particular example is 1.7 μm .

8. Summary

This dissertation presents a method of three-dimensional imaging of defects and dopants in wide band gap semiconductors by spectrally resolved two-photon fluorescence microscopy. Tightly focused light beam radiated by titanium-doped sapphire laser is used to obtain two-photon excitation of selected area of the semiconductor sample. Photoluminescence intensity of a specific spectral range is selected by optical band pass filters and measured by photomultiplier tube. Reconstruction of specimen image is done by scanning the volume of interest by piezoelectric positioning stage and measuring the spectrally resolved photoluminescence intensity at each point.

It was proven, that two-photon fluorescence is a technique capable of three-dimensional imaging of doped area in the wide band gap semiconductors. We believe that currently it is the only technique with such possibilities and further investigation might lead to development of industry-class microscope capable of imaging the distribution of dopants in wide variety of samples. Such device might have a tremendous impact on the manufacturing of semiconductor devices by giving access to precise engineering in axial dimension with ease. A step forward from the currently available techniques which allow only for rough estimation of the structure, without deep penetration.

The method was used to observe intrinsic defects in zinc oxide nanorods sample containing of nanoparticles of length in range of 2.5-3.5 μm and diameter in range of 0.3-0.5 μm . The sample was scanned in search for crystalline structure point defects, oxygen vacancies and zinc interstitials. The study found agglomerations of the above defects and image of their distribution was acquired. The results and analysis of depth of penetration and achievable resolution for the said wide band gap semiconductor material was estimated.

Another application of the method is imaging of depth and distribution of doped areas in semiconductors, namely gallium doped zinc selenide. Imaging abilities were compared with the confocal fluorescence microscopy. The developed two-photon microscope was able to image the whole doped volume, which was beyond capabilities of market-available confocal

microscope, due to the inferior penetration abilities. Additionally the study found, that the doped volume exhibits decrease of the dopant density at the edges, due to the diffusion taking place during annealing. The method was able to successfully determine and compare the depth of doping with acceleration voltage equal 10 kV and 15 kV. The obtained results show that this increase of acceleration voltage lead to deepening of the doping, by approximately 15%.

Our method was proven to be effective in volume imaging of mechanical as well as intrinsic defects of the wide band gap semiconductors, with high axial resolution. The resolution of the method was calculated using the equations available in the literature. The theoretical lateral resolution of two-photon fluorescent microscope with presented parameters is 163 nm, and the theoretical axial resolution is 1198 nm, however the theoretical resolution is affected by the refractive index of the imaged material. It also has to be noted, that in presented case the resolution is additionally affected by the excited charge carrier diffusion. High carrier lifetime and mobility in the semiconductors results in radiative recombination of some charge carriers outside of the irradiation area. Precise impact of this phenomenon on the resolution is impossible to predict. Maximum imaging depth was estimated at 35 μm for zinc oxide monocrystals and is strongly dependent on the sample.

This method can be used for quality control of preprocessed semiconductors by detecting mechanical impurities as well as determining the content of intrinsic defects at any stage of production of semiconductor devices. Other methods of volume defect identification, like XRD, provide information only about the existence of various defects, without the ability to image them. Imaging of these defects will help in gaining a better understanding of their source and propagation, and might lead to significant improvements in suppressing the formation of impurities during the processing of semiconductors.

The method can draw from years of development of laser scanning microscopy, fluorescence microscopy and two-photon fluorescence microscopy for biological applications, to achieve state-of-the-art resolution, real-time imaging and adaptation to industrial standards.

BIBLIOGRAPHY

1. Haase, M.A., et al., *Blue-green laser diodes*. Applied Physics Letters, 1991. **59**(11): p. 1272-1274.
2. Nakamura, S., T. Mukai, and M. Senoh, *Candela-class high-brightness InGaN/AlGaIn double-heterostructure blue-light-emitting diodes*. Applied Physics Letters, 1994. **64**(13): p. 1687-1689.
3. Chuang, C.-H.M., et al., *Improved performance and stability in quantum dot solar cells through band alignment engineering*. Nat Mater, 2014. **13**(8): p. 796-801.
4. Pearton, S.J. and F. Ren, *Advances in ZnO-based materials for light emitting diodes*. Current Opinion in Chemical Engineering, 2014. **3**: p. 51-55.
5. Pearton, S.J., et al., *ZnO spintronics and nanowire devices*. Journal of Electronic Materials, 2006. **35**(5): p. 862-868.
6. Przybyla, R.J., et al. *12.1 3D ultrasonic gesture recognition*. in *Solid-State Circuits Conference Digest of Technical Papers (ISSCC), 2014 IEEE International*. 2014. IEEE.
7. He, Q.P. and J. Wang, *Statistics pattern analysis: A new process monitoring framework and its application to semiconductor batch processes*. AIChE journal, 2011. **57**(1): p. 107-121.
8. Guziewicz, E., et al., *Zinc oxide grown by atomic layer deposition—a material for novel 3D electronics*. physica status solidi (b), 2010. **247**(7): p. 1611-1615.
9. Ahn, J.-H., et al., *Heterogeneous three-dimensional electronics by use of printed semiconductor nanomaterials*. science, 2006. **314**(5806): p. 1754-1757.
10. Joe Lopes, A., E. MacDonald, and R.B. Wicker, *Integrating stereolithography and direct print technologies for 3D structural electronics fabrication*. Rapid Prototyping Journal, 2012. **18**(2): p. 129-143.
11. Göppert-Mayer, M., *Über Elementarakte mit zwei Quantensprüngen*. Annalen der Physik, 1931. **401**(3): p. 273-294.
12. Kaiser, W. and C.G.B. Garrett, *Two-Photon Excitation in $\text{CaF}_2:\text{Eu}^{2+}$* . Physical Review Letters, 1961. **7**(6): p. 229-231.
13. Davidovits, P., *Scanning laser microscope*. Nature, 1969. **223**: p. 831.
14. Denk, W., J.H. Strickler, and W.W. Webb, *Two-photon laser scanning fluorescence microscopy*. Science, 1990. **248**(4951): p. 73-6.
15. Chapman, D., et al., *Diffraction enhanced x-ray imaging*. Physics in medicine and biology, 1997. **42**(11): p. 2015.
16. Edelman, R.R. and S. Warach, *Magnetic resonance imaging*. New England Journal of Medicine, 1993. **328**(10): p. 708-716.
17. Hounsfield, G.N., *Computerized transverse axial scanning (tomography): Part 1. Description of system*. The British journal of radiology, 1973. **46**(552): p. 1016-1022.
18. Huang, D., et al., *Optical coherence tomography*. Science (New York, NY), 1991. **254**(5035): p. 1178.
19. Natterer, F., *The mathematics of computerized tomography*. 2001: SIAM.
20. Haddad, W., et al., *Ultrahigh-resolution x-ray tomography*. Science, 1994. **266**(5188): p. 1213.
21. Theer, P., M.T. Hasan, and W. Denk, *Two-photon imaging to a depth of 1000 μm in living brains by use of a Ti: Al₂O₃ regenerative amplifier*. Optics letters, 2003. **28**(12): p. 1022-1024.
22. Kobat, D., et al., *Deep tissue multiphoton microscopy using longer wavelength excitation*. Optics express, 2009. **17**(16): p. 13354-13364.

23. Buist, A., et al., *Real time two-photon absorption microscopy using multi point excitation*. Journal of microscopy, 1998. **192**(2): p. 217.
24. Brakenhoff, G., et al., *Real-time two-photon confocal microscopy using a femtosecond, amplified Ti: sapphire system*. Journal of microscopy, 1996. **181**(3): p. 253-259.
25. Fujita, K., et al. *Real-time confocal two-photon fluorescence microscope using a rotating microlens array*. in *Optical Engineering for Sensing and Nanotechnology (ICOSN'99)*. 1999. International Society for Optics and Photonics.
26. Bewersdorf, J., R. Pick, and S.W. Hell, *Multifocal multiphoton microscopy*. Optics letters, 1998. **23**(9): p. 655-657.
27. Hoover, E.E. and J.A. Squier, *Advances in multiphoton microscopy technology*. Nature photonics, 2013. **7**(2): p. 93.
28. Niesner, R., et al., *The power of single and multibeam two-photon microscopy for high-resolution and high-speed deep tissue and intravital imaging*. Biophysical journal, 2007. **93**(7): p. 2519-2529.
29. Girkin, J.M., S. Poland, and A.J. Wright, *Adaptive optics for deeper imaging of biological samples*. Current opinion in biotechnology, 2009. **20**(1): p. 106-110.
30. Pillai, R.S., et al., *Multiplexed two-photon microscopy of dynamic biological samples with shaped broadband pulses*. Optics express, 2009. **17**(15): p. 12741-12752.
31. Piston, D.W., *Two-Photon Excitation Microscopy for Three-Dimensional Imaging of Living Intact Tissues*. Fluorescence Microscopy: From Principles to Biological Applications, 2017.
32. Koeckhoven, S., W. Buma, and C. De Lange, *Four-photon excitation of autoionizing states of Ar, Kr, and Xe between the $2P\ 3/2$ and $2P\ 1/2$ ionic limits*. Physical Review A, 1995. **51**(2): p. 1097.
33. Zheng, Q., et al., *Frequency-upconverted stimulated emission by simultaneous five-photon absorption*. Nature Photonics, 2013. **7**(3): p. 234.
34. Tamasaku, K., et al., *X-ray two-photon absorption competing against single and sequential multiphoton processes*. Nature Photonics, 2014. **8**(4): p. 313.
35. Liu, Q., et al., *Strong two-photon-induced fluorescence from photostable, biocompatible nitrogen-doped graphene quantum dots for cellular and deep-tissue imaging*. Nano letters, 2013. **13**(6): p. 2436-2441.
36. He, K., et al., *Tightly bound excitons in monolayer WSe₂*. Physical review letters, 2014. **113**(2): p. 026803.
37. Hayat, A., P. Ginzburg, and M. Orenstein, *Observation of two-photon emission from semiconductors*. Nature photonics, 2008. **2**(4): p. 238.
38. Alex, H., et al., *Applications of two-photon processes in semiconductor photonic devices: invited review*. Semiconductor Science and Technology, 2011. **26**(8): p. 083001.
39. Noor, A.S.M., et al., *Two-photon excited luminescence spectral distribution observation in wide-gap semiconductor crystals*. Applied Physics Letters, 2008. **92**(16): p. 161106.
40. Al-Tabich, A., et al., *3D imaging of intrinsic crystalline defects in zinc oxide by spectrally resolved two-photon fluorescence microscopy*. Applied Physics Letters, 2017. **110**(22): p. 221106.
41. Mondal, P.P. and A. Diaspro, *Multiphoton Fluorescence Microscopy*, in *Fundamentals of Fluorescence Microscopy: Exploring Life with Light*. 2014, Springer Netherlands: Dordrecht. p. 149-159.
42. Boyd, R.W., *Nonlinear optics*, in *Handbook of Laser Technology and Applications (Three-Volume Set)*. 2003, Taylor & Francis. p. 161-183.
43. Sheppard, C. and A. Choudhury, *Image formation in the scanning microscope*. Journal of Modern Optics, 1977. **24**(10): p. 1051-1073.

44. Born, M. and E. Wolf, *Principles of optics: electromagnetic theory of propagation, interference and diffraction of light*. 1980: Elsevier.
45. Wilson, T., *Optical sectioning in confocal fluorescent microscopes*. Journal of Microscopy, 1989. **154**(2): p. 143-156.
46. Török, P. and T. Wilson, *Rigorous theory for axial resolution in confocal microscopes*. Optics Communications, 1997. **137**(1): p. 127-135.
47. Kanicki, J., et al., *Stretched exponential illumination time dependence of positive charge and spin generation in amorphous silicon nitride*. Applied Physics Letters, 1990. **57**(7): p. 698-700.
48. Bourgoin, J.C., *What happens in semiconductors during quenching*. Physics Letters A, 1984. **106**(3): p. 140-142.
49. Kasha, M., *Characterization of electronic transitions in complex molecules*. Discussions of the Faraday society, 1950. **9**: p. 14-19.
50. Srikant, V. and D.R. Clarke, *On the optical band gap of zinc oxide*. Journal of Applied Physics, 1998. **83**(10): p. 5447-5451.
51. Chandramohan, R., C. Sanjeeviraja, and T. Mahalingam, *Preparation of zinc selenide thin films by electrodeposition technique for solar cell applications*. physica status solidi (a), 1997. **163**(2).
52. Monllor-Satoca, D., et al., *The "Direct-Indirect" model: An alternative kinetic approach in heterogeneous photocatalysis based on the degree of interaction of dissolved pollutant species with the semiconductor surface*. Catalysis Today, 2007. **129**(1): p. 247-255.
53. Lincot, D. and G. Hodes. *Chemical Solution Deposition of Semiconducting and Non-Metallic Films: Proceedings of the International Symposium*. 2006. The Electrochemical Society.
54. Levinshtein, M.E., S.L. Rumyantsev, and M.S. Shur, *Properties of Advanced Semiconductor Materials: GaN, AlN, InN, BN, SiC, SiGe*. 2001: John Wiley & Sons.
55. Park, J., et al., *Coulomb blockade and the Kondo effect in single-atom transistors*. Nature, 2002. **417**(6890): p. 722-725.
56. Flynn, C.P., *Point defects and diffusion*. 1972.
57. Glinchuk, M., *The Dynamical Jahn-Teller Effect in Localized Systems*. 1984.
58. Lebedev, A. and I. Sluchinskaya, *Unusual phase transitions in $Pb_{1-x}Sn_xTe_{1-y}Se_y$ and $Pb_{1-x}Sn_xTe_{1-y}Si_y$ crystals induced by Sn off-center ions*. Ferroelectrics, 1993. **143**(1): p. 91-98.
59. Alkauskas, A., M.D. McCluskey, and C.G. Van de Walle, *Tutorial: Defects in semiconductors—Combining experiment and theory*. Journal of Applied Physics, 2016. **119**(18): p. 181101.
60. Dannefaer, S., *Defects in semiconductors*. Radiation Effects and Defects in Solids, 1989. **111**(1-2): p. 65-76.
61. Pantelides, S.T., *The electronic structure of impurities and other point defects in semiconductors*. Reviews of Modern Physics, 1978. **50**(4): p. 797.
62. Lannoo, M., *Point defects in semiconductors I: theoretical aspects*. Vol. 22. 2012: Springer Science & Business Media.
63. Bourgoin, J., *Point defects in Semiconductors II: Experimental aspects*. Vol. 35. 2012: Springer Science & Business Media.
64. Chang, B. and M. Ameen, *High Mass Molecular Ion Implantation*. 2011: INTECH Open Access Publisher.
65. Niina, T., T. Minato, and K. Yoneda, *Ga-doped ZnSe grown by molecular beam epitaxy for blue light emitting diodes*. Japanese Journal of Applied Physics, 1982. **21**(6A): p. L387.
66. Kohan, A., et al., *First-principles study of native point defects in ZnO*. Physical Review B, 2000. **61**(22): p. 15019.
67. Zhang, S., S.-H. Wei, and A. Zunger, *Intrinsic n-type versus p-type doping asymmetry and the defect physics of ZnO*. Physical Review B, 2001. **63**(7): p. 075205.

68. Oba, F., et al., *Energetics of native defects in ZnO*. Journal of Applied Physics, 2001. **90**(2): p. 824-828.
69. Lee, E.-C., et al., *Compensation mechanism for N acceptors in ZnO*. Physical Review B, 2001. **64**(8): p. 085120.
70. Erhart, P., A. Klein, and K. Albe, *First-principles study of the structure and stability of oxygen defects in zinc oxide*. Physical Review B, 2005. **72**(8): p. 085213.
71. Janotti, A. and C.G. Van de Walle, *Native point defects in ZnO*. Physical Review B, 2007. **76**(16): p. 165202.
72. Tomlins, G.W., J.L. Routbort, and T.O. Mason, *Oxygen Diffusion in Single-Crystal Zinc Oxide*. Journal of the American Ceramic Society, 1998. **81**(4): p. 869-876.
73. Vlasenko, L. and G. Watkins, *Optical detection of electron paramagnetic resonance for intrinsic defects produced in ZnO by 2.5-MeV electron irradiation in situ at 4.2 K*. Physical Review B, 2005. **72**(3): p. 035203.
74. Reynolds, D.C., et al., *Similarities in the bandedge and deep-centre photoluminescence mechanisms of ZnO and GaN*. Solid State Communications, 1997. **101**(9): p. 643-646.
75. Reynolds, D., et al., *Source of the yellow luminescence band in GaN grown by gas-source molecular beam epitaxy and the green luminescence band in single crystal ZnO*. Solid state communications, 1998. **106**(10): p. 701-704.
76. Erhart, P. and K. Albe, *First-principles study of migration mechanisms and diffusion of oxygen in zinc oxide*. Physical Review B, 2006. **73**(11): p. 115207.
77. Lany, S. and A. Zunger, *Dopability, intrinsic conductivity, and nonstoichiometry of transparent conducting oxides*. Physical Review Letters, 2007. **98**(4): p. 045501.
78. Janotti, A., D. Segev, and C.G. Van de Walle, *Effects of cation d states on the structural and electronic properties of III-nitride and II-oxide wide-band-gap semiconductors*. Physical Review B, 2006. **74**(4): p. 045202.
79. Janotti, A. and C.G. Van de Walle, *Absolute deformation potentials and band alignment of wurtzite ZnO, MgO, and CdO*. Physical Review B, 2007. **75**(12): p. 121201.
80. Lany, S. and A. Zunger, *Anion vacancies as a source of persistent photoconductivity in II-VI and chalcopyrite semiconductors*. Physical Review B, 2005. **72**(3): p. 035215.
81. Janotti, A. and C.G. Van de Walle, *Oxygen vacancies in ZnO*. Applied Physics Letters, 2005. **87**(12): p. 122102.
82. Madelung, O., *Semiconductors—basic data*. 2012: Springer Science & Business Media.
83. Ahn, C.H., et al., *A comparative analysis of deep level emission in ZnO layers deposited by various methods*. Journal of Applied Physics, 2009. **105**(1): p. 013502.
84. Vempati, S., J. Mitra, and P. Dawson, *One-step synthesis of ZnO nanosheets: a blue-white fluorophore*. Nanoscale research letters, 2012. **7**(1): p. 470.
85. Rodnyi, P. and I. Khodyuk, *Optical and luminescence properties of zinc oxide (Review)*. Optics and Spectroscopy, 2011. **111**(5): p. 776-785.
86. Cao, B., W. Cai, and H. Zeng, *Temperature-dependent shifts of three emission bands for ZnO nanoneedle arrays*. Applied physics letters, 2006. **88**(16): p. 161101.
87. Yukawa, R., et al., *Electron-hole recombination on ZnO (0001) single-crystal surface studied by time-resolved soft X-ray photoelectron spectroscopy*. Applied Physics Letters, 2014. **105**(15): p. 151602.
88. Das, D. and P. Mondal, *Photoluminescence phenomena prevailing in c-axis oriented intrinsic ZnO thin films prepared by RF magnetron sputtering*. Rsc Advances, 2014. **4**(67): p. 35735-35743.
89. Hvedstrup Jensen, G., *Temperature Dependence of the Band Gap in ZnO from Reflection Data*. physica status solidi (b), 1974. **64**(1): p. K51-K54.

90. Hu, B., et al., *Gallium-related defect centers in molecular-beam-epitaxy-grown ZnSe films: Influence of electric field on thermal emission of electrons*. Physical Review B, 1993. **47**(15): p. 9641.
91. Hou, Q., F. Meng, and J. Sun, *Electrical and optical properties of Al-doped ZnO and ZnAl₂O₄ films prepared by atomic layer deposition*. Nanoscale research letters, 2013. **8**(1): p. 144.
92. Logue, F., et al., *Optical measurement of the ambipolar diffusion length in a ZnCdSe–ZnSe single quantum well*. Journal of applied physics, 1997. **81**(1): p. 536-538.
93. Hodes, G. and P.V. Kamat, *Understanding the implication of carrier diffusion length in photovoltaic cells*. 2015, ACS Publications.

Acknowledgments

I would like to express my deepest gratitude to Professor Ryszard Jabłoński for his continuous support for the past 6 years. His trust allowed me to develop a confidence necessary for researcher. His guidance led me to opportunities that I could not imagine as an undergraduate student. I might not be able to ever repay this debt of kindness, but it will not stop me from trying.

I would also like to thank Professor Yoshimasa Kawata for providing such an amazing opportunity to perform my research in his tremendous laboratory. Only his excellent insight allowed me to achieve presented results. This 3 years I spent under his supervision allowed me to progress and achieve my self-development milestones.

Professor Wataru Inami saved me countless times with his technical guidance and research advice. Without his contribution I would not be able to develop the presented system. I would like to thank him, as well as all other members of Kawata Laboratory, for their support and all the time spent together during my stay.

I would also like to include Dr. Edvīns Daukšta for his friendship and hundreds of hours of discussions concerning his field of expertise, material science. I want to sincerely thank him for expanding my understanding in a manner immediately applicable to my research. I am extremely lucky that I met him in such an unlikely conditions.

Finally I would like to thank my family and friends who always believed in me, especially my mother, Kinga Al-Tabich, for all the support and encouragement in pursuing education, even in the hardest of times.

SUPPLEMENT 1

Zinc Oxide microparticles as a biological marker

This chapter presents an inconclusive study on the application of the ZnO microparticles in the form of powder as a marker for two-photon imaging of the biological samples.

The microparticles in the size of 10 μm were mixed with culture medium and applied to in vivo cells. Cells were incubated in this conditions for 72 hours. After the feeding process, cells have been fixed with a formaldehyde solution and imaged with phase-contrast and two-photon microscopes. Imaging of the cells revealed that the ZnO powder settled on the cell membrane

Marco cells

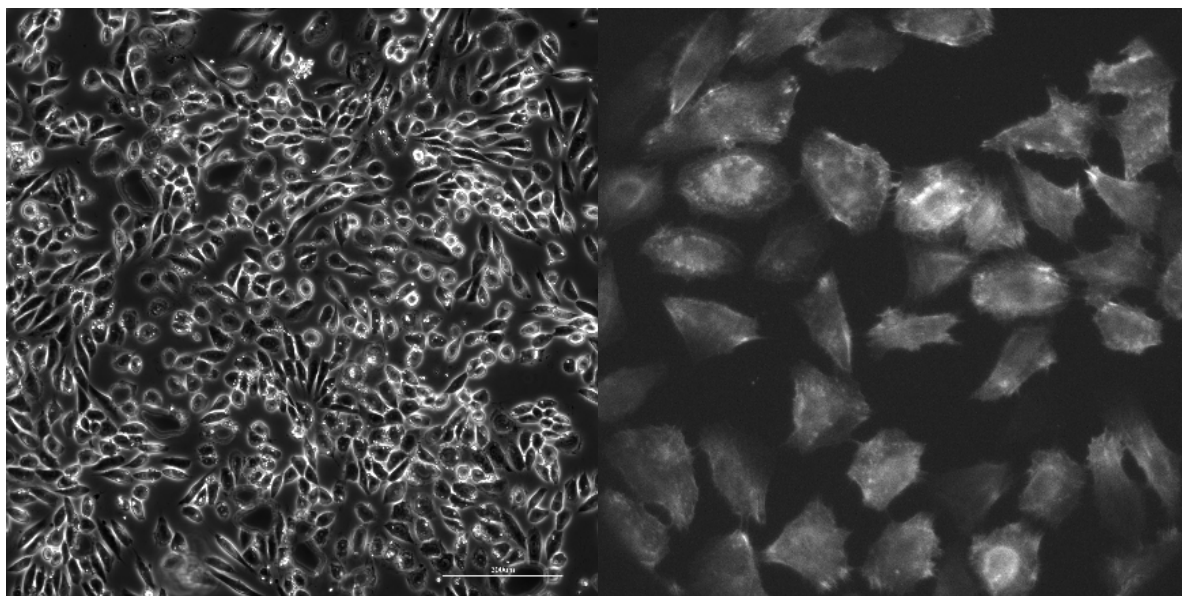


Fig. S1.1

HeLa cells

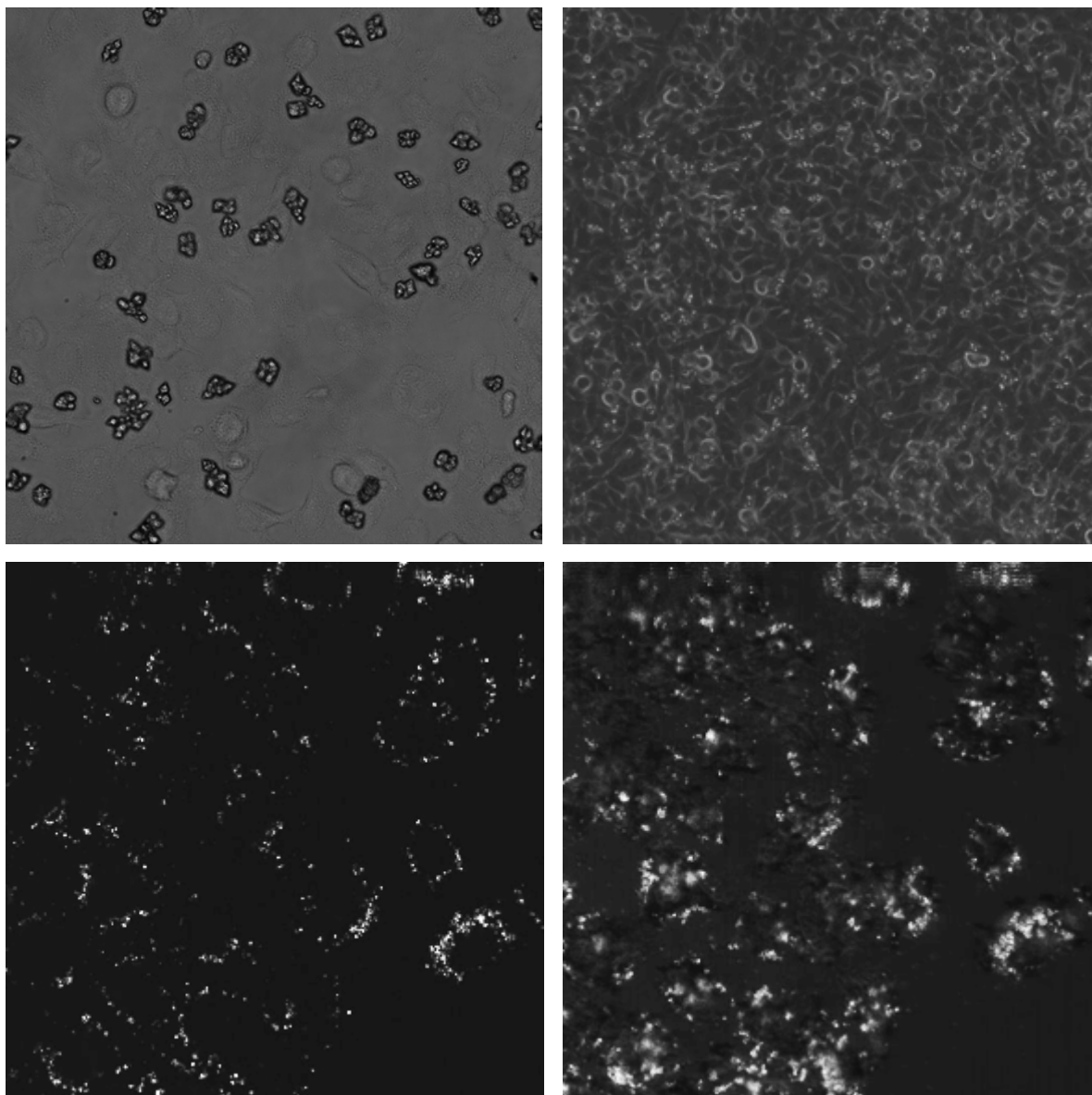


Fig. S1.2

In conclusion, both studied cell lines failed to absorb the ZnO powder. This result indicates, that the ZnO microparticles of the given size are not suitable two-photon imaging marker for the internal structure of the studied cells. It can still be used as a position marker, however for this purpose other methods already exist.